UNIVERSITÀ
DEGLI STUDI
DI PADOVA

Dipartimento
di Fisica
e Astronomia
Galileo Galilei

CORSO DI LAUREA MAGISTRALE ASTROPHYSICS AND COSMOLOGY

TESI MAGISTRALE

Photometry and astrometry of M22: an integration with spectroscopy for a state-of-the-art characterization.

LAUREANDO

Augusto Bouras Moreno Sanchez

Matricola 2071452

RELATORE

Prof. Antonino Milone

UNIPD

CORRELATORE

Dott. Emanuele Dondoglio

UNIPD

ANNO ACCADEMICO
2023/2024

To my family
and friends.

Abstract

The presence of multiple stellar populations in globular clusters is one of the most intriguing and mysterious phenomenon in stellar astrophysics. Indeed, these systems host distinct groups of stars typically classified as first generation (1G), with chemical composition akin to halo field stars, and second-generation (2G) stars, with peculiar light-elements composition. Beyond the bulk 1G and 2G patterns typical of old and massive GCs (hereafter, the *canonical* stars), a subclass of about one-fifth of the studied GCs, dubbed anomalous, presents an additional group of stars enriched in heavier elements, such as s-process elements and iron content. This latter class of clusters has been poorly explored in the literature, and a comprehensive characterization of these structures is mandatory to shed light on the processes that led to the formation of anomalous star and their link with the multiple stellar populations phenomenon.

In this work, an extended study on the anomalous GC M22 is presented, both deriving fundamental global parameters, such as age and distance, and exploring its chemically-different populations.

First, the most recent Hubble Space Telescope optical observations were reduced by performing state-of-the-art Point Spread Function photometry. The resulting Color-Magnitude diagram, published here for the first time, has then been used to infer the age, distance, and reddening of M22. Findings show an age range of 13.2 to 13.8 Gyr, a distance of 3.31 kpc, and mean reddening E(B-V) = 0.39, which are in agreement with previous estimates from the literature.

Then, several multiband archive photometric catalogs were considered, involving UV and optical magnitudes, from HST and ground-based observations. To identify the chemically different populations in M22 along the red giant branch -including 1G, 2G, and anomalous stars- from the GC center to the outskirts. With this extended dataset, it was possible to derive the fraction of the different populations and their radial distribution. It was found that 2G stars are more centrally concentrated than the 1G and hints of the anomalous population being more centrally concentrated than the bulk of 1G and 2G stars.

Combining the photometric population tagging introduced in this work with literature spectroscopy abundances allowed to directly investigate the Na, Al, and Fe chemical differences between the different populations. I found that 2G stars are enhanced in Na and Al compared to 1G stars, and that anomalous population presents a spread in these elements, thus proving that that they are characterized by light-elements inhomogeneities. Intriguingly, anomalous stars are distributed around higher [Na/Fe] and [Al/Fe] values than the bulk of 1G and 2G stars. Finally, I confirm with this robust approach, based on both photometry and spectroscopy, the presence of a [Fe/H] spread, with anomalous stars being 0.124 dex metal-richer than the rest of M22 stars.

Contents

List of Figures

List of Tables

List of Acronyms

ACS Advanced Camera for Surveys
AGB Asymptotic Giant Branch
AGC Anomalous Globular Clusters
CDF Cumulative Distribution Function
ChM Chromosome Map
CMD Color-Magnitude Diagram
CTE Charge Transfer Efficiency
DG Dwarf Galaxy
ePSF effective Point Spread Function
FoV Field of View
FRMS Fast Rotating Massive stars
GB Ground Based
GC Globular Cluster
HB Horizontal Branch
HBB Hot Bottom Burning
HST Hubble Space Telescope
iPSF instrumental Point Spread Function
ISM Inter Stellar Medium
KDE Kernel Density Estimation
Λ**CDM** Λ Cold Dark Matter
MIB Massive Interacting Binary
MS Main Sequence
MSP Multiple Stellar Population
MSTO Main Sequence Turn-Off
MW Milky Way galaxy
PSF Point Spread Function
RGB Red Giant Branch

SGB	Sub-Giant Branch
SMS	Super Massive stars
SN	Supernova explosion
SSP	Simple Stellar Population

1

Introduction

In this chapter, an introduction to the present day view of Globular Cluster (GC) is provided. **Sec. 1.1** explains what is the Multiple Stellar Population (MSP) phenomenon and summarizes its main observational properties. **Sec. 1.2** discusses some of the most appealing theoretical formation scenarios and their implications. **Sec. 1.3** introduces the Type I and Type II subclasses of GCs, explaining their main differences in terms of photometric diagrams and chemical abundances. The target of this thesis, M22, is presented in **Sec. 1.4**. Finally, **Sec. 1.5** provides the outline of the thesis.

1.1 MULTIPLE POPULATIONS IN GLOBULAR CLUSTERS

Until a few years ago, GCs were assumed to be prototypes of Simple Stellar Population (SSP), populated by thousands to millions of old Population II stars with the same age and chemical composition, tightly bound by gravity on a dense stellar system with spherical symmetry. Thanks to the large amount of data gathered from both spectroscopic and photometric observations in the last decades, the aforementioned picture of GCs have to be modified. Indeed, throughout the years light-elements variations have been detected among Red Giant Branch (RGB), Sub-Giant Branch (SGB), and Main Sequence (MS) stars of several GCs. In particular, the light element abundances describe well-defined trends of C-N, O-Na, and Mg-Al anticorrelation, suggesting that these anomalies result from hot H-burning in ON, NeNa, and MgAl proton capture chains (e.g., Kraft, 1994; Gratton et al., 2004; Carretta et al., 2009; Marino et al., 2008; Marino et al., 2012).

The consequence of these chemical variation can be detected by employing high-precision photometry. In particular, UV bands are instrumental to disentangle chemically-different stars, since in this wavelength range lie the absorption bands of the CH, CN, NH, and OH molecules, which track carbon, nitrogen, and oxygen variations among GC stars. The Hubble Space Telescope (HST) photometry has given a massive contribution to this field, especially thanks to the F275W, F336W (or F343N), and F438W (or F435W) bands, which allowed the development of photometric tools efficient in disentangling GCs stars. In particular, the so-called Chromosome Map (ChM) diagram, introduced by Milone et al. (2015a), unveiled the complexity and the details of this phenomenon. The ChM is a pseudo two-color diagram obtained by verticalizing the sequence of stars in the $C_{F275W,F336W,F438W}$ (definition given by **Eq. 3.2** in **Sec. 3.2.1**) and m_{F275W}-m_{F814W} filters combinations such that a chemically-uniform population in this diagram is represented by a blob of stars as extended as the observational errors. An example of this diagram in provided in the upper-left panel of **Fig. 1.1** for the RGB (in black) and the Asymptotic Giant Branch (AGB) (in red) of the Galactic GC 47 Tuc. Here, the 1G stars describe the sequence around $C_{F275W,F336W,F438W}$ ~0, while 2G stars are distributed along the 0.15-to-0.65 y-axis range. The upper-right panel displays the same diagram but for MS stars. Finally, the m_{F343N}-m_{F435W} vs. m_{F275W}-m_{F343N} two-color diagrams in the lower panels separate the two populations in the SGB (left) and in the Horizontal Branch (HB) (right). Here, 1G and 2G stars describe the sequences at lower and higher F343N-F435W colors, respectively. **Fig. 1.1** proves how the chemically-different stars in GCs form distinct populations which can be spotted in all the evolutionary stages. In particular, the fact that the phenomenon -hereafter, MSP - is still present among unevolved MS stars, demonstrates that these distinct groups of stars have a primordial origin, forming in the very early phases of a GC's life.

1.1.1 PROPERTIES OF MULTIPLE STELLAR POPULATIONS

In the past decades, the phenomenon has been extensively analyzed. In the following, the main observational properties of multiple populations are summarized:

- **1G-2G discreteness.** 1G and 2G stars group distinctly in photometric diagrams with appropriate color combinations, particularly evident in ChMs (Milone et al., 2017).

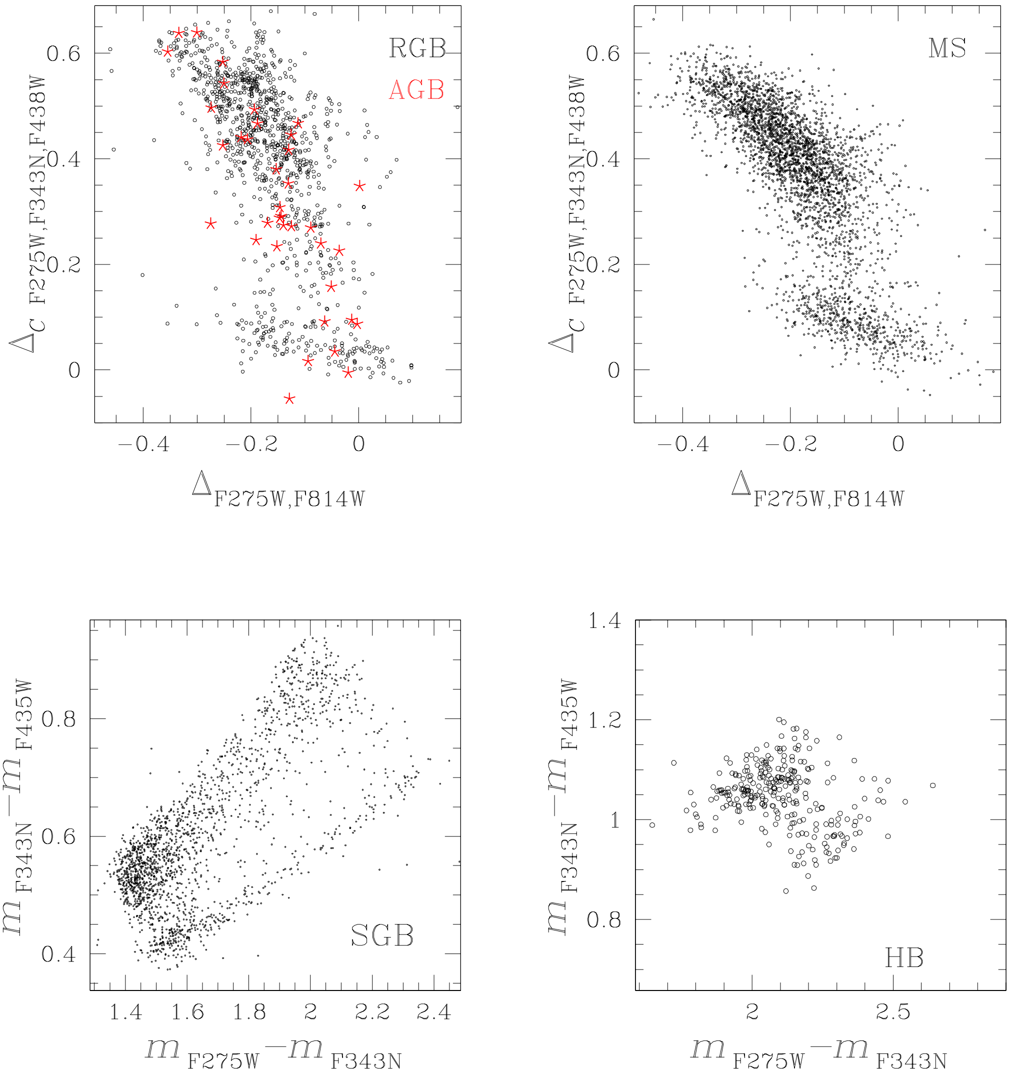

Figure 1.1: *Upper-left Panel:* superimposed $\Delta_{C\,F275W,F336W,F438W}$ vs. $\Delta_{F275W,F814W}$ ChMs for the RGB stars (black dots) and AGB stars (red starred symbols) of 47 Tuc. *Upper-right Panel:* ChM of the bright MS stars. *Lower-left and -right Panels:* $(m_{F343N} - m_{F435W})$ vs. $(m_{F275W} - m_{F343N})$ two-color diagrams of SGB and HB stars, respectively. (Image taken from Milone et al., 2022).

- **Ubiquity.** The formation of MPs is a common phenomenon of old and massive Galactic GCs, as demonstrated through the study of ChMs, where 1G and 2G stars have been found in all studied GCs (Milone et al., 2017).

- **Variety.** Some of the properties of MPs significantly change considering different clusters. An example is the fraction of 2G stars that ranges from $\sim 35\%$ as in M71, to more than 90% in ω Cen (Legnardi, 2021).

- **Dependence on cluster mass.** The incidence and complexity of MPs increase with cluster mass since the maximum internal variations of He and N, correlate with the host cluster mass (Milone et al., 2018). The least massive Galactic GCs are the only ones without MPs, thus suggesting that there is a threshold in their initial mass, below which the phenomenon does not occur, around $1.5\times10^5 M_\odot$, for its manifestation (e.g., Milone et al., 2019a).

- **Maximum He enrichment.** The maximum He variation correlates with the cluster mass. The He mass fraction ranges from Ymax < 0.01 to ~ 0.18 (Di Criscienzo et al., 2011,Milone et al., 2018).

- **Dependence on GC orbit and host galaxy.** The fractions of 1G stars of GCs with large perigalactic radius ($R_{per} > 3.5$ kpc) are typically higher than in the other GCs with similar masses (Zennaro et al., 2019); this suggests that interactions with the host galaxy during the entire life of the GC could have a role in 1G/2G fractions, as seen in Magellanic-Cloud clusters which host larger fractions of 1G stars than Milky Way galaxy (MW) GCs.

- **Stellar mass independence.** The relative amounts of 1G and 2G stars are constant in the ~ 0.15 0.80 M mass range (Milone et al., 2014).

- **Centrally-concentrated 2G.** 2G stars in GCs have been seen to be either more centrally-concentrated (Sollima et al., 2007, Bellini et al., 2009, Milone et al., 2012a, Cordero et al., 2013) or similarly radially distributed (Nardiello et al., 2014, Dalessandro et al., 2018, Milone et al., 2019b), but not more externally-concentrated than 1G ones.

- **Anisotropic motions of 2G stars.** In massive GCs, like ω Cen or 47 Tuc, 2G stars exhibit more radially-anisotropic velocity distributions than 1G stars (Richer et al., 2013, Bellini et al., 2018). Less massive GCs, as M4 or M71, show instead isotropic velocity distributions among both 1G and 2G stars suggesting that dynamical processes could have cancelled out differences in the kinematic properties of MPs at formation (Legnardi, 2021).

- **Specificity.** 2G seem to be formed only inside GCs. The small number of 2G stars found outside GCs is consistent with a scenario where these stars have been generated inside GCs and were then lost via tidal interactions (Vesperini et al., 2010), suggesting that their formation could be a distinctive feature of GCs.

- **Supernova explosion (SN) avoidance.** Excluding some Type II GCs, no variations in metallicity between 1G and 2G stars were detected thus indicating that GCs have retained a small fraction of SN products that did not appreciably contaminate 2G stars (Legnardi, 2021).

- **Hot CNO and NeNa processing.** 2G stars exhibit the chemical composition resulting from CNO cycling and p-capture processes at high temperatures (He, N, and Na enhanced, and depleted in C and O). Therefore, the Inter Stellar Medium (ISM) in which they have formed should be polluted by the elements resulting from these processes (Marino et al., 2012).

- **2G mass-budget problem.** In most GCs 2G stars are the dominant component, especially in central regions where their fractions can largely exceed $\sim 50\%$. This is a challenge for the formation scenarios in which the 1G are formed before the 2G. A possible explanation is that the progenitors of the present-day GCs had a larger mass, which has been lost (at least$\sim$ 80 - 90%) by dynamical interaction with the Milky Way. This hints to the possibility that GC were as massive as Dwarf Galaxy (DG) and lost most 1G stars (Dondoglio, 2020, Legnardi, 2021).

1.2 FORMATION SCENARIOS

The observed chemical patterns within GCs involve elements typically produced (or consumed) by the nuclear reactions in intermediate-to-high-mass stars therefore suggesting that 1G stars more massive than the ones that currently populate old GCs ejected processed material polluting the intracluster medium in which the 2G stars would form. There are two main classes of formation scenarios for MSP, in which the different groups of stars formed either by a single or multiple star formation bursts, each one considers several of possible polluters:

1. **Multiple star formation bursts.** Massive 1G star SN ejecta pollutes the

primordial material so 2G are formed from this mix. Possible polluters include AGB stars that eject material, and Fast Rotating Massive stars (FRMS) which lose material due to equatorial winds, and Super Massive stars (SMS) characterized by mass loss through intense radiation-driven stellar wind.

- **AGB stars.** Stars in the AGB phase, with masses from $\sim$ 3 to 8 $M_{\odot}$, experience the Hot Bottom Burning (HBB) process, in which very high temperatures are reached at the bottom of the convective envelope thus allowing efficient p-capture nuclear processing where proton-rich nuclides can be produced by sequentially adding one or more protons to an atomic nucleus (Ventura et al., 2013). By adding a proton to a nucleus, the element is changed and at the same time the ratio of protons to neutrons is changed, resulting in a more neutron-deficient isotope of the next element (Burbidge et al., 1957).
  HBB characterizes the AGB phase of stars with masses from at least 3 to $\sim$ 10 $M_{\odot}$ since otherwise HBB process would not operate and AGB stars would evolve as carbon (C) stars. But no C-star has been observed among 2G stars.
  In the model proposed by D'Ercole et al. (2010), the massive GC progenitor has a first major episode of star formation of 1G stars. The residual non-collapsed gas is then swept out by the SN ejection. After more than 30 Myr, AGB stars start ejecting material through ($\sim$ 10 to 30 km/s) winds slower than the GC's escape velocity so that it accumulates in the cluster. This material then cools off and accretes towards the center until a critical density is reached, at which point further starburst episodes occur leading to the formation of 2G stars from a mix of pristine gas and AGB ejecta. The GC progenitor then loses a considerable fraction of 1G stars by interacting with the parent galaxy, leaving the present-day centrally-concentrated 2G structure. In order to have 2G stars which are O depleted and Na rich, HBB should work at temperatures lower than 10^8 K given that in AGB stars, O is destroyed faster than Na.

- **FRMS.** This scenario speculates about the existence of very massive stars ($\sim$ 25 to 150 $M_{\odot}$) which are also rotating very fast ($\sim$ 800 to 1000 $\frac{km}{s}$), losing material in equatorial winds, forming a disk around them, which is rich of H-burning products (Krause et al., 2013). 2G stars may form from gravitational instability inside the disk.

Since winds continuously enrich the disk, discreteness of abundances cannot be explained by this polluter. Also, there would be no reasons for these stars not to be ubiquitous throughout the Galaxy, in contradiction with the GC specificity property.

2. **Single star formation burst.** Single generation with accretion of polluted material[1] from continuous rejuvenation through a pristine gas inflow, leading to 1G stars accreting material ejected from the more massive stars of the same generation. A possible indicator for this scenario is the MS splitting for low mass stars in young and intermediate-age star clusters which has been interpreted not only in terms of stellar populations with different rotation rates (Milone et al., 2015b) and different age (Milone et al., 2009) but also, in terms of stellar populations with different metallicity (Milone et al., 2015a), resulting in O abundance paths. Possible polluters include Massive Interacting Binary (MIB)s, Early Disk Accretion, and again SMSs.
    - **MIBs**. The forced rotation of the primary stellar envelope would cause internal mixing that brings H-burning products from the core to the envelope of the star. The processed material would then be spread outside in a subsequent common envelope phase of the MIB, polluting the ISM (Mink et al., 2009). Continuously increasing chemical differences are expected in the accreted material so MSP discreteness is not easily reproducible by this model. Also after 3 8 Myr core collapse SN begin to explode so that SN avoidance characteristic is not reproduced either.
    - **Early Disk Accretion.** The enriched material from MIBs and FRMS ejecta would be swept up by the protoplanetary disks of stars with M $< 2M_{\odot}$ and eventually accreted onto the host star (Bastian et al., 2013). In order to mix the accreted material throughout the star, the latter must be fully convective, limiting the accretion timescales to 13 Myr and therefore the amount of processed material that can be accreted.

---

[1] Bondi accretion concerns the supersonic motion of a point mass through a gas cloud. The cloud is assumed to be free of self-gravity, and to be uniform at infinity. Gravity focuses material behind the point mass, which can then accrete some of the gas (Edgar, 2004).

- **SMSs.** Within a young GC the most massive stars fall towards the center as a result of dynamical friction, leading to the formation of a SMS with a mass of $\sim 10^4\ M_\odot$, which could be continuously rejuvenated by stellar collisions, so that the amount of material ejected by the SMS can be 10x higher than its mass (Denissenkov et al., 2013). SMS are characterized by luminosities close to the Eddington limit, which refers to the maximum luminosity a body can achieve when in hydrostatic equilibrium between the force of radiation acting outward and the gravitational force acting inward. When a star exceeds the Eddington luminosity, it will initiate a very intense radiation-driven stellar wind from its outer layers (Marle et al., 2008), allowing for a consistent mass loss. As the SMS evolve their winds would be progressively enriched in He and products of CNO cycling and p-processes reactions so that 2G stars formed in the observed range of compositions.
  The SN avoidance characteristic is unexplained by this polluter.

Despite the observational efforts made to clarify which one of the two mechanisms produced the MPs and from which polluter, no firm answer has been provided yet, and no current formation scenario is able to justify all the observational features of 1G and 2G stars.

1.3 ANOMALOUS GLOBULAR CLUSTERS

The GCs that host the 1G and 2G stars discussed so far are the so-called Type I. A subclass of Galactic GCs is, on the other hand, referred to as Type II. This latter group of clusters (also known as Anomalous Globular Clusters (AGC)), constitutes about one fifth of the Galactic GCs, and are characterized by an additional population which defines a fainter SGB and a redder RGB than the bulk of 1G and 2G stars (which, as opposed to the anomalous stars, will be refered to as canonical stars), and a redder distribution of stars in the ChMs (Milone et al., 2017; Piotto et al., 2012).

Spectroscopy then revealed that the origin of these different sequences is again caused by chemical inhomogeneities, but this time regarding heavier elements that the ones involved within canonical stars. In particular, s-process elements[2], such as barium and lantanium, and iron content are present in a larger amount among anomalous stars. In addition, a total C+N+O enhancement has been observed in stars of this population with respect to the canonical stars (Yong et al., 2008; Carretta et al., 2010; Marino et al., 2011; Marino et al., 2015).

In **Fig. 1.2**, the Color-Magnitude Diagram (CMD) and the ChM of the Type II GCs NGC 1851 are shown. The left and central panels display the m_{F336W}-m_{F814W} color from HST bands and the U-I in Johnson-Cousins' photometric bands, respectively, which cover similar spectral ranges (from Dondoglio et al., 2023). In both diagrams, a split SGB and RGB sequence are well visible, with the canonical and anomalous stars describing the blue and red sequence, respectively. The right panel illustrates the ChM from Milone et al. (2017) in which anomalous stars form the distribution of stars at the largest $\Delta_{\mathrm{F275W,F814W}}$. This latter population is not present in the ChM of Type I GCs, like in the ones presented in **Fig. 1.1**. In **Fig. 1.3**, the case of ω Centauri is portrayed, the most complex Type II GC known to date. From the optical CMD (left panel), it is already possible to identify multiple RGB, spanning a wide color interval. This is indeed due to the presence of large metallicity variation (~1.5 dex) within this cluster stars (Marino et al., 2009a; Mucciarelli et al., 2018). The ChM derived by Milone et al. (2017) reflect this large complexity. Indeed, the canonical stars form the bluest branch at $\Delta_{F275W,F814W} \lesssim 0$, while anomalous stars occupy a very wide area, extending from $\Delta_{F275W,F814W}$ 0 up to ~2. The distribution of these stars clearly indicates that large chemical inhomogeneities are present among ω Centauri anomalous population. Milone et al. (2017) estimated that this GCs harbors 16 different stellar populations.

---

[2] The slow neutron-capture process, or s-process, is a series of reactions in nuclear astrophysics that occur at relatively low neutron density and intermediate temperature conditions in stars, particularly asymptotic giant branch stars. Under these conditions the rate of neutron capture by atomic nuclei is slow relative to the rate of radioactive beta-minus decay. A stable isotope captures another neutron; but a radioactive isotope decays to its stable daughter before the next neutron is captured. The s-process is responsible for the nucleosynthesis of approximately half the atomic nuclei heavier than iron, and therefore plays an important role in the galactic chemical evolution. The s-process differs from the more rapid r-process of neutron-capture by its slow rate of neutron captures.

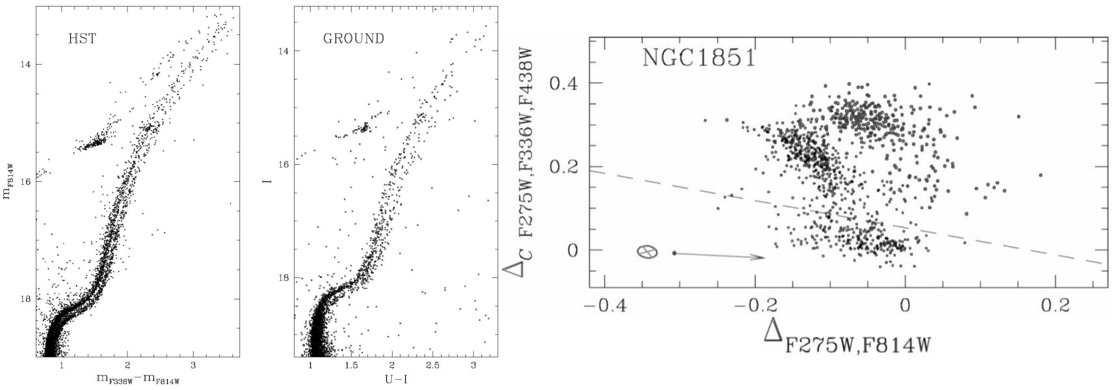

Figure 1.2: CMD and ChM of the GC NGC 1851 from Dondoglio et al., 2023 and Milone et al., 2017 respectively.

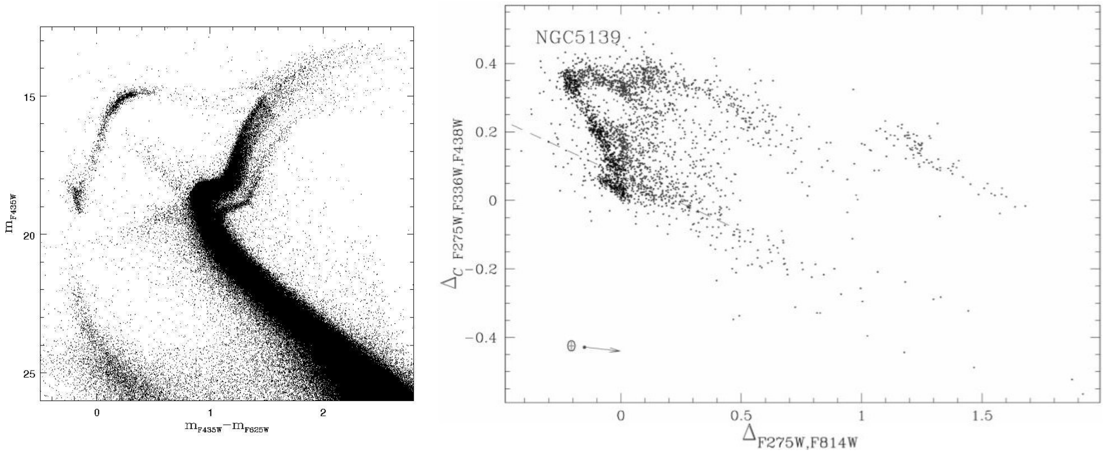

Figure 1.3: CMD and ChM of the GC NGC 5139 (or ω Cen) from Bellini et al., 2017 and Milone et al., 2017 respectively.

The origin of anomalous stars, and their link with the formation of MSPs in GCs, is currently unknown. An appealing hypothesis regarding their origin is that they are the remnants of larger structures, likely DG, with a more complex formation history than Type I GCs that allowed the formation of populations with differences in heavy elements abundances. The original DG were eventually accreted by the Milky Way, with only their nuclei -what are now the Type II GCs- surviving up to the present. This idea is corroborated by the fact that the Type II GC NGC 6715 lies at the center of the Sagittarius DG and by the observation of a halo extended up to several times the tidal radius surrounding NGC 1851, which would be the remnant of the original DGs (Bellazzini et al., 2008; Olszewski et al., 2009; Sollima et al., 2012; Marino et al., 2014). This plausible hypothesis could indeed account for the MSP in cosmology[3].

1.4 The Target of this Thesis: M22

The target of the present study is the GC M22 (or NGC 6656), with its estimated central region located at *RA* 18d36m23.94, *DEC* -23:54:17.1, which was one of the first globular clusters discovered, by Abraham Ihle in 1665. With an estimated mass of 10^5 to 10^6 $M_\odot$ and a relatively bright apparent magnitude of 5.1, M22 is a very remarkable object.

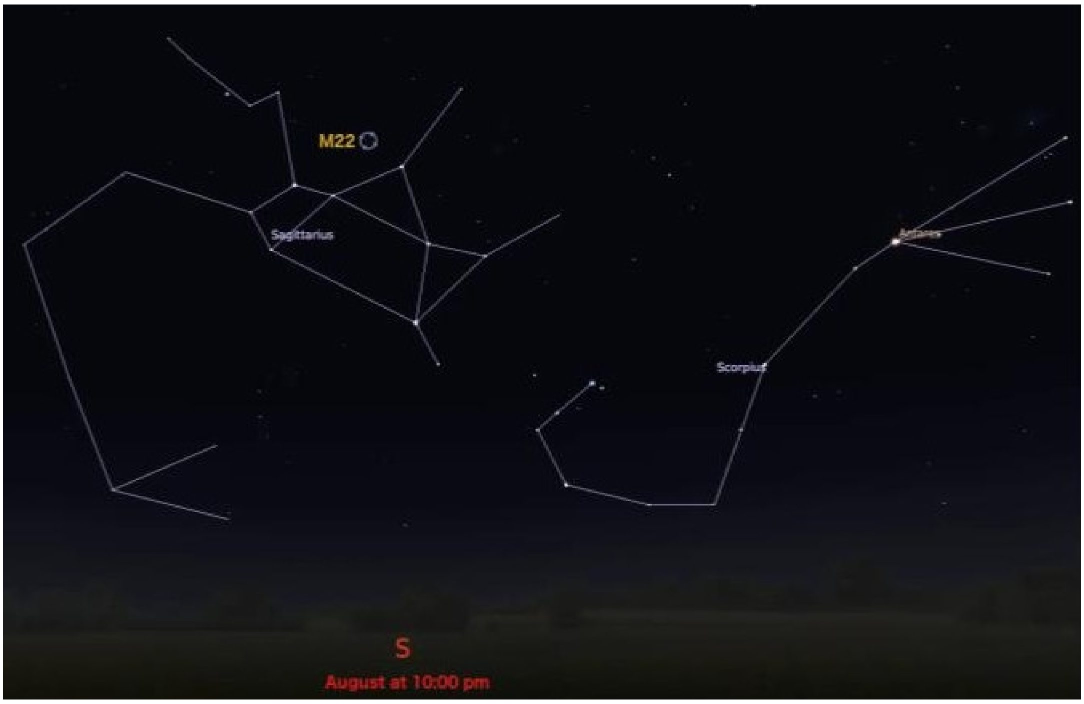

Figure 1.4: Located in the Sagittarius constellation as seen from Earth, in ideal conditions, M22 can be seen with the naked eye. The best time to observe the cluster is during August (*Messier 22 - NASA Science — science.nasa.gov* n.d.).

At about 3.2kpc , it is one of the nearest GCs. At this distance, it has an

---

[3] The MSP broadly refers to the overabundance of predicted Cold Dark Matter sub-halos compared to satellite galaxies known to exist in the Local Group. The current Λ Cold Dark Matter (ΛCDM) model of cosmology predicts that dark matter clusters hierarchically, so ever increasing number counts for smaller-and-smaller-sized halos is expected, promoting a large number of DG orbiting a bigger galaxy, as is the case of the Magellanic Clouds orbiting the Milky Way. Though DGs are known to orbit large galaxies, the number of the former is orders of magnitude below expected from simulations. Assuming re-ionization suppressed star formation in small dark matter halos, many faint DGs should be seen.

angular diameter of 32′, which makes it appear slightly larger than Full Moon in the night sky, though it possesses a half-light radius of 3.36′ making evident the central concentration of stars. It is visible to the naked eye for observers at not too northern latitudes, as it is outshined only by the two bright southern GCs ω Cen (NGC 5139) and 47 Tuc (NGC 104). From the rough count of its 70,000 stars, amounting to a mass of $\log \frac{M}{M_{\odot}} \sim 5.5$ (Marino et al., 2012), of which the brightest are about mag 11, only the relatively small number of 32 variables has been identified. The stars are spread over a region ~ 200 ly (0.06kpc) in diameter, and receding from us at about 149 $\frac{km}{s}$.

M22 is a Type II GC, revealed both by photometric and spectroscopic studies. Indeed, this cluster displays a split SGB and RGB sequences, which stars are enriched in [Fe/H], s-process elements, and total C+N+O abundances (Piotto et al., 2012; Milone et al., 2017; Marino et al., 2011; Marino et al., 2012; McKenzie et al., 2022). The various chemical anomalies of M22 stars indicate that this GC has undergone a complex, and still unclear, chemical enrichment history. Similarly to ω Cen, Fe and Ca variations suggest that core-collapse supernovae have had a role in the pollution of the intra-cluster medium from which the present generation of slightly Fe-enriched stars formed (Smith, 2003; Tsujimoto et al., 2003).

M22 has been compared to other clusters such as NGC 1851, since both share similar heavy element spreads (Roederer et al., 2011, Cordoni et al., 2023, and Dondoglio et al., 2023 which largely inspires the present work). For the latter, Carretta et al., 2010 and Tautvaiien et al., 2022 support the possibility of merging clusters resulting in abundance spreads. Given the chemical similarities between M22 and NGC 1851 it could be plausible to hypothesize that M22 is also the result of two merging clusters. Lee, 2019 decomposes M22 into five different populations, three of them belonging to the anomalous population; and finds, through the analysis of Cumulative Radial Distributions, that more metal-rich sub-populations are more centrally concentrated than metal-poor ones, with both canonical and anomalous populations having similar radial behaviour.

The origin and complex evolution history of M22 -and other Type II GCs- is still uncertain, with internal enrichment, cluster merging and DG nucleus hypotheses still valid contenders; what is certain and proven once again in the present results is the presence of distinct stellar populations that generate a chemical spread in the GC.

This GC is an ideal target to perform a photometric study on its anomalous stars, since it is one of the well-known Type II GCs with a wide range of spectroscopic studies, thus allowing us to combine information from both techniques, and has multiband data available from different facilities, allowing to study its anomalous populations along the whole Field of View (FoV) of M22.

1.5 Outline and purpose of the thesis

The aim of the thesis is to hint at the true origin of M22 via photometric and spectroscopic characterization, in order to contribute necessary information to eventually decipher its formation and evolution history so as to eb able to classify it either as a true GC or else as a DG remnant. To do so, the general chemical composition of its components is derived via chromosome mapping and verified with spectroscopic data for a small subset of stars. The outline of the thesis is as follows:

- **Chapter 1.** Provides a brief introduction to GCs and describes the MPs phenomenon. An introduction to the target GC of the present study is also provided.

- **Chapter 2.** Describes in detail the dataset processing, from description of the instrumentation used to the photometric and astrometric data reduction performed.

- **Chapter 3.** Illustrates the data analysis from CMDs to ChM and the main insights of the thesis.

- **Chapter 4.** This chapter summarizes the results of this work, including a comparison with the most recent works in literature and a brief discussion of the implications of the results obtained.

2

Data reduction

In this chapter, a brief explanation of the HST instrumentation is provided in **Sec. 2.1**, followed by a description of the different datasets involved in the present work in **Sec. 2.2**. The remainder of the chapter focuses only on the first dataset and the process to derive an accurate Point Spread Function (PSF). In **Sec. 2.3** the concept of PSF photometry is introduced. Afterwards, the process of obtaining clean, apparent magnitude data in GAIA reference system out of instrumental magnitudes in the local (HST) CCD reference system is explained thoroughly in **Sec. 2.4**. Finally, once data has been reduced, the calibration and correction for differential reddening processes are detailed in **Secs. 2.5** and **2.6**.

2.1 HST INSTRUMENTATION

The HST, launched by NASA in 1990, has changed our fundamental understanding of the universe. It travels in a Low Earth Orbit avoiding atmospheric distortion and thus allowing us to obtain high-resolution images, which, as opposed to ground-based telescopes, can detect photons in wavelengths that are inaccessible for the latter due to atmospheric scattering; this paves the way for the measurement of accurate position and magnitude of stars in order to explore very crowded regions, as is the case of GCs.

HST has a primary mirror of 2.4 m and covers a wide range of wavelengths, from ~ 100 nm to ~ 1700 nm through a variety of instruments and filters. As of today, the instrumentation in service is the following (Space Telescope Science Institute, 2024):

Advanced Camera for Surveys (ACS) is designed to provide deep, wide-field survey capability via the 16 megapixel camera, from the near-UV to the near-IR with the PSF critically sampled at 6300 Å. ACS consists of three channels:

- High Resolution Channel (HRC), with FoV = 29.1 × 26.1 $arcsec^2$, with wavelength coverage range of 200 - 1050 nm and with plate scale ps = 0.027 $^{arcsec}/_{pix}$.

- Solar Blind Channel (SBC), with FoV = 34.59 × 30.8 $arcsec^2$, with wavelength coverage range of 115 - 180 nm and with ps = 0.032 $^{arcsec}/_{pix}$.

- Wide Field Channel (WFC), with FoV = 202 × 202 $arcsec^2$, with wavelength coverage range of 350 - 1050 nm and with ps = 0.05 $^{arcsec}/_{pix}$. It is worth noting that the ACS/WFC CCD is composed of two separated rectangular CCDs.

ACS was installed during the 2002 servicing mission and is today the most heavily used HST instrument.

Cosmic Origins Spectrograph (COS) is a fourth-generation instrument that was installed on HST during the 2009 servicing mission; it was designed to perform high sensitivity, moderate- and low-resolution spectroscopy of astronomical objects in the 115 - 320 nm wavelength range. COS has a far-UV and near-UV channel that use different detectors: two side-by-side 16384 × 1024 pixel Cross-Delay Line Microchannel Plates (MCPs) for the far-UV, 115 - 205 nm, and a 1024 × 1024 pixel cesium telluride Multi-Anode Microchannel Array (MAMA) for the near-UV, 170 - 320 nm.

Space Telescope Imaging Spectrograph (STIS) can study properties of celestial objects as chemical composition and abundances, temperature, radial velocity, rotational velocity, and magnetic fields across a spectral range from the UV through the visible red and the near-IR (115 - 1000 nm). STIS uses three detectors: a cesium iodide photocathode MAMA for 115 - 170 nm, a cesium telluride MAMA for 165 - 310 nm, and a CCD for 165 to 1000 nm. All three detectors have a 1024×1024 pixel format. The FoV for each MAMA is 25×25 arc-seconds, and the FoV of the CCD is 52×52 arc-seconds.

Wide Field Camera 3 (WFC3) is also a fourth generation instrument installed during the 2009 servicing mission. Provides wide-field imaging with continuous spectral coverage from the ultraviolet into the infrared, dramatically increasing both the survey power and the panchromatic science capabilities of HST. The WFC3 has two camera channels: the UVIS channel that operates in the UV and visible bands (from about 200 to 1000 nm), and the IR channel that operates in the infrared (from 900 to 1700 nm). The performance of the two channels was designed to complement the performance of the ACS.

Fine Guidance Sensors (FGS) in addition to being an integral part of the HST Pointing Control System (PCS), provides precision astrometry and milliarcsecond resolution over a wide range of magnitudes ($3 < V < 16.8$). Its two observing modes - Position Mode and Transfer Mode - have been used to determine the parallax and proper motion of astrometric targets to a precision of 0.2 mas, and to detect duplicity or structure around targets as close as 8 mas (visual orbits can be determined for binaries as close as 12 mas).

For the present work, the data reduction technique was employed on images from the ACS instrument.

2.2 Datasets and data reduction tools

Five sets of data were used for the totality of the present work. Three of them are space-based from HST, while the fourth and fifth datasets contain Ground Based (GB) photometric and spectroscopic observations respectively.

2.2.1 Dataset 1: HST observations for data reduction

Dataset 1 was downloaded from MAST[4] and was used for data reduction. The dataset consists of the currently latest science frames taken with ACS in F475W and F814W filters; which correspond to observations from October 10th, 2020 by PI Calamida with Proposal ID 16177. A summary of the image sets is presented in **Table 2.1**.

---

[4] Barbara A. Mikulski Archive for Space Telescopes search for HST data accessed on February 2024 at https://mast.stsci.edu/search/ui/#/hst

ROOTNAME	**jeaa01uaq**	**jeaa01uqq**	**jeaa01uqq**	**jeaa01v2q**
TIME_OBS	03:32:35	04:10:50	05:07:23	05:47:30
RA_TARG	18d36m27s1	18d36m27s1	18d36m27s2	18d36m27s2
DEC_TARG	-23:54:01.9	-23:54:03.0	-23:54:01.8	-23:54:01.7
FILT	F814W	F814W	F475W	F475W
EXPT	150	230	250	150

Table 2.1: Data reduction image sets.

Image types:

- DRC: corrected, calibrated and combined images, used for obtaining apparent magnitude calibrated to Vega.
- FLT: images not corrected for Charge Transfer Efficiency (CTE), which is the fraction of charge which is successfully transferred during one CCD transfer cycle.
- FLC: images corrected for CTE (as well as for BIAS and FLATS).

2.2.2 Dataset 2: GAIA observations for proper motion

The GAIA satellite was launched by ESA in on December 19th, 2013, and has since been creating an extraordinarily precise three-dimensional map of more than a thousand million stars throughout our MW galaxy and beyond, mapping their motions, luminosity, temperature and composition.

GAIA has its roots in ESA's Hipparcos mission (1989-1993), which catalogued more than 100,000 stars to high precision, and more than a million to lesser precision. GAIA measures each star's position and motion 200 times more accurately than Hipparcos, and produces data for 20,000 times more stars. The name GAIA was originally derived as an acronym for Global Astrometric Interferometer for Astrophysics.

GAIA's payload consists of a single integrated instrument the design of which is characterised by:

- A dual telescope concept, with a common structure and a common focal plane. Beam combination is achieved in image space with a small beam combiner.

- Silicon-carbide (SiC) ultra-stable material is used for mirrors and telescope structure.
- A highly robust measurement system for the Basic Angle between the two telescopes' pointing directions.
- A large common focal plane with an array of 106 CCDs. The large focal plane also includes areas dedicated to the spacecraft's metrology and alignment measurements.

The instrument has the following functions:

- **Astrometry**: accurate measurements, even in densely populated sky regions of up to 3 million stars per square degree. The astrometric field in the focal plane is sampled by an array of 62 CCDs, each read out in time-delayed integration mode synchronized to the scanning motion of the satellite.
- **Photometry**: continuous spectra in the band 330-1050 nm for astrophysics and chromaticity calibration of the astrometry.
- **Spectrometry**: high resolution, grating, narrow band: 845-872 nm.

The spacecraft operates in a continuously scanning motion, such that a constant stream of relative angular measurements is built up as the FoVs sweep across the sky. High angular resolution provides high positional precision in the scanning direction. The wide-angle measurements provide the high rigidity of the resulting reference system (ESA, 2013).

Dataset 2, extracted from DR3[5] was downloaded matching the FoV of HST ACS/WFC. Since **Dataset 1** observations are strongly contaminated by field stars on the same line of sight, the purpose of **Dataset 2** is to filter out these stars (not belonging to the GC), as detailed description of this process is given in **Sec. 2.4.6**.

2.2.3 DATASET 3: LEGACY HST OBSERVATIONS

Given that **Dataset 1** is limited to the mentioned filters, **Dataset 3** was used instead to account for the required set of filters for the intended analysis via

---

[5] GAIA Data Release search at https://gea.esac.esa.int/archive/

ChMs.
This dataset was reduced by Milone et al. (for more detail refer to *The Hubble Space Telescope UV Legacy Survey of Galactic globular clusters* paper series by Milone et al.) and includes the data from calibrated images in F275W, F336W, F395W, F438W, F467W, F475W, F502W, F547W, F606W, and F814W filters.

2.2.4 DATASET 4: GROUND-BASED OBSERVATIONS

Dataset 4, consists of data from wide-field ground-based observations, from now on referred to as **"GB"**, in the UBVRI Johnson-Kron-Cousins passbands. Specifically, data was collected through the U filter of the Wide-Field Imager (WFI) at the Max Planck 2.2m telescope at La Silla as part of the SUrvey of Multiple populations in GCs (SUMO) programme (088.A-9012-A by PI. A. F. Marino) (Monelli et al., 2013); and photometric data from the archive maintained by P.B. Stetson (Stetson, 2000) on B, V, and I filters, from observations made by many different observers using 10 telescopes at five sites (Kitt Peak National Observatory: 4 m, 2.1 m, 0.9 m; Cerro Tololo InterAmerican Observatory: 4 m, 1.5 m, 0.9 m; La Palma: Isaac Newton Telescope, Jacobus Kapteyn Telescope; Canada/France/Hawaii Telescope; and Wyoming Infrared Observatory) over the period from 1983 to 1999.

2.2.5 DATASET 5: SPECTROSCOPIC OBSERVATIONS

Dataset 5 consists of two **GB** sets of high-resolution spectra of RGB stars. The first set comes from APOGEE[6] with the Apache Point Observatory, 3.5 m telescope, ARC Echelle Spectrograph (Wang et al., 2003).

The second one, from Aguilera-Gómez et al., 2021, corresponds to spectra obtained with VLT-UVES[7] as part of the ESO program 095.D-0735 (PI. A. Mucciarelli), with observations carried out using UVES (Dekker et al., 2000), and FLAMES multi-object spectrograph (Pasquini et al., 2002).

---

[6] Apache Point Observatory Galactic Evolution Experiment, is a large-scale, NIR, high-resolution (R ~ 20,000) spectroscopic survey of Galactic stars. It is one of the four experiments in SDSS-III. APOGEE observations are carried out in the H band, with extinction six times smaller than in V, so provides a vast, uniform database of chemical abundances and radial velocities for stars across all Galactic populations (bulge, disk, and halo) (Prieto et al., 2008).

[7] ESO Very Large Telescope, Ultraviolet and Visual Echelle Spectrograph

2.2.6 Computational tools for PSF photometry

The following tools were employed during the data reduction process:

- `FORTRAN` routines by Anderson et al., 2006:
  - `drz_phot`
  - `img2xym`
  - `readheader`
  - `flt2wj2`
  - `img2psf`
  - `xym1mat`
  - `flt2wj2`
  - `xym1mat`
  - `img2psf`
  - `xym2bar`
  - `img2xym`
  - `xym2mat`
- `Supermongo` (Lupton et al., 1996)

2.3 PSF Photometry

HST images of GCs typically present stars as point-like sources, the appearance of each of these point-like sources is described by its PSF. Measuring the sharpness of the source allows us to determine whether the object found is truly stellar, a faint galaxy, or even a spurious detection such as a cosmic ray.

In performing PSF photometry we make 2 basic assumptions:

1. All point sources imaged can be represented by a PSF which can be modeled.

2. The imaging system is linear in the response to input radiation: when two objects A and B are imaged simultaneously, the result is equal to the sum of the independently imaged objects.

As a result of this linearity property, the image of any object can be computed by dividing the object into smaller parts, imaging each of these, and subsequently summing the results. If one divides the object into increasingly small parts, it is eventually a collection of infinitely small point objects. Each of these point objects produces a PSF in the image, shifted and scaled to the location and intensity of the corresponding point, respectively. The resulting image is therefore a collection of (often overlapping) PSFs (Heasley, 1999).

The shape of a star on the focal plane is called instrumental Point Spread Function (iPSF), but, as explained in Dondoglio, 2020, what we actually measure is the count registry for each pixel in the CCD array. A star image is therefore distributed over several pixels and the value of counts in each pixel centered at some offset (Δx, Δy) from the center of the iPSF, depends on the results of a convolution between the iPSF and the sensitivity profile of the pixels it lies on. The effective Point Spread Function (ePSF), as defined in Anderson et al., 2000, represents whatever results from the combination of the detector and iPSF, without assuming anything about any of them. Observers must understand the limitations and response behaviour of the detection systems. The ePSF gives directly the fraction of a star light that should fall in each pixel of a star image, from where the center of each pixel lies with respect to the center of the star. As opposed to the iPSF, which is discrete, the ePSF is a continuous function (and is also smoother).

In order to describe the point-like sources in the images, only three parameters are necessary: the center coordinates (X, Y) and the total flux (f). Deriving these parameters, starting from the 2-dimensional pixel array that is the image, is a crucial target for an high precision photometry. Finding out accurate positions requires an accurate PSF model; inaccuracies induce bias, called pixel-phase error, which depends on the location of the star within the pixel. The same stellar profile can be fitted with different PSF models. It is not straightforward to determine which one of the many consistent PSFs is actually the right one for the image in question. If the position of the star was somehow known, this might tie down the PSF model; however, this clearly cannot be known without recourse to an accurate PSF. The breaking of this degeneracy is a major challenge (Anderson et al., 2000).

The basic principle of PSF photometry is to identify the stars within the CCD image, determine the sky level behind them, use "isolated" stars to derive the PSF template, and then fit this template to all the stars in the frame. Star finding algorithms will sometimes fail to find faint stellar companions located next to bright stars; these can usually be found on a second pass through the image after the stars found in the first detection pass have been measured by the PSF fitting and subtracted from the image. By running the finding routine on the residual image, the stars missed on the previous pass will usually be located (Heasley, 1999).

2.4 DATA REDUCTION PROCESS

The ACS/WFC files contain the overlapped images of the two CCDs and therefore cannot be used directly. The two images can be disentangled using the `FORTRAN` routine `flt2wj2`, which creates an single image by aligning the two obtained from each CCD (Bortolan, 2022).

After having converted the images from FLC to WJC type, the following steps for data handling are followed:

2.4.1 DERIVE ePSF MODEL, USING A SUITABLE LIBRARY PSF AS BASELINE.

The routine `img2psf` fits a library PSF (Anderson et al., 2006) to the sources in a certain image that meet some criteria in order to derive a PSF model for the stars in each exposure. The criteria to be met by the sources are:

- **HMIN**. Isolation index (i.e. the minimum distance in pixels between two sources).
- **FMIN**. Minimum flux (in counts). A high value for this parameter is chosen in order to select bright sources.
- **PMAX**. Maximum flux. Allows to discard saturated sources (above the limit of 55000).
- **QMAX**. Maximum Q factor. The Q factor 'grades' how good the source fits to the model PSF. 0 is perfect fit, the higher the value the more the source departs from the model, this in practice means that the source is not a stellar one.
- **NSIDES**. Regions in which to divide the image. The more regions, the better the model, as long as there are enough stars in each region.
- **PSF.FITS** file. Library PSF model upon which to build the tailored model.
- **IMAGE.FILE** source file.

The routine output file contains the PSF model tailored to the chosen image. Note that the routine must be run independently for every image, of each filter. It is customary to try the process with different amounts of regions (**NSIDES**) until getting best ePSF model.

It is assumed that all stars have a common PSF and that it only changes in detector position because of charge-diffusion or optical aberrations, so the programme does not produce a single PSF model for the whole image but a grid of 9×10 ePSFs. The PSF model for any point in the detector is then obtained by interpolating the PSF among the four nearest grid points.

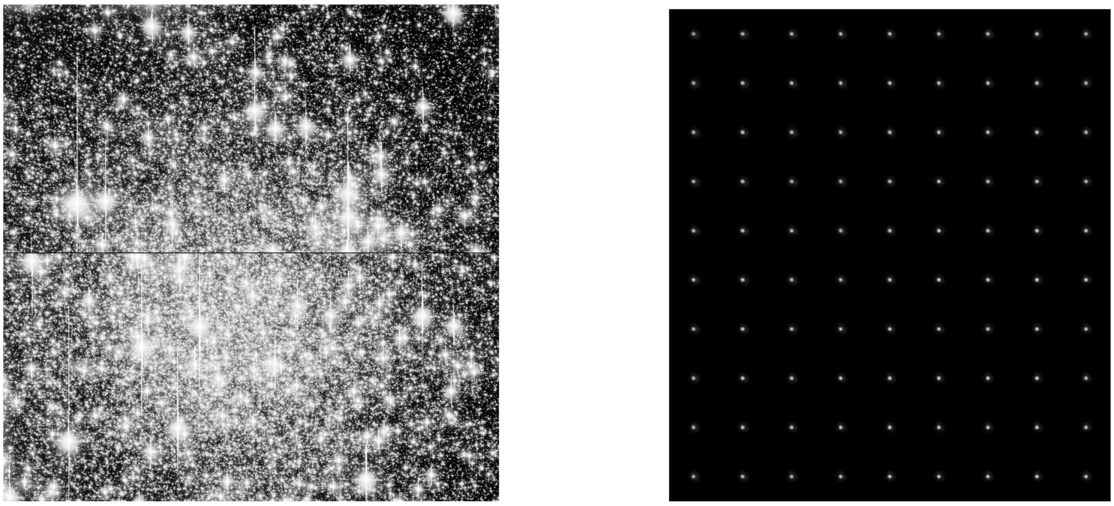

(a) jeaa01uaq image.

(b) Tailored ePSF grid.

Figure 2.1: ePSF

2.4.2 OBTAIN COORDINATES AND MAGNITUDE.

The ePSF model is applied to the sources in the image that meet Isolation index, Minimum and Maximum flux criteria using the routine `img2xym`. A large flux range allows to take into account all sources. The routine output file contains X and Y coordinates, instrumental magnitude and Q factor.

2.4.3 DISCARD UNWANTED SOURCES.

Stars follow a trend in which for brighter stars, the ePSF model has the best fit (Q factor close to 0), and as brightness dims out, the Q factor naturally increases. All sources that do not follow this trend must be discarded as they are not stars. On the other hand, sources brighter than the instrumental limit, which for ACS/WFC is a magnitude of ~ -13.7, are saturated sources which come in handy in the following steps. The output file contains the same information as before, for the selected sources only.

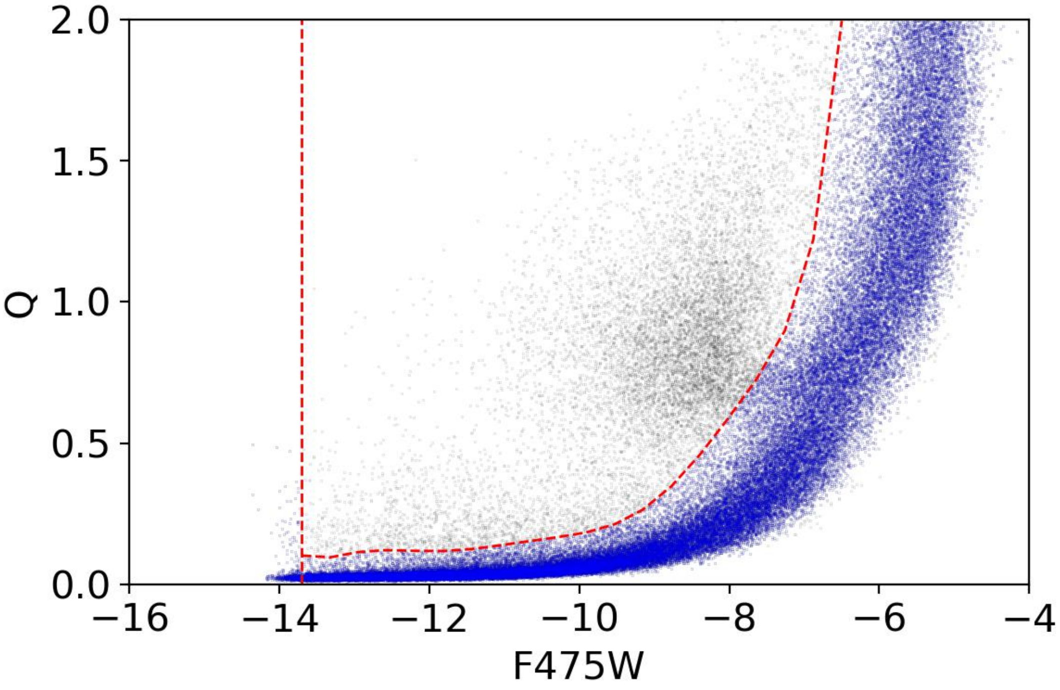

Figure 2.2: All sources below -13.7 mag are selected, for dimmer brightness, sources outside the visible trend are discarded. Blue points represent selected sources.

2.4.4 Transform images to a chosen reference frame.

To eliminate the slight shift in position and CCD response from image to image with respect to a chosen frame, the routine `xym2mat` is used, which requires a single argument, that is related to the distance in pixels from a source within which common sources are searched for; and an input file that contains the list of all images on which transformations are to be found, as well as specifications for instrument and filter of the images (for the present work **c5** (HST/ACS) and **f5** (F814W) or **f2** (F475W) were used accordingly). The chosen reference frame is customarily the image with largest exposure time since it will contain brighter sources.

The output files contain coordinates and their corresponding variations (X, Y, dx, dy) for each image with respect to the chosen reference frame.

The process is applied in a two-step manner, where in the first, a big radius is chosen.

It is necessary to find a proper radius before proceeding to the iteration. This is done by defining a radius that encircles the main density area in the *dx* vs. *dy* distribution. In the present work a 2σ radius was chosen, as shown in **Fig. 2.3**.

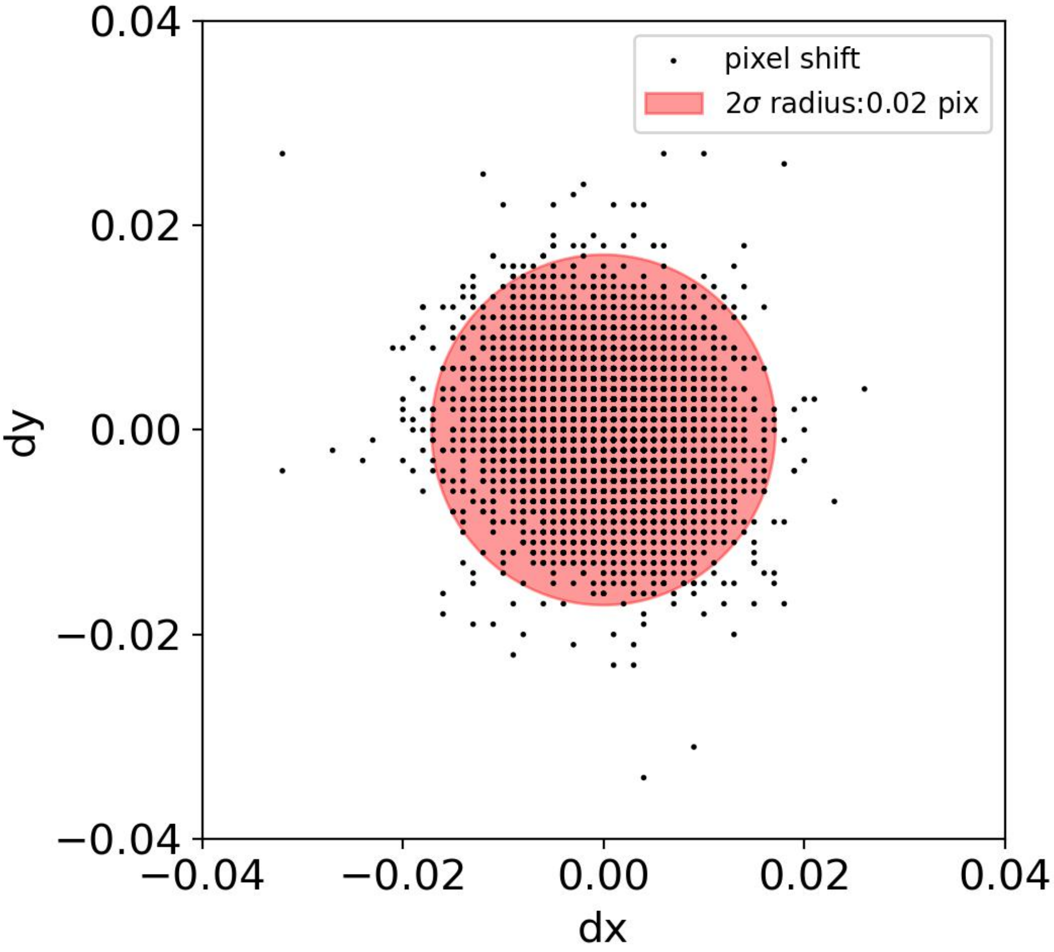

Figure 2.3: A 2 σ radius includes the central population density of the distribution.

Furthermore, as *sanity check*, the pixel shift as a function of CCD position was computed in order to verify that there is no CTE variation due to an unexpected CCD malfunction. This is shown in **Fig. 2.4**.

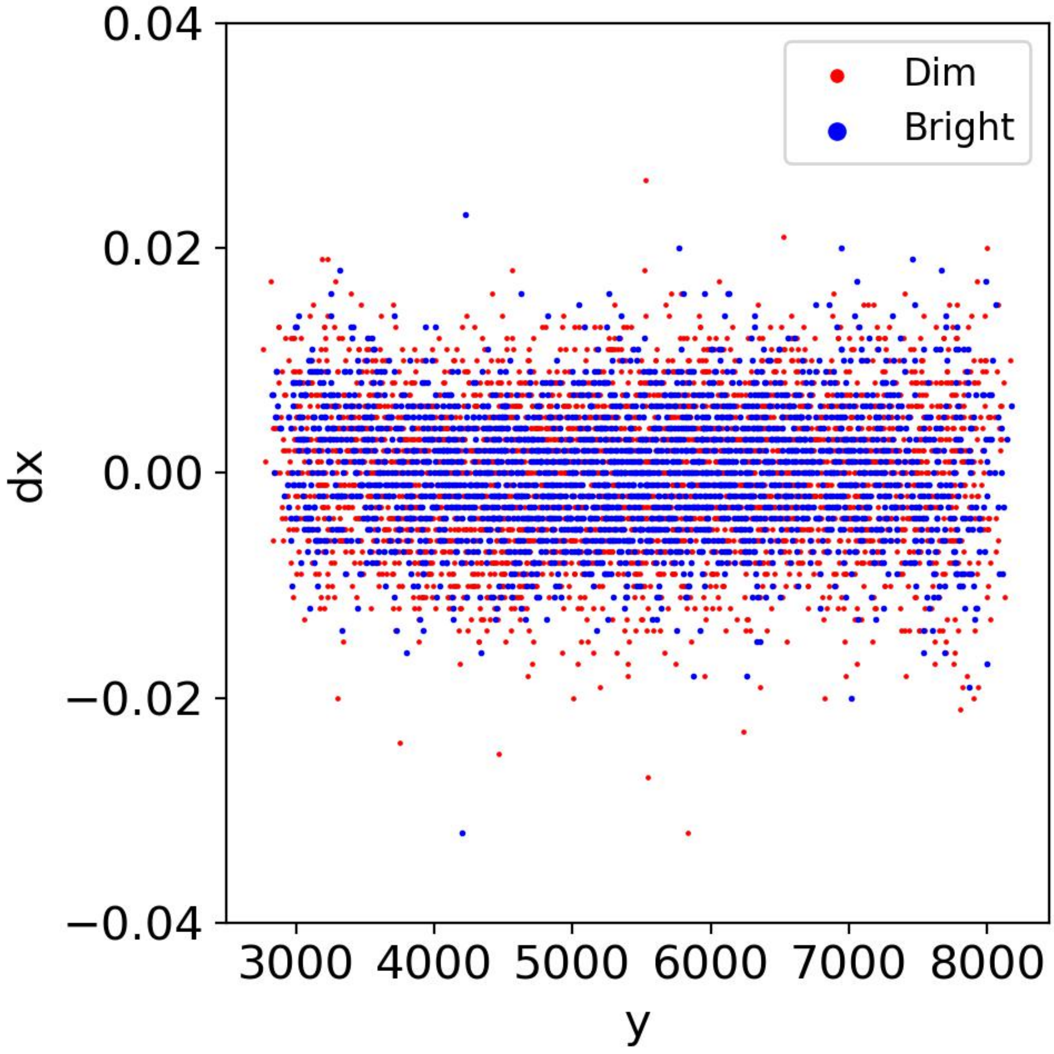

Figure 2.4: dx vs. Y plot shows that there is effectively no CCD malfunction, otherwise a non-Gaussian distribution along Y position would be seen.

The second step takes into account bright but not saturated stars, so the magnitude range was changed accordingly by adjusting it to a maximum brightness of -13.5 and a minimum of -12.2.

2.4.5 Generate a single catalogue.

The routine `xym2bar` superimposes all images in a chosen reference frame and calculates the average values of position and magnitude between the common stars. It requires a single parameter which is the amount of images in which a source must be found in order to be considered in the final catalogue, and a an input file containing the list of images and magnitude ranges. The output file contains the unified catalogue with X and Y coordinates, magnitude, and their respective measurement errors. The process must be ran for all filters.

2.4.6 TRANSFORM STAR COORDINATES TO ABSOLUTE REFERENCE FRAME.

TRANSFORM POSITIONS TO ABSOLUTE REFERENCE FRAME.

The absolute reference frame is the GAIA frame, whose positioning uses spherical coordinates expressed in *RA* and *DEC*, so it is necessary to transform the positions in the HST FoV plane, while keeping the original magnitudes from HST.

FIND COMMON STARS BETWEEN CATALOGUES.

For a single filter, a link between HST and GAIA catalogues is created in a 2 step process with the routine `xym1mat` which requires as parameters the 2 catalogue files (with the possibility of specifying a coordinate and magnitude range) of which the first one is considered the matcher (GAIA), and the second the matchee (HST); number of rejection iterations (which determines how consistent the positions have to be), and finally the minimum proximity to be considered in the link file. The chosen filter must be the one that includes the most stars, in this case F814W. The first step considers only saturated stars while the second step includes all stars.

CREATE MIXED CATALOGUE.

For the selected filter, a catalogue is created such that for each common source, the previously transformed coordinates and the original magnitude measured are considered.

FIND REFERENCE SYSTEM TRANSFORMATIONS FOR REMAINING HST IMAGES.

For each HST image in the selected catalogue, a transformation to GAIA reference system is found with the routine `xym2mat`. The routine is implemented in the same 2-step manner as explained in **Sec. 2.4.4**, but using the output file catalogue from the previous step as matcher (note that instrument and filter must be null-specified as **c0** and **f0** since the image is NOT anymore an HST image but a processed one).

CREATE A CATALOGUE FOR COMMON STARS.

The routine `xym2bar` is used as explained in **Sec. 2.4.5** with the same input file. The output file is considered the master file for the filter, which will be used to find a final catalogue file.

ITERATE TO FIND FINAL CATALOGUE.

Since the master file includes only common HST-GAIA stars, many other stars are effectively lost in the process; due to HST images having a lot more sources since are deeper than GAIA's, to find transformations in order to create the final catalogue, it is necessary to iterate the two previous steps using the master file as matcher. The output is a final matchup file.

TRANSFORM REMAINING FILTER CATALOGUES.

The filter F814W was used to transform to GAIA reference because has more stars, while the rest of filters need not to be transformed with the GAIA catalogue but are rather transformed making use of the final matchup file from the F814W filter. The process of connecting the remaining filter catalogues to the one transformed to GAIA reference system is the same as explained in **Sec. 2.4.6** but using the F814W matchup file as master. In a nutshell, the master catalogue in the chosen filter (F814W) is related to GAIA, while the catalogues in the remaining filters are related to the final matchup in the first filter. In the present exercise, only filter F475W is considered. Steps from **Secs. 2.4.4** through **2.4.6** are performed for F475W images to reach the final catalogue matchup as output in this filter.

2.5 CALIBRATION.

Once matchup files for each filter are obtained, the position is taken as definitive but magnitude is yet to be calibrated as up to this step they are still instrumental magnitudes that have no physical meaning. The calibrated magnitude is given by:

$$m_{calibrated} = m_{instrumental} + \Delta_{mag} + ZP_{filt} + C \tag{2.1}$$

where $m_{instrumental}$ is the magnitude that has been used up to this step, Δ_{mag} is the difference between PSF and aperture photometry magnitudes, ZP_{filt} is the zero-point for a given filter and C is the aperture correction.

The zero point of an instrument, by definition, is the magnitude of an object that produces one count per second. It is the setting of the zeropoint, then, which determines the connection between observed counts and a standard photometric system (such as Cousins RI), and in turn between counts and astrophysically interesting measurements such as the flux incident on the telescope (Stevens, 1997).

The aperture correction C is defined as:

$$C = 2.5log(EE) \tag{2.2}$$

where EE refers to fractional encircled energy as function of aperture radius and filter, as shown in **Fig. 2.5**, which can be obtained from the Space Telescope Science Institute[8]. The data table was derived by Bohlin (2016) according to the following logic:
for an aperture photometry with a radius of i, the EE fractions EE_i are the average of the measured count rate inside i, N_i, divided by the measured instrumental count rate N_e in $\frac{photoelectrons}{s}$ in the ACS "infinite" 5.5" radius aperture:

$$EEi = Ni/Ne \tag{2.3}$$

for each filter (i.e. the sum of the N_i $\frac{counts}{s}$ within a radius i divided by N_e). N_e implicitly includes all the detected photons in an infinite radius aperture. Though an actual infinite radius is not feasible, a 5.5" is about as large an aperture as is practical. In principle, models of the iPSF could help define EE but these are generally not good past a radius of $\sim$ 2" due to effects of scatter and high-frequency aberrations.

The aperture photometry magnitude $m_{aperture}$ is found using the routine `drz_phot`, which measures the aperture magnitudes of the DRC images (See **Sec. 2.2.1**) at an exposure time of 1 sec, so that the values for each pixel are the actual number of $\frac{counts}{s}$.

Finally, in order to find Δ_{mag}, a range of magnitudes where stars are brightest and best measured is considered in the $m_{aperture}$ vs. $m_{instrumental}$ plot (marked with red points in **Fig. 2.6**), with the objective of finding an adequate reference value of the distribution.

In an iterative fashion, a $N\sigma$ portion of the distribution is chosen around the reference value (median of the distribution in the considered range), the standard deviation is computed and so the reference value is changed until a desired precision is reached. In this work the process was done starting from a

---

[8] https://www.stsci.edu/hst/instrumentation/acs/data-analysis/aperture-corrections

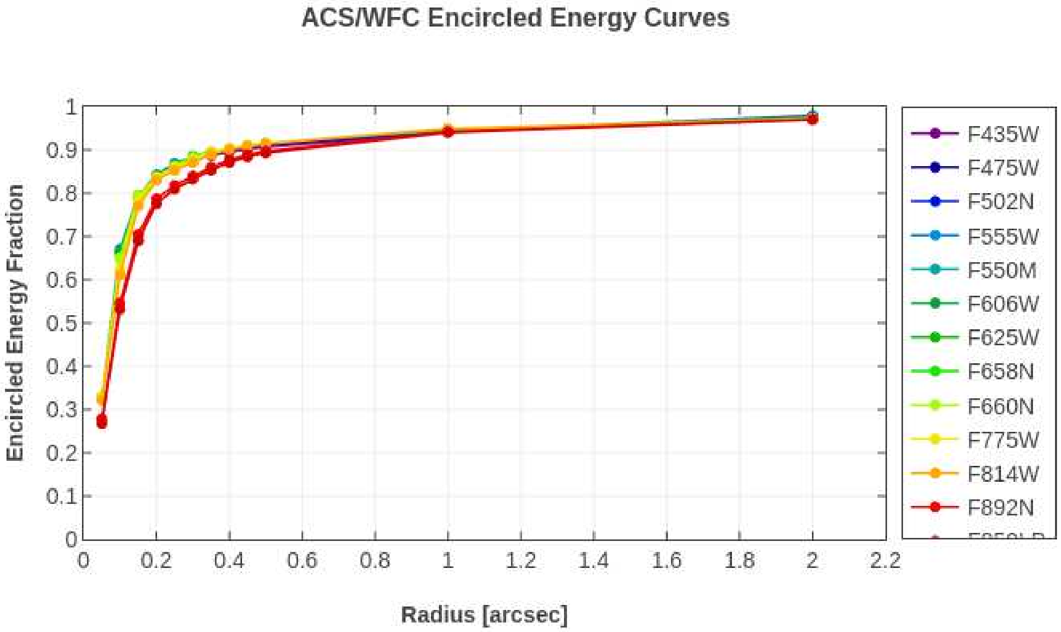

Figure 2.5: The encircled energy values are used to compute the aperture corrections required to account for flux falling outside an aperture of radius i, where i is less than the "infinite" aperture. For WFC, the infinite aperture radius is defined to be 5.5". Plot taken from Space Telescope Science Institute, 2024

4σ distribution and arriving to a 2σ distribution as seen in **Fig. 2.6**.

The three constants found are then added as a single calibration constant to the instrumental magnitude values for each filter catalogue as:

$$C_{calibration} = \Delta_{mag} + ZP_{filt} + C \tag{2.4}$$

The calibration constants found are:
$C_{calibration}$ = 5.907 + 25.503 - 0.098 = 31.312 for F814W and
$C_{calibration}$ = 6.000 + 26.148 - 0.100 = 32.048 for F475W.

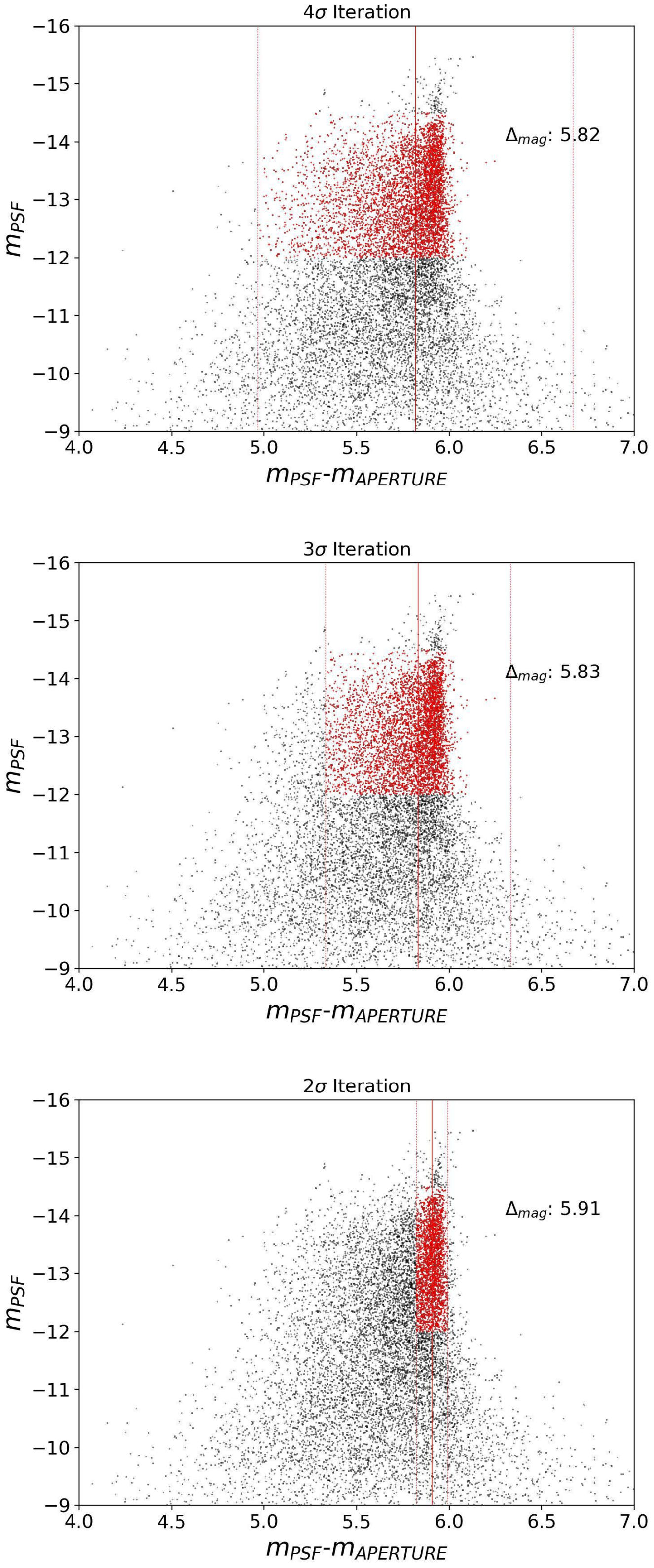

Figure 2.6: Iterative calibration process for finding Δ_{mag}.

2.6 Differential reddening correction.

Differential reddening is caused by interstellar extinction due to the presence of molecular clouds and dust, which depends on the density of absorbents present along the line-of-sight. This absorption is a function of the considered spectral range, being larger at smaller wavelengths. The reddening vector defines the direction of this effect on the CMD plane; for the case of the m_{F814W} vs. (m_{F475W}-m_{F814W}) diagram:

$$R_v = \sqrt{A^2_{F814W} + (A_{F475W} - A_{F814W})^2} \tag{2.5}$$

where A_{F475W} and A_{F814W} are the F475W and F814W ACS bands' absorption coefficients, corresponding to the average reddening for observations in a given band X (with X=F475W, F814W in this case), A_X, defined as the difference between the apparent magnitude m_X and the original magnitude m_0

$$A_X = m_X - m_0 \tag{2.6}$$

To obtain the difference in magnitudes, since the original magnitude is unknown, it is possible to resort to the color excess, which is the difference between apparent magnitudes in 2 bands X_1 and X_2. If $X_1 = B$ and $X_2 = V$:

$$E(B - V) = A_B - A_V \tag{2.7}$$

Then, a relation between A_X and *E(B-V)* is given by

$$A_X = k_X E(B - V) \tag{2.8}$$

Where k_x depends on the wavelength and its value can be retrieved from the online catalogue for all the filters of HST. The interstellar reddening is not constant, but changes with the direction of the line of sight. Small *E(B-V)* differences across the FoV of an observation can arise, leading to the so-called differential reddening effect, which spreads the typical evolutionary sequences of the CMDs, thus negatively affecting the information that photometry can provide. To minimise its impact, the procedure for differential reddening correction by Milone et al. (2012b) has been applied to the m_{F814W} vs. (m_{F475W}-m_{F814W}) CMD, assuming $k_{F475W} = 3.743$ and $k_{F814W} = 1.842$.

This method is explained in **Fig. 2.7**, using NGC 2298 as a template, and follows these steps:

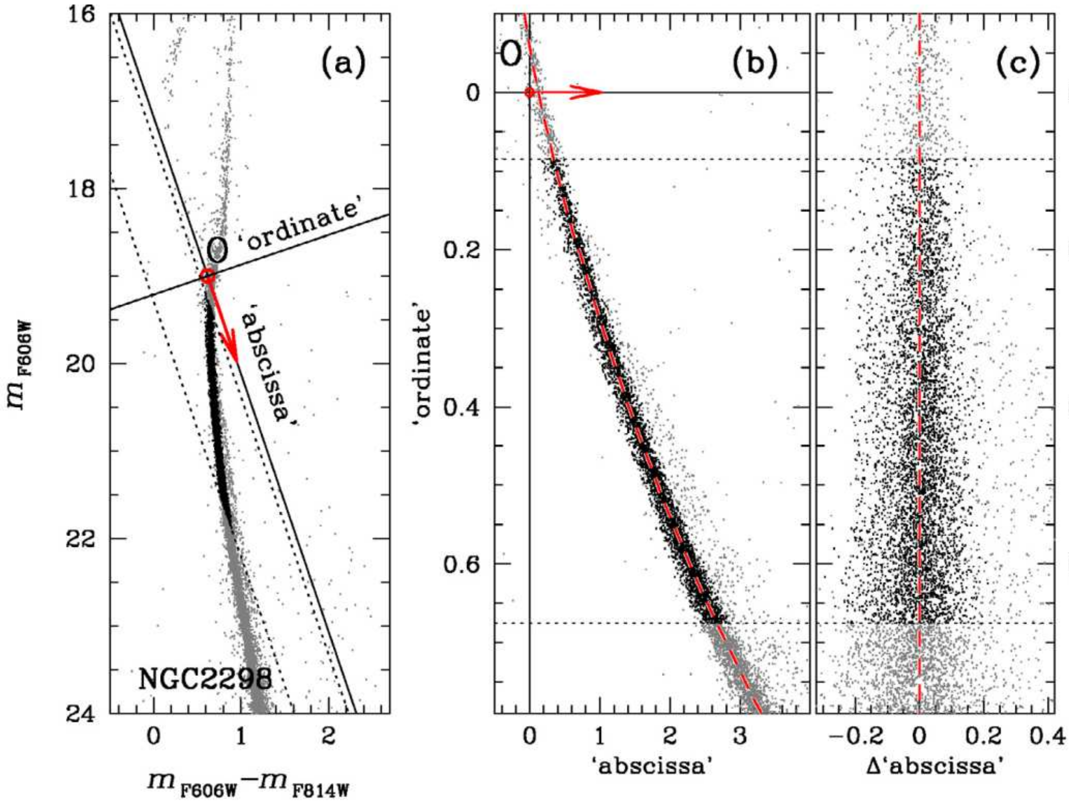

Figure 2.7: *Panel (a)*: CMD of NGC 2298; the arrow indicates the direction of reddening. The continuous lines are the axes of the introduced reference frame. *Panel (b)*: the position of stars in the this reference, where the fiducial line of the MS is drawn as a dashed red line. Stars between the dotted lines (in black) are used as reference stars. *Panel (c)*: verticalized "ordinate" vs. Δ"abscissa" diagram. Taken from Milone et al., 2012b.

1. A selection of sample stars from the high MS to the Main Sequence Turn-Off (MSTO) has been performed, avoiding obvious binary stars, like done in *panel (a)* of **Fig. 2.7**, where the sample of stars in indicated in black. Here, the reddening vector is indicated with a red arrow.

2. A new reference frame is defined, with its two axis, "abscissa" and "ordinate", parallel and perpendicular to the reddening vector respectively, as portrayed in *panel (b)*. This new photometric reference frame is centered at an arbitrarily defined origin (O), near the MSTO in the CMD, and obtained by rotating counterclockwise on the CMD plane by an angle:

$$\theta = arctan\frac{A_{F475W}}{A_{F475W} - A_{F814W}} \tag{2.9}$$

3. A fiducial line (dotted, colored in red in *panel (b)*) is derived only for the selected MS stars by dividing the sample into "ordinate" bins of 0.4 mag. To each bin, I associate a point with coordinate defined with the median "ordinate" and "abscissa". Then, the red dashed fiducial line is derived by interpolating these points.

4. For each star, the distance from the fiducial line along the reddening direction (Δ "abscissa") is calculated. The subsample of stars used is located in a region of the CMD where the angular separation between the evolutionary sequence and the direction of the reddening vector is maximum. In this portion of the CMD, indeed, the impact that the random magnitude errors has on the observed colour spread is minimum when compared with the effect of differential reddening. The "ordinate" vs. Δ"abscissa" diagram is represented in *panel (c)*. The Δ"abscissa" value is taken as the value of the differential reddening that affects each sample star.

5. To estimate the differential reddening effect on each and all of the cluster stars, the median of the Δ"abscissa" scatter of the 30 closest spatial neighbour stars is considered, as portrayed in **Fig. 2.8**. The differential reddening contribution is subtracted to each star magnitude in order to correct them for this effect.

6. Finally, the procedure is repeated iteratively, starting from the differential-reddening corrected CMD in the previous iteration, until the differential reddening correction derived in two subsequent iterations converge. In the case, the procedure converged after four iterations.

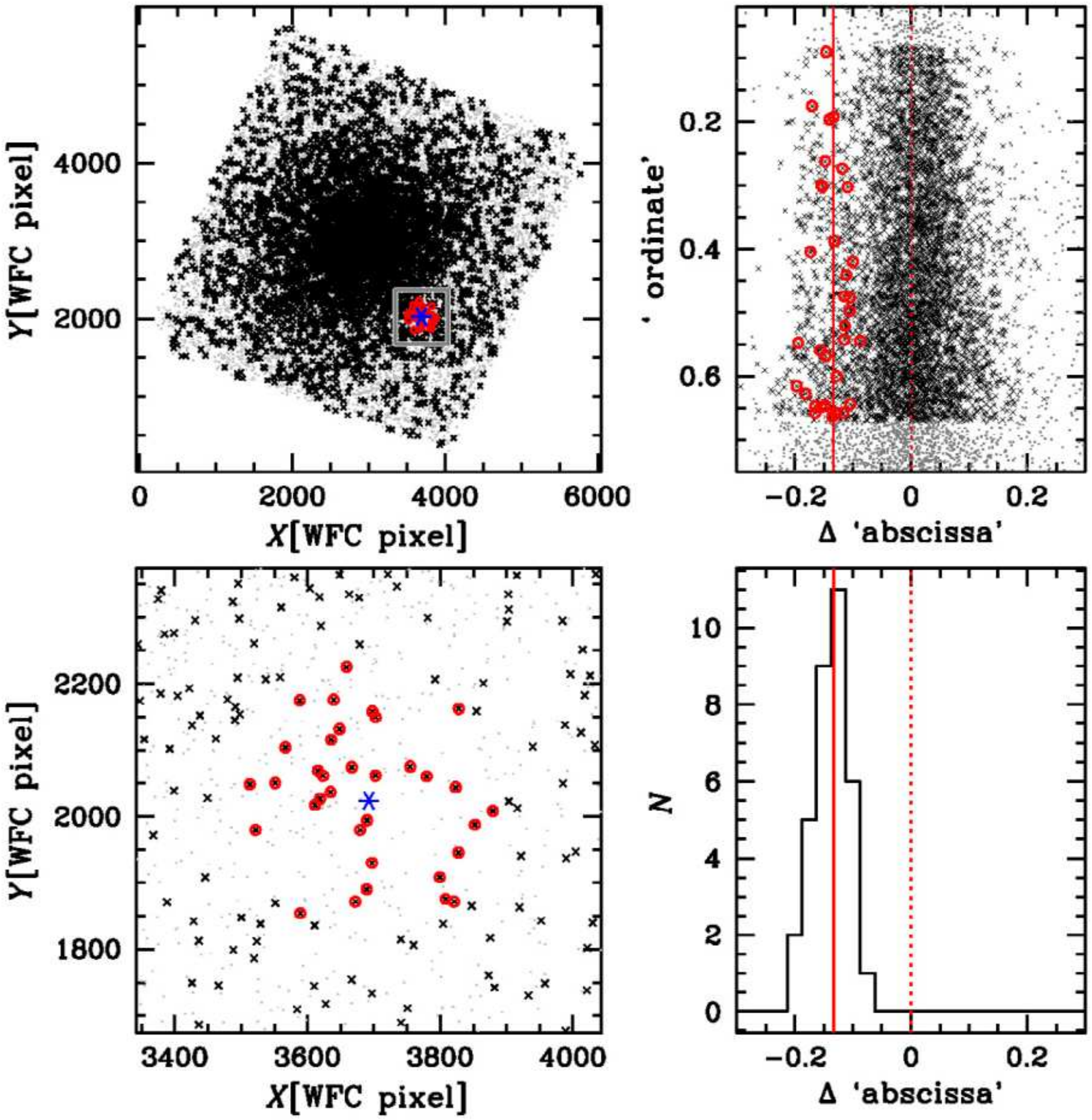

Figure 2.8: *Left panels: (Top)* A blue asterisk represents the target star, while red circles highlight the closest reference stars, indicated with black crosses, in the full ACS/WFC FoV, and *(Bottom)* zoomed in FoV centered on the target star. *Top right panel*: "ordinate" vs. Δ "abscissa" for all the stars in the FoV. The median "abscissa" of the neighbours is indicated by the continuous red vertical line. *Bottom right panel*: histogram of the Δ "abscissa" distribution of the neighbour stars. Taken from Milone et al., 2012b.

By comparing star-to-star variation in magnitudes of the original and the corrected CMDs it is possible to estimate local mean reddening variations $\Delta E(B\text{-}V)$ and derive a reddening map.

Fig. 2.9 shows the local deviations from the mean reddening $E(B\text{-}V)$. Local variations are calculated taking the median $\delta E(B\text{-}V)$ for corrected stars inside 10×10 pix^2 bins, in the case where no corrected stars are positioned inside a certain bin, that bin is assigned a value of zero differential reddening.

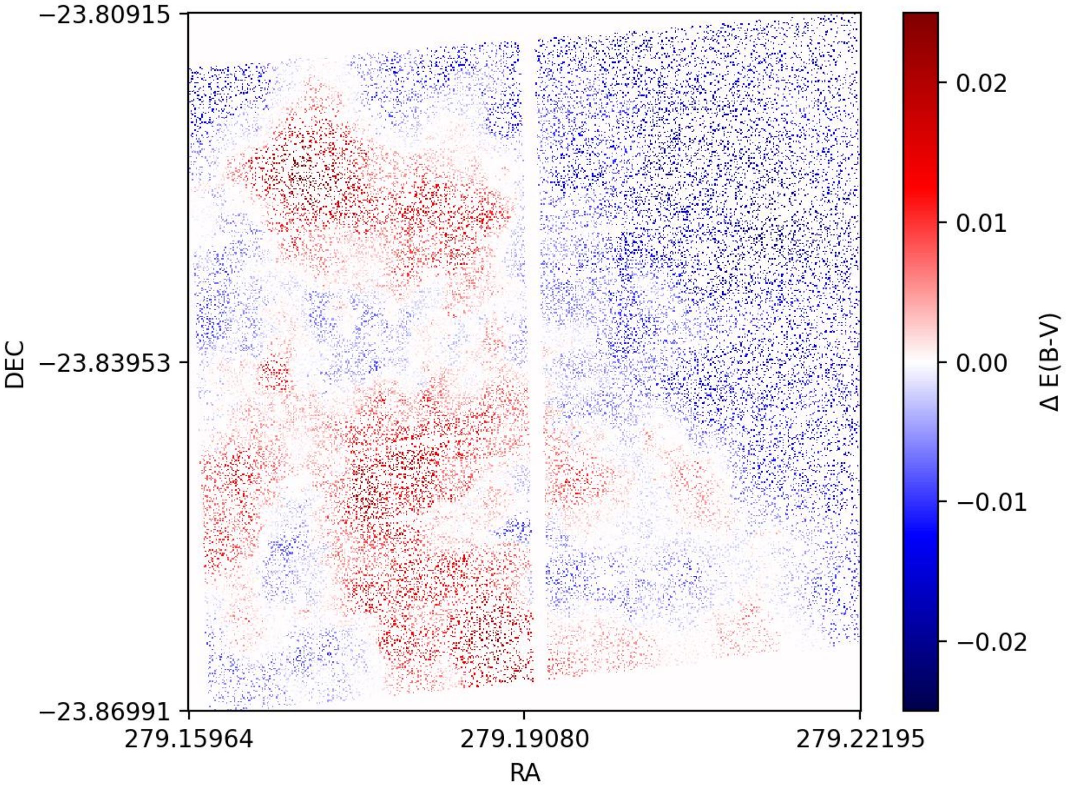

Figure 2.9: Reddening map of M22, local deviations from the mean reddening are seen across the FoV. The full FoV of the observations is divided in bins of 10×10 pix^2 (comprising 0.5×0.5 $arcsec^2$ according to HST ACS/WFC plate scale) where the median $\Delta E(B\text{-}V)$ from all corrected stars in each bin is taken as value. Bins where no corrected star falls are left with zero-value reddening.

The results obtained for differential reddening corrections are in agreement with previous similar studies (see **Table 2.2**) as Legnardi et al., 2023, Monaco et al., 2004[9], Piotto et al., 1999, and Richter et al., 1999, which report a variety of results, defined as:

- $\Delta E(B-V)$: total range of reddening variations
- $\Delta E(B-V)_{,max}$: maximum absolute value for a reddening variation in the sample
- $\sigma_{\Delta E(B-V)}$: standard deviation of reddening variations, as proxy for the intrinsic spread, and whose changes from color to color follow the reddening laws (Anthony-Twarog et al., 1995, Dean et al., 1978) as:
  $\sigma_{\Delta E(V-I)} = 1.34\ \sigma_{\Delta E(B-V)}$ (Monaco et al., 2004)
- ΔA_{F814W} can be obtained with the relation **Eq. 2.8**, discussed in at the beginning of this section.

	Present work	**Legnardi et al., 2023**	**Monaco et al., 2004**	**Piotto et al., 1999**	**Richter et al., 1999**
$\Delta E(B-V)$	0.051	-	0.06	-	0.07
$\Delta E(B-V)_{,max}$	0.029	-	-	-	-
$\sigma_{\Delta E(B-V)}$	0.010	-	-	-	-
$\sigma_{\Delta E(V-I)}$	0.013	-	0.03	0.05	-
$\Delta A_{F814W,max}$	0.053	0.047	-	-	-
$\sigma_{\Delta A_{F814W}}$	0.018	0.12	-	-	-

Table 2.2: Differential reddening results

---

[9] Values considered as upper limits to the amount of differential reddening needed to explain the RGB width, assuming zero metallicity spread.

The calibrated and corrected for differential reddening CMD is shown in **Fig. 2.10**. All the evolutionary sequences along the CMD are narrowed down to better defined distributions (specially above m_{F814W} ~17), with respect to a non-corrected CMD.

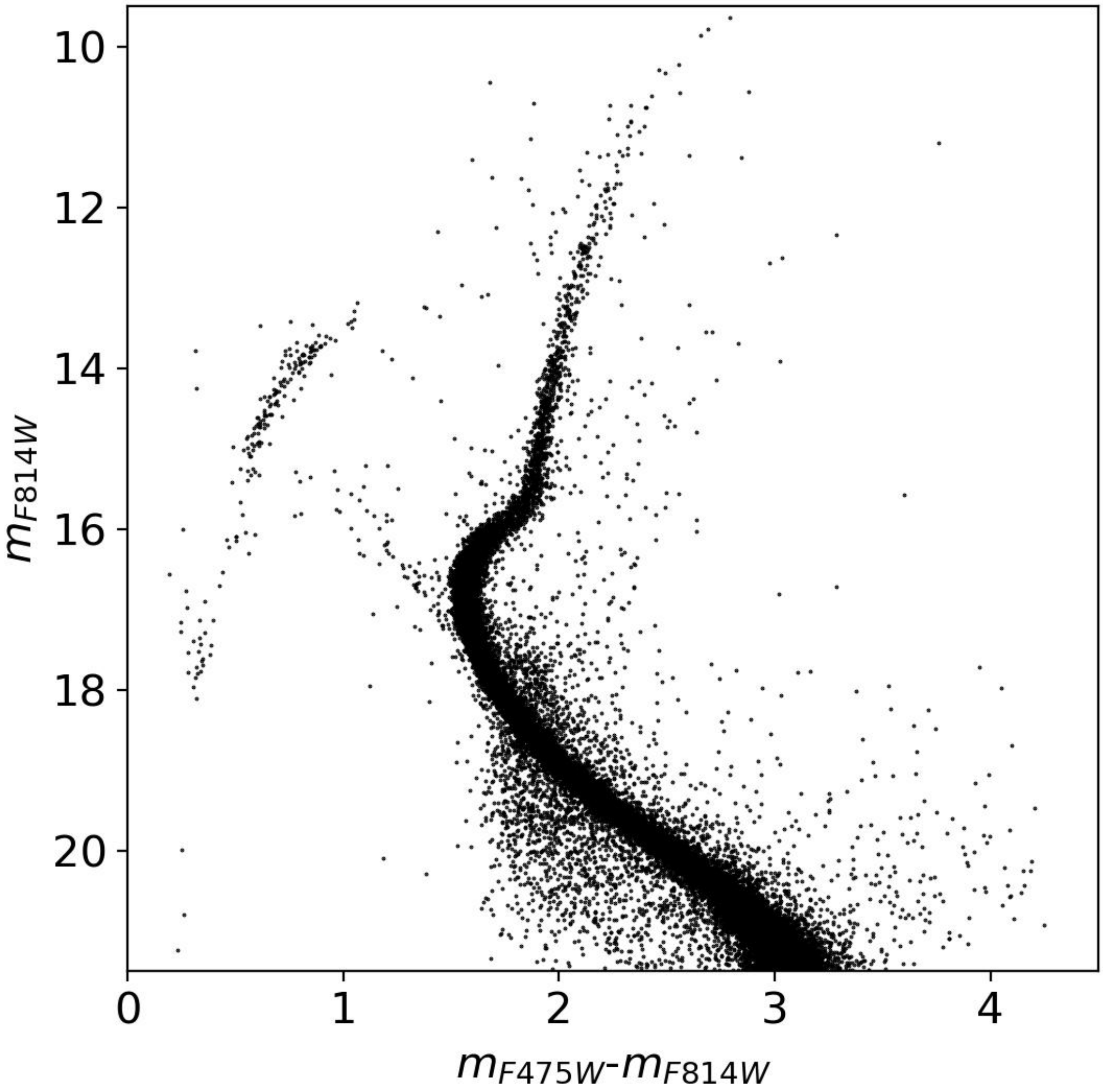

Figure 2.10: m_{F814W} vs. (m_{F814W}-m_{F475W}) CMD for M22 corrected for differential reddening.

3

Data Analysis and Results

In the previous chapter, state-of-the art photometry was derived from the most recent HST observations of M22, taken with the F475W and F814W filters; in this chapter, this catalog is exploited to estimate fundamental cluster parameters such as age, mean reddening, distance modulus, and luminosity distance in **Sec. 3.1**. The following **Sec. 3.2** is dedicated to the investigation of the chemically-different populations harbored by M22 making use of all the datasets described in **Sec. 2.2**.

3.1 ISOCHRONE FITTING

For the purpose of estimating fundamental cluster parameters, a group of 7 isochrone models is considered from the DSEP[10] (Dotter et al., 2007), which require the following input parameters:

- *[Fe/H]*. Small differences in the iron abundances (0.15 dex) among M22 stars are well documented in literature (Marino et al., 2009b, Marino et al., 2011, McKenzie et al., 2022). For the present fit, the value of **-1.82** was used as adopted for metal-poor RGB stars by Marino et al., 2011.

- *[α/Fe]*. Marino et al., 2009b and Marino et al., 2011 find $[\alpha/Fe] = 0.36$ and

---

[10] Dartmouth Stellar Evolution Program data accessed on April 2024 at http://stellar.dartmouth.edu/models/index.html.
Alternatively, ischrone models can also be taken from the PARSEC library via a query on the Stellar Evolution server (STEV) from Osservatorio Astronomico di Padova (OAPd) at http://stev.oapd.inaf.it/

0.33, respectively. The closest available value in the DSEP models is **0.4**, which is the one adopted in this work.

- *Helium mass fraction (Y)*. Due to the small He variation among the different populations of M22 (Milone et al., 2018), a primordial value of **0.245** is assumed.

- *Age*. To derive the age of the GC, a grid of seven isochrones with ages **12.0, 12.5, 13.0, 13.2, 13.4, 13.6,** and **13.8** Gyr with fixed [$^{Fe}/_{H}$], [$^{\alpha}/_{Fe}$], and Y is considered.

In order to perform isochrone fitting, it is necessary to transform the model magnitudes from the theoretical to the observational plane by applying the following formula:

$$m(x) = M(x) + 5log(d) - 5 + A_x \tag{3.1}$$

where *M(x)* is the absolute magnitude of the theoretical model, *d* the luminosity distance (in pc), and A_X the interstellar extinction in the X band (explained thoroughly in **Sec. 2.6**).

With the assumed values for k_X ($k_{F438W} = 4.1818$ and $k_{F814W} = 1.8420$) a mean color excess can be found through the best fit of the reddening vector defined in **Eq. 2.5**.

In **Fig. 3.1**, the m_{F814W} vs. (m_{F475W} -m_{F814W}) CMD with the grid of considered isochrones and the reddeining vector is illustrated, which displays the direction and the amount of the reddening effect in the CMD plane. **Fig. 3.2** shows a zoom-in around the MSTO region, which is the part of the CMD most sensitive to age variation. The isochrones that, by eye, best-fit the observed CMD distribution range from 13.2 to 13.8 Gyr. The detailed results of the fit, including the final *E(B-V)*, distance modulus, and distance in kpc are presented in **Table 3.1**, along with literature results, showing that the values here derived qualitatively align with past studies.

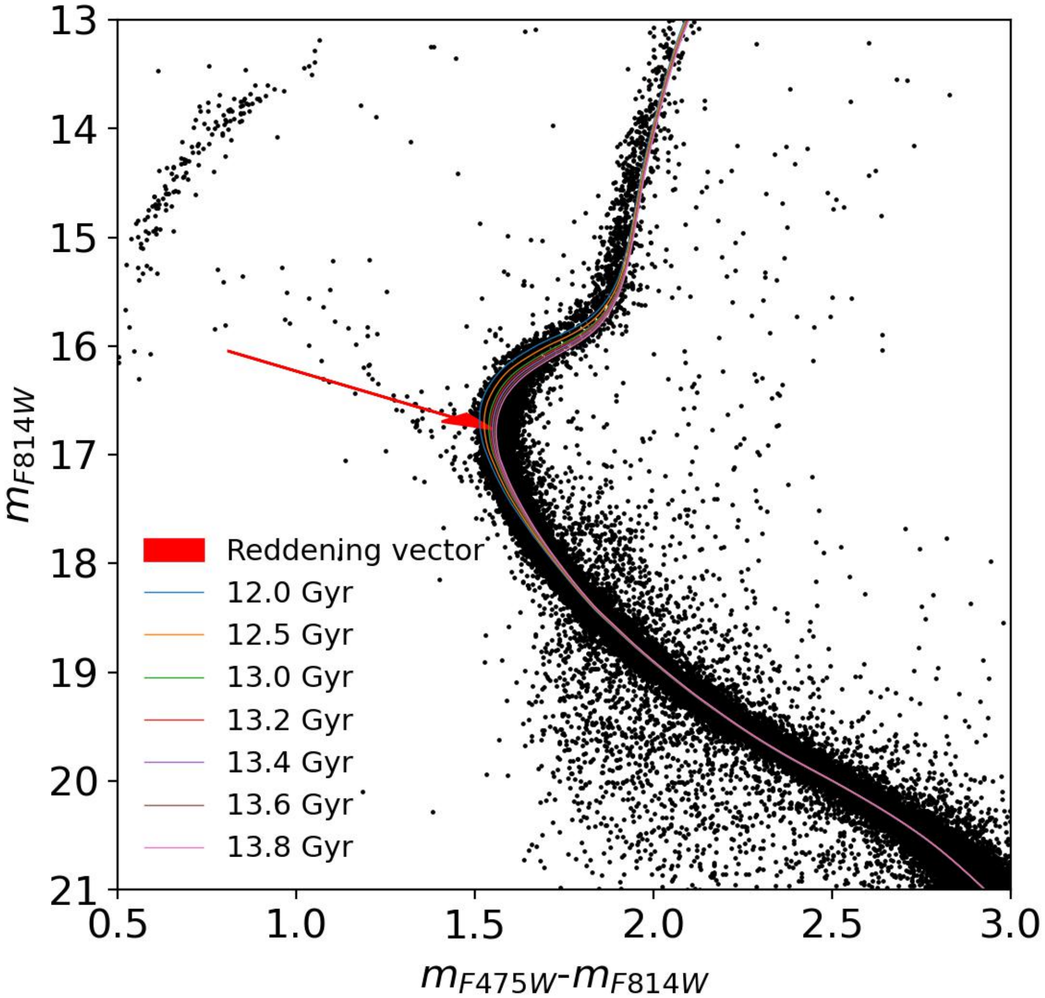

Figure 3.1: Isochrone fitting process. The seven lines, color-coded as indicated in the plot, indicate the isochrone grid used. The red arrow indicates the effect of a reddening variation of *E(B-V)* = 0.39.

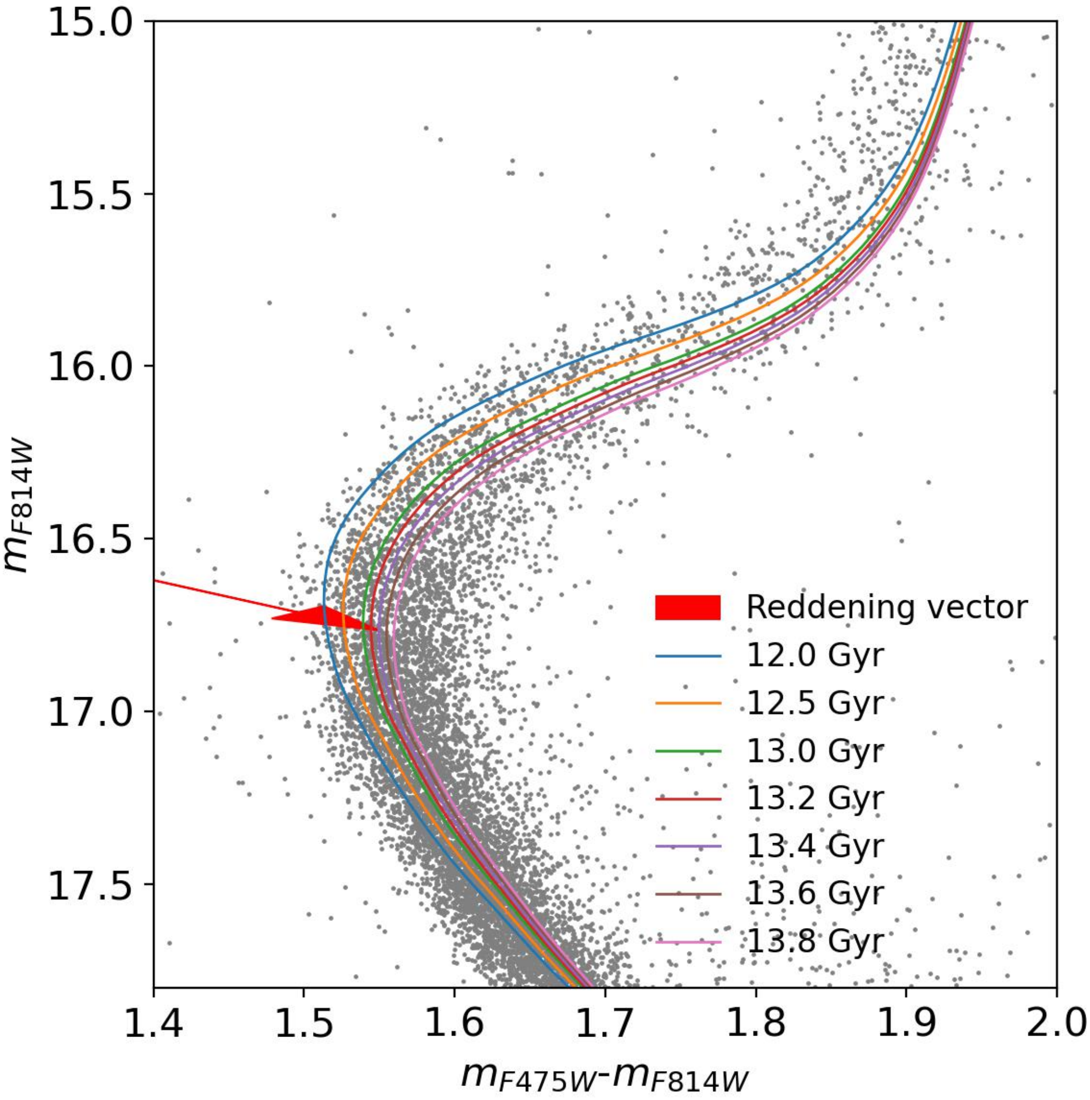

Figure 3.2: Isochrone fitting zoom in.

	Present work	**Marino et al.** (2011, 2012)	**Piotto et al.** (1999)	**Baumgardt & Hilker** (2018)	**Legnardi** (2023)	**Monaco et al.** (2004)
Age [*Gyr*]	13.2-13.8	13.5	10.0-14.0	-	-	-
Mean reddening *E(B-V)*	0.39	0.34	0.31-0.37	-	0.34	0.38
Distance modulus [*mag*]	13.3	13.6	13.7	-	-	13.7
Luminosity distance [*kpc*]	3.31	~3.2	-	3.1	-	~3.2

Table 3.1: Isochrone fit results

3.2 MULTIPLE POPULATIONS IN M22

This section is dedicated to the investigation of the chemically-different populations harbored by M22. To do so, several multi-band photometric catalogs were collected from the literature in order to separate the different groups of stars along the whole GC area, from its center to the outskirts. **Sec. 3.2.1** illustrates the procedure to disentangle multiple populations by using HST data, while **Sec. 3.2.2** explains how to identify the distinct stellar groups by using ground-based observations.

3.2.1 HST OBSERVATIONS

To study the innermost ~2 arcmin for M22, Dataset 3 introduced in **Section 2.2.3** is exploited, in particular observations in the F275W, F336W, F438W, and F814W filters. Indeed, combining UV and optical observations is crucial to disentangle populations with differences in C, N, and O since the F275W, F336W, and F438W passbands are sensitive to the absorption bands of the OH, NH, CN, and CH molecules.

To reveal the distinct stellar groups in M22, the ChM diagram, a pseudo two-color diagram able to maximize the separation between the multiple populations, is the appropriate tool. In order to build this diagram, the procedure introduced by Milone et al., 2015a, 2017 was followed, which exploits the (m_{F275W} - m_{F814W}) and the $C_{F275W,F336W,F438W}$ filter combinations, where the index :

$$C_{F275W,F336W,F438W} = (m_{F275W} - m_{F336W}) - (m_{F336W} - m_{F438W}), \tag{3.2}$$

has the advantage of separating multiple sequences with different N abundances along the whole CMD (Milone et al., 2013). Along with the ChM derived from these two filter combinations, a second ChM based on the (m_{F336W} - m_{F814W}) color instead of the (m_{F275W} - m_{F814W}) is also derived. Indeed, this color is more effective in separating the bulk of canonical and anomalous stars, as represented in **Fig. 3.3**, where the two RGB sequences are well separated. Therefore, beyond the classical ChM introduced by Milone and collaborators, a second ChM is put forward, which puts more emphasis on the separation between canonical and anomalous stars. The procedure (valid for both ChMs) involves the following steps:

1. **Selection of RGB target stars**. Exploiting the m_{F814W} vs (m_{F336W} - m_{F814W}) CMD, the MSTO and RGB are identified by eye and manually selected via a polygon filter. These stars are colored in black in **Fig. 3.3**.

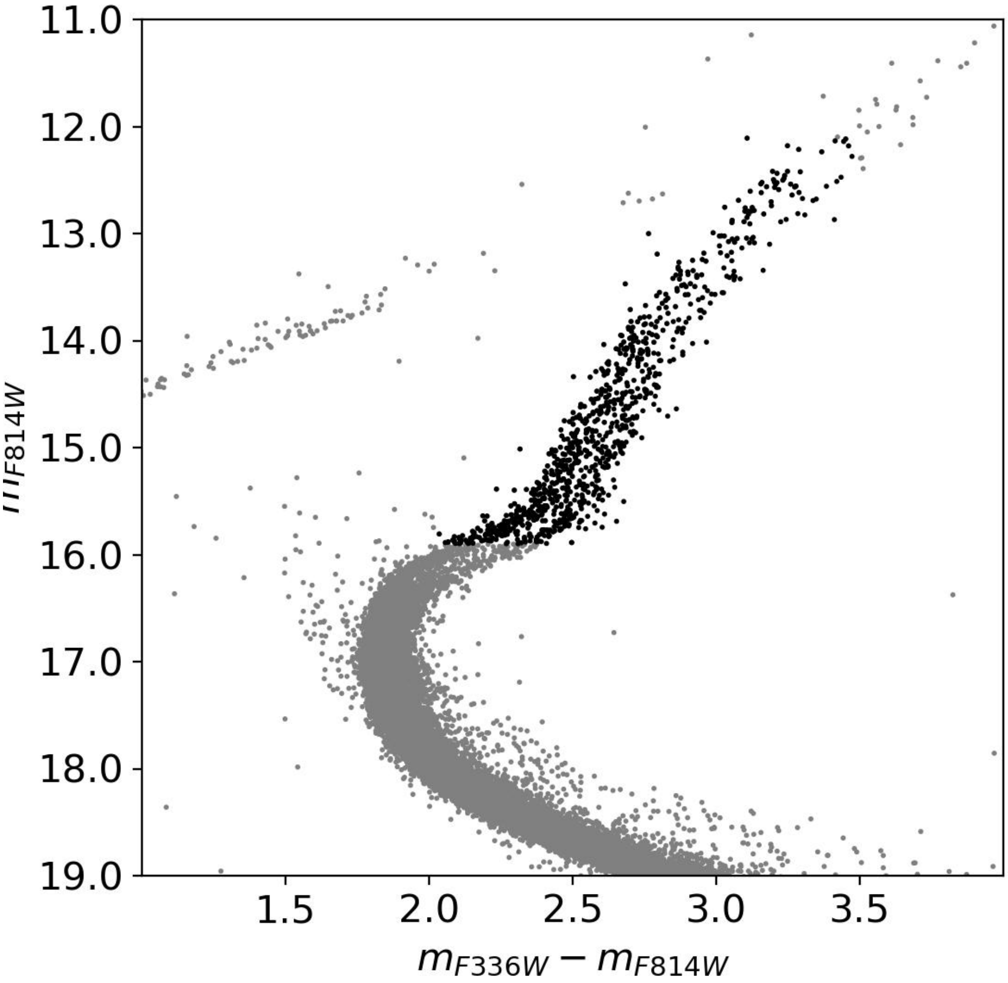

Figure 3.3: Selected RGB stars are colored in black.

2. **Derivation of the fiducial lines**. F814W magnitude intervals of size δm are considered to define magnitude bins over a grid of points separated by $s = \delta m/3$ magnitude intervals. For each bin, the 4th and the 96th percentile are measured on both (m_{F336W} - m_{F814W}) and $C_{F275W,F336W,F438W}$ filter combinations and associated to the average m_{F814W}. Blue and red fiducial lines represented in **Fig. 3.4** are defined by smoothening the points distribution by means of boxcar averaging, where each point is replaced by the average of the three adjacent points. The observed RGB width, $W^{obs}_{F336W,F814W}$, is defined as the difference between the m_{F336W}-m_{F814W} index of the red and blue fiducial lines, calculated 2.0 *F814W* magnitudes above the MSTO (see **Fig. 3.4**, where it is traced as a turquoise line). The

analogous quantity $W^{obs}_{CF275W,F336W,F438W}$ for the $C_{F275W,F336W,F438W}$ index is also derived.

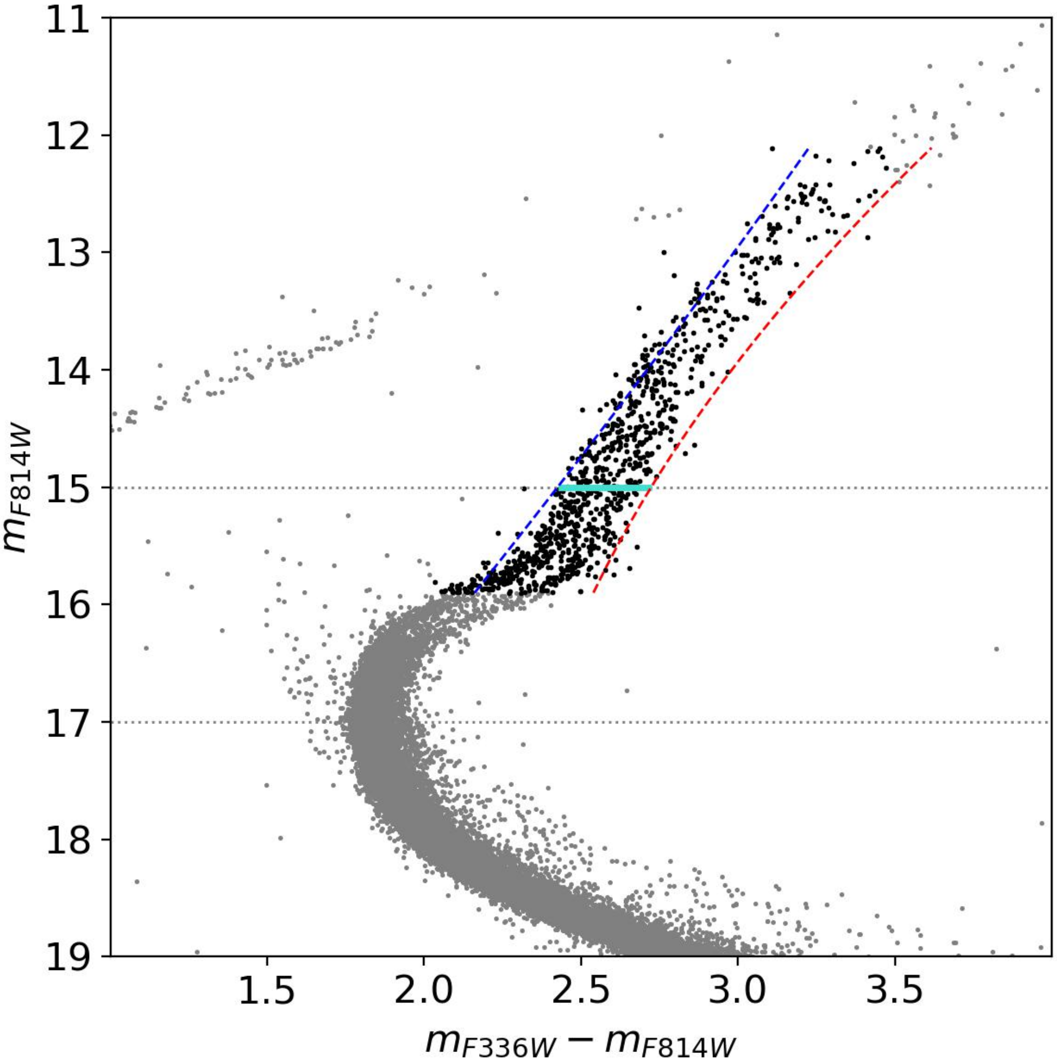

Figure 3.4: Blue and red fiducial lines mark boundaries of the selected RGB region. The observed width is traced with a turquoise line.

3. **ChM coordinates.** Finally, to derive the coordinates in the ChM reference frame, the following transformations are applied:

$$\Delta_{F336W,F814W} = W_{F336W,F814W} \frac{X - X_{Rf}}{X_{Rf} - X_{Bf}} \tag{3.3}$$

$$\Delta_{CF275W,F336W,F438W} = W_{CF275W,F336W,F438W} \frac{Y_{Rf} - Y}{Y_{Rf} - Y_{Bf}}, \tag{3.4}$$

where $X = (m_{F336W} - m_{F814W})$ and $Y = C_{F275W,F336W,F438W}$, with *Rf*, *Bf* being the corresponding red and blue fiducial lines.

In this way, Δ measures the colour distance to the red fiducial line, as Δ=*0* corresponds to stars lying on such line. **Fig. 3.5** depicts the result of applying this procedure to HST (m_{F275W} - m_{F814W}), (m_{F336W} - m_{F814W}) and $C_{F275W,F336W,F438W}$ (pseudo-) colours on the *left*, *central*, and *right panel*, respectively.

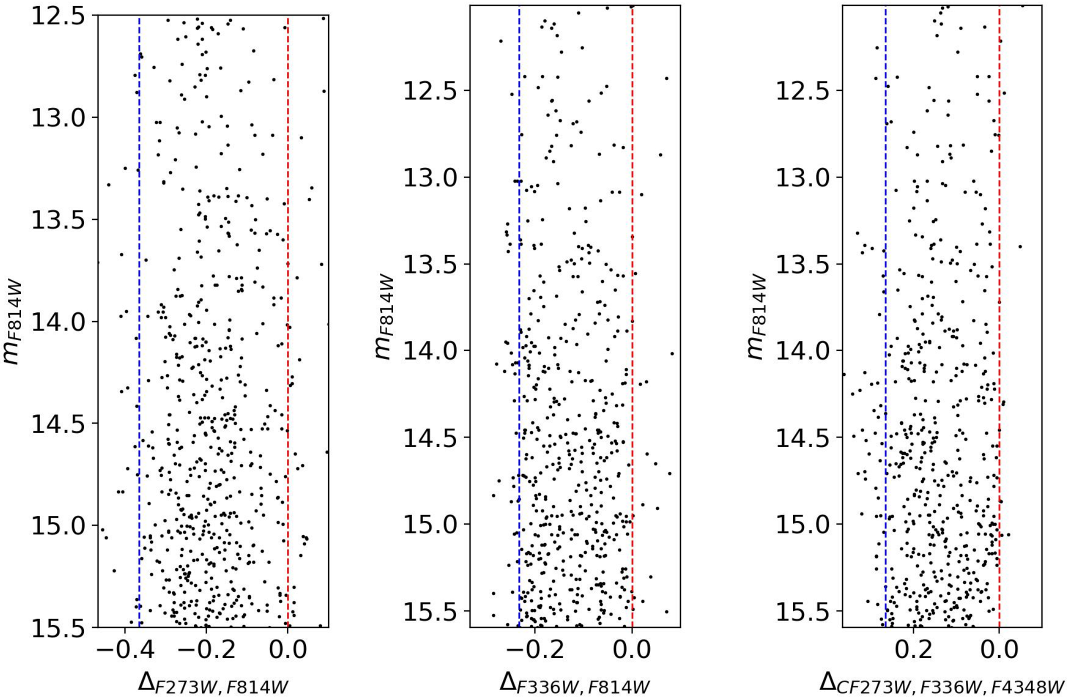

Figure 3.5: $\Delta_{F275W,F814W}$, $\Delta_{F336W,F814W}$, and $\Delta_{CF275W,F336W,F438W}$ ChM coordinates plotted against m_{F814W} magnitude in the *Left*, *Central* and *Right panel* respectively.

The final $\Delta_{\mathrm{F275W,F814W}}$ vs. $\Delta_{\mathrm{CF275W,F336W,F438W}}$ and $\Delta_{\mathrm{F336W,F814W}}$ vs. $\Delta_{\mathrm{CF275W,F336W,F438W}}$ ChMs are represented in **Fig. 3.6** in the *upper* and *lower panel*, respectively.

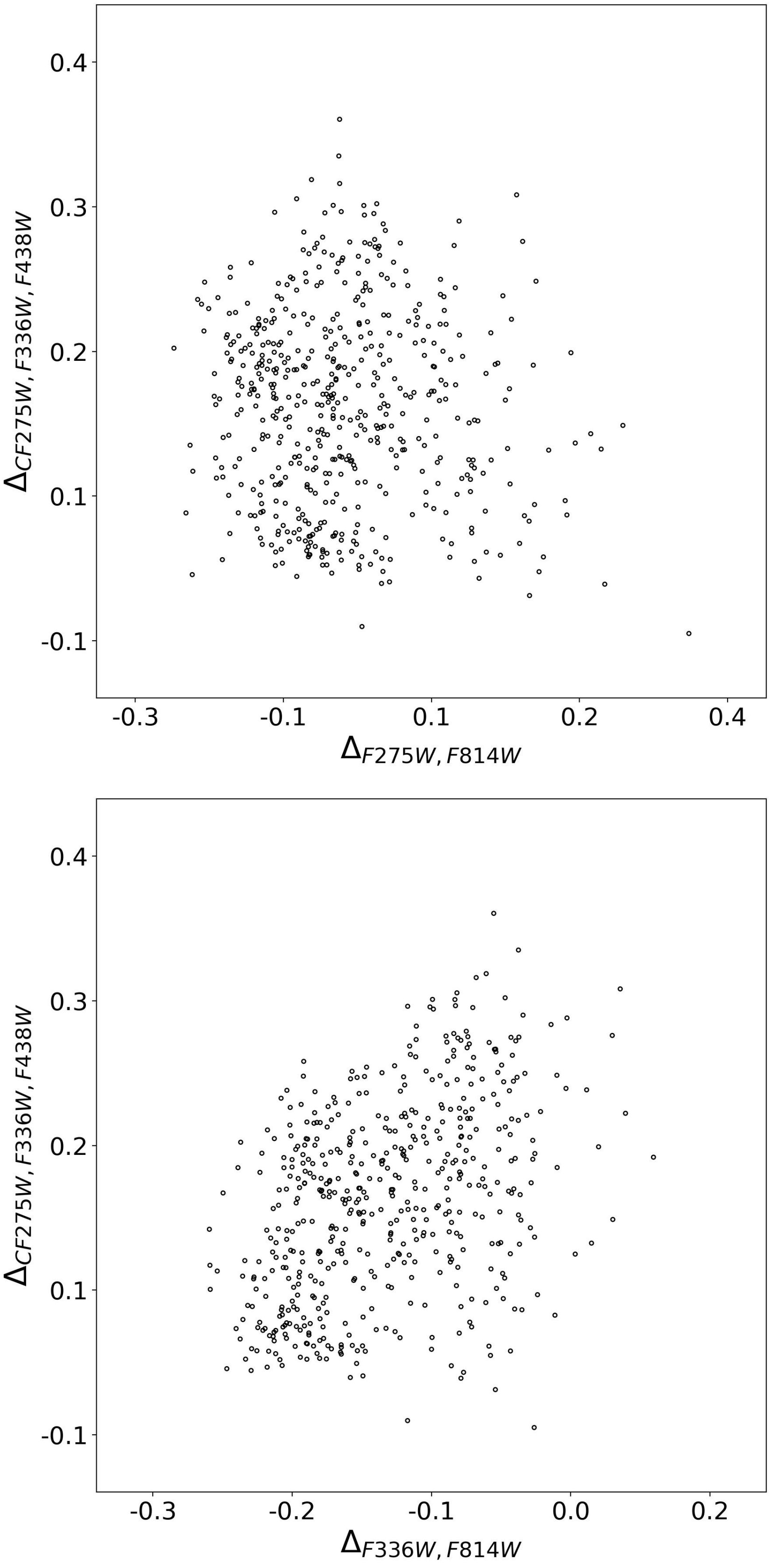

Figure 3.6: *Top panel*: $\Delta_{CF275W,F336W,F438W}$ vs $\Delta_{F275W,F814W}$ ChM, result is comparable to that of Marino et al., 2012. *Bottom panel*: $\Delta_{CF275W,F336W,F438W}$ vs $\Delta_{F336W,F814W}$ ChM.

Being M22 a Type II GC (see discussion in **Sec. 1.3**), it is characterized by an additional group of stars, beyond the typical 1G and 2G patterns, dubbed *anomalous* population. Its presence produces an additional redder RGB sequence. The (m_{F336W} - m_{F814W}) color maximises the separation between the two RGBs, likely due to nitrogen differences, to which the F336W band is particularly sensitive (Yong et al., 2014, Milone et al., 2017, Dondoglio et al., 2023), as can be clearly seen in **Fig. 3.7**; furthermore the wide spread of stars can be complementary inferred, when comparing to previous studies of similar clusters (Marino et al., 2008), to be due to the sodium - oxygen anticorrelation, where 1G stars are oxygen rich and sodium poor, hence with primordial chemical composition, while 2G stars are enhanced in sodium and depleted in oxygen. For this reason, anomalous stars can be selected by eye in the m_{F814W} vs (m_{F336W} - m_{F814W}) CMD, represented in red in **Fig. 3.7**.

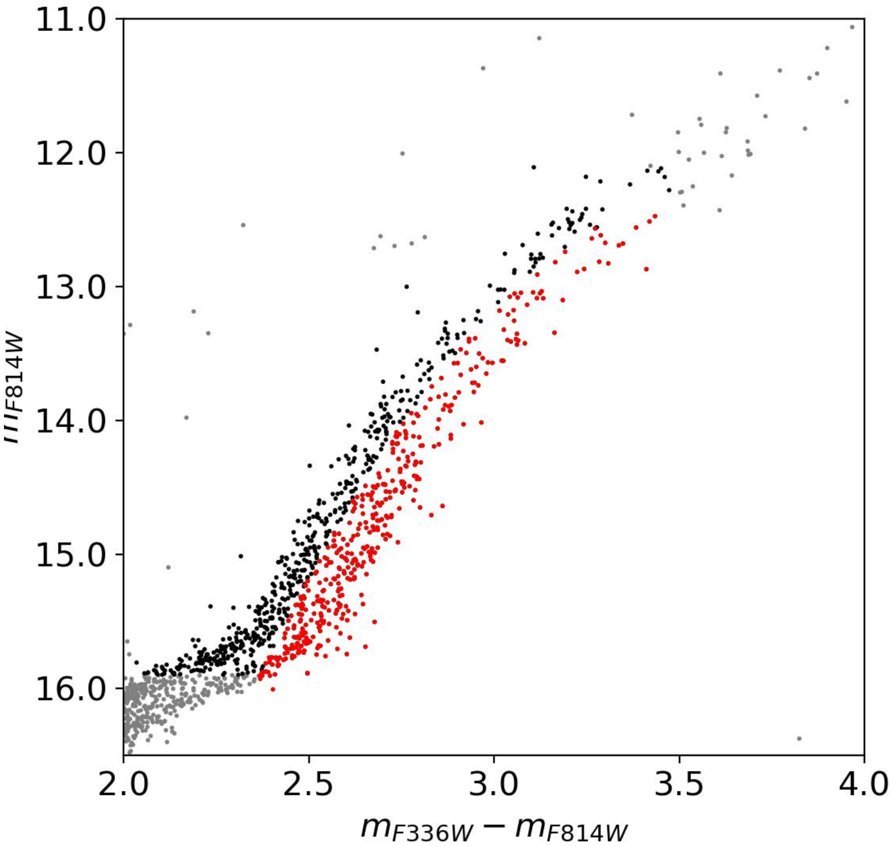

Figure 3.7: The anomalous population of stars is selected by eye and presented in red color.

Having identified the anomalous population, it is possible to plot an updated version of the HST CMDs with the anomalous population color coded in red, as seen in **Figs. 3.8, 3.9**, and **3.10**, where, as in 3.4, two grey horizontal dotted lines are placed at the magnitude level of the MSTO and at the bin closest to 2.0 *F814W* mags above it. The blue and red lines mark the fiducial lines acting as boundaries of the RGB, while the turquoise segment represents the observed RGB width. On the *right panels*, the verticalized representation of the RGB CMDs showing the blue and red fiducial lines. Black and red dots represent metal-poor and metal-rich sets of stars respectively.

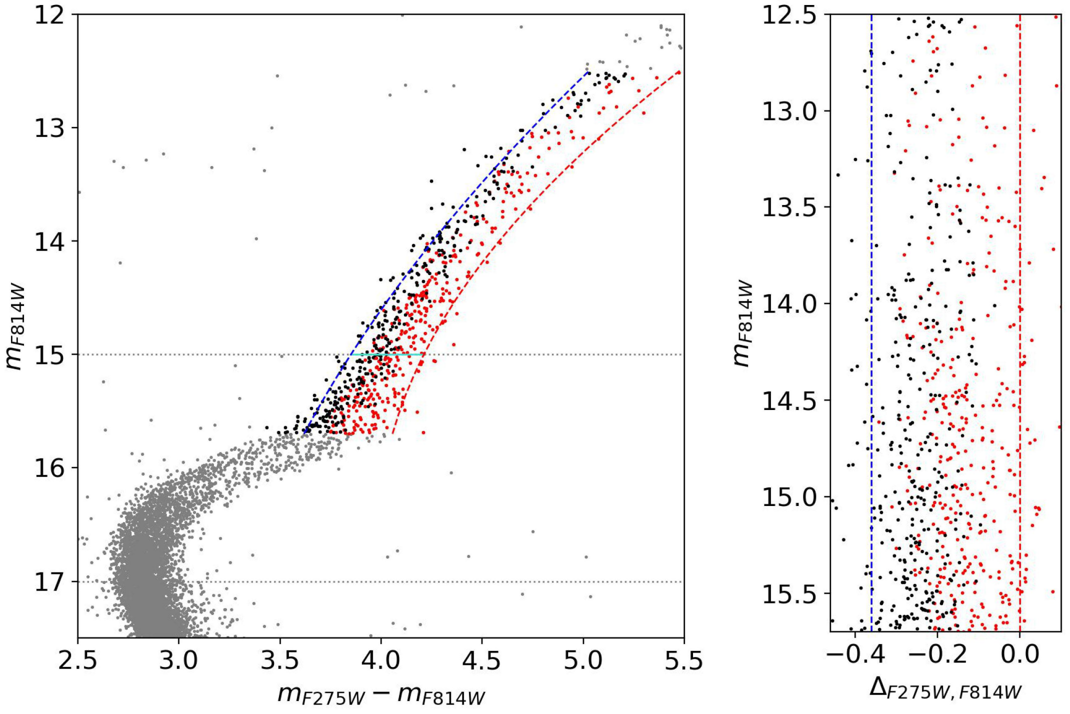

Figure 3.8: m_{F814W} vs (m_{F275W} - m_{F814W}) CMD with color verticalization.

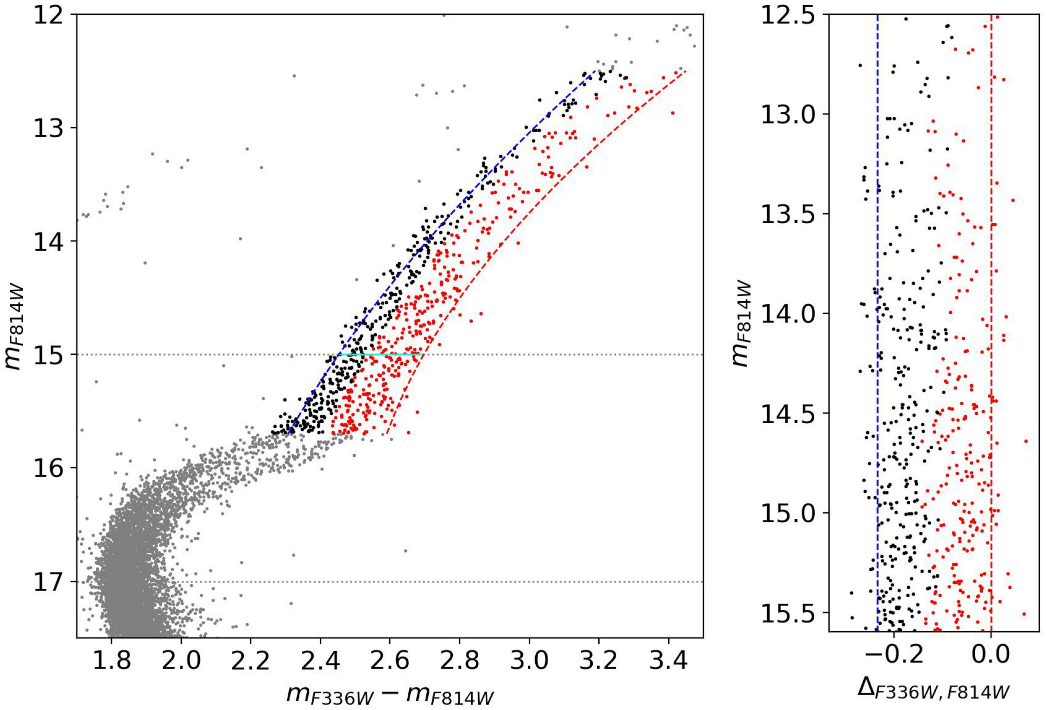

Figure 3.9: m_{F814W} vs (m_{F336W} - m_{F814W}) CMD with color verticalization.

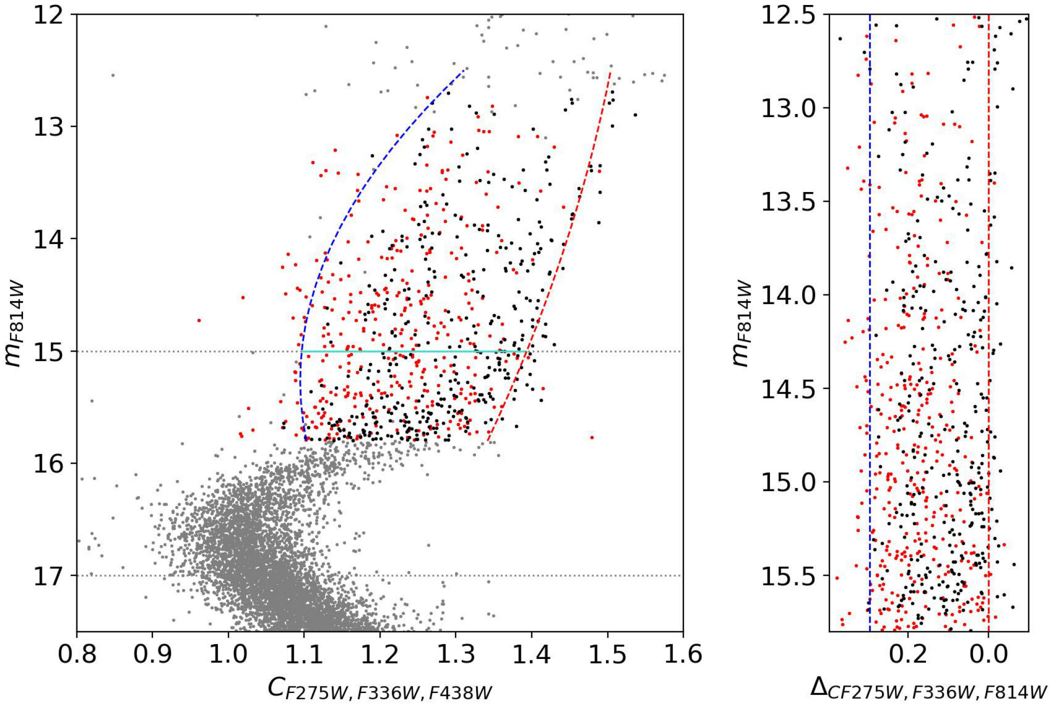

Figure 3.10: m_{F814W} vs $C_{F275W,F336W,F438W}$ CMD with color verticalization.

The same ChMs represented in **Fig. 3.6** are shown in **Fig. 3.11** this time, the metal-rich, anomalous stars are color coded in red. In both diagrams, this stars have redder pseudo-colors along the x-axis, as also proven by the Kernel Density Estimation (KDE) plotted on top of each ChM. Notably, the two distribution have a much more clear-cut separation in the $\Delta_{\mathrm{F336W,F814W}}$ pseudo-color than in the $\Delta_{F275W,F814W}$. Intriguingly, the KDE along the y-axis illustrates that both populations span a comparable interval in $\Delta_{CF275W,F336W,F438W}$, thus suggesting that not only the canonical stars are made by chemically-different subpopulations (i.e., the 1G and 2G stars that form two separate peaks), but also anomalous stars exhibit internal chemical inhomogeneities.

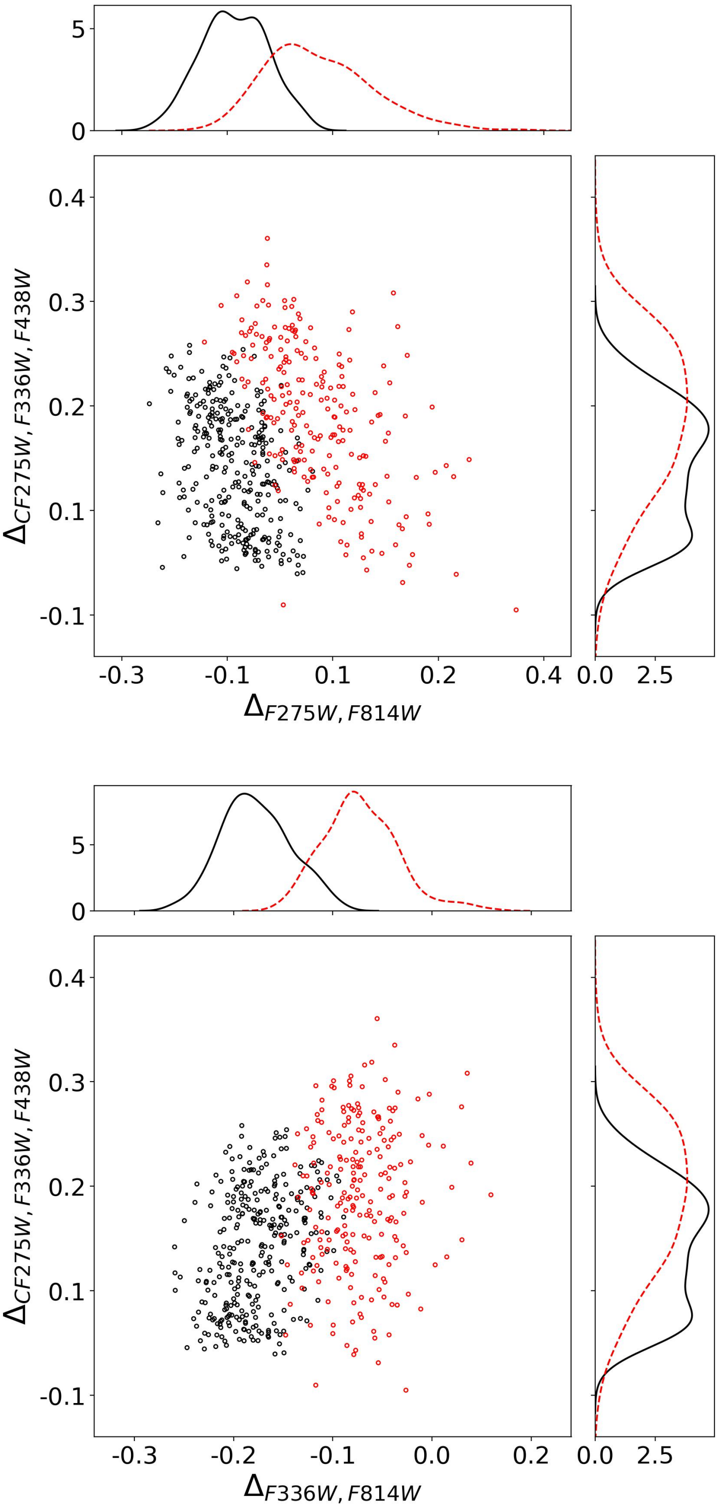

Figure 3.11: Top panel: $\Delta_{CF275W,F336W,F438W}$ vs $\Delta_{F275W,F814W}$ ChM. Bottom panel: $\Delta_{CF275W,F336W,F438W}$ vs $\Delta_{F336W,F814W}$ ChM. Black and red points represent canonical and anomalous stars, respectively. The kernel density distribution of canonical (black continuous) and anomalous (red dashed) along both axis are represented on top and side of each ChM diagram.

3.2.2 Ground-based observations

Ground based photometry and spectroscopy, **GB** for short, (see **Secs. 2.2.4** and **2.2.5** for details on these datasets), allow to map a much larger area of the cluster, since these types of observations commonly enclose the full GC, albeit with a lower resolution. Joining **Datasets 3**, **4** and **5**, it is possible to infer some chemical characteristics of the populations identified in the GC.

Also, GB allows to map a radial characterisation of the identified populations across the GC.

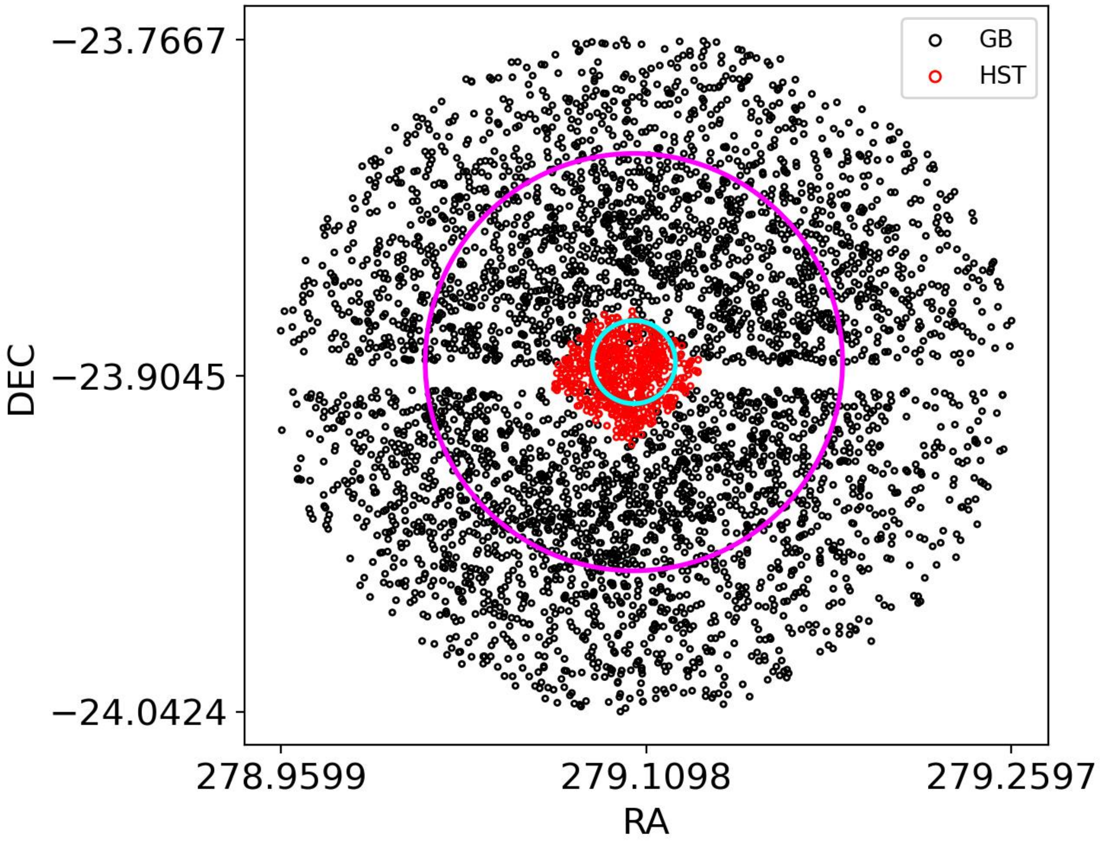

Figure 3.12: FoV for *HST* and *GB* observations. *HST* and *GB* observations are complementary to characterise the GC on its full radial extension. Cyan and magenta circles represent the median radius from GC center of stars in *HST* and *GB* observtions, respectively.

Now, the procedure explained in **Sec. 3.2.1** is applied to GB observations; in summary, after identifying the anomalous population with the U vs (U - V) CMD (**Fig. 3.13**), verticalization of U - B, U - I and $C_{U,B,I}$ pseudo-colors is performed in order to produce the ChMs for these observations, shown in **Fig.**

3.14, which reveals stars distributed along two main, distinct groups, namely *canonical* and *anomalous* populations (colored in black and red dots respectively), this information was foreshadowed by the clear SGB and RGB splits seen in **3.13**. The KDE plots in **3.14** show a similar behavior than what seen from **Figs. 3.11**, thus proving that anomalous stars are still present in the outskirts of M22 and that the spreads on the ChM y-axis of the two populations are comparable.

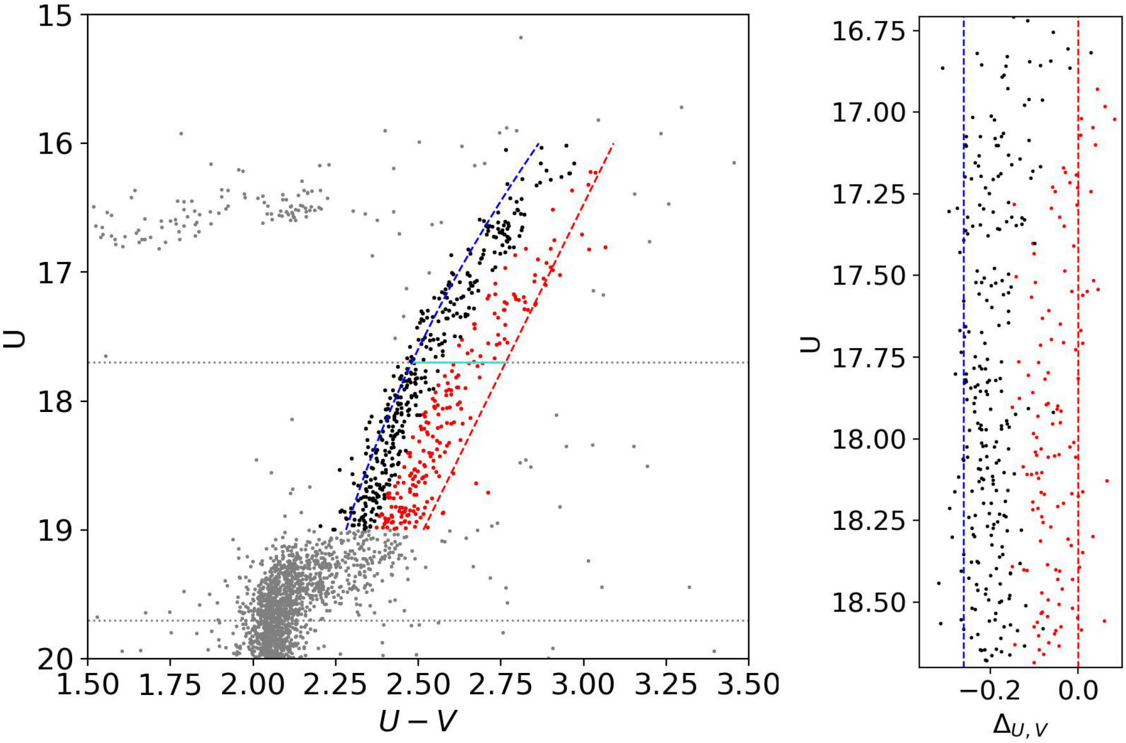

Figure 3.13: U vs (U - V) CMD, ideal for anomalous population identification.

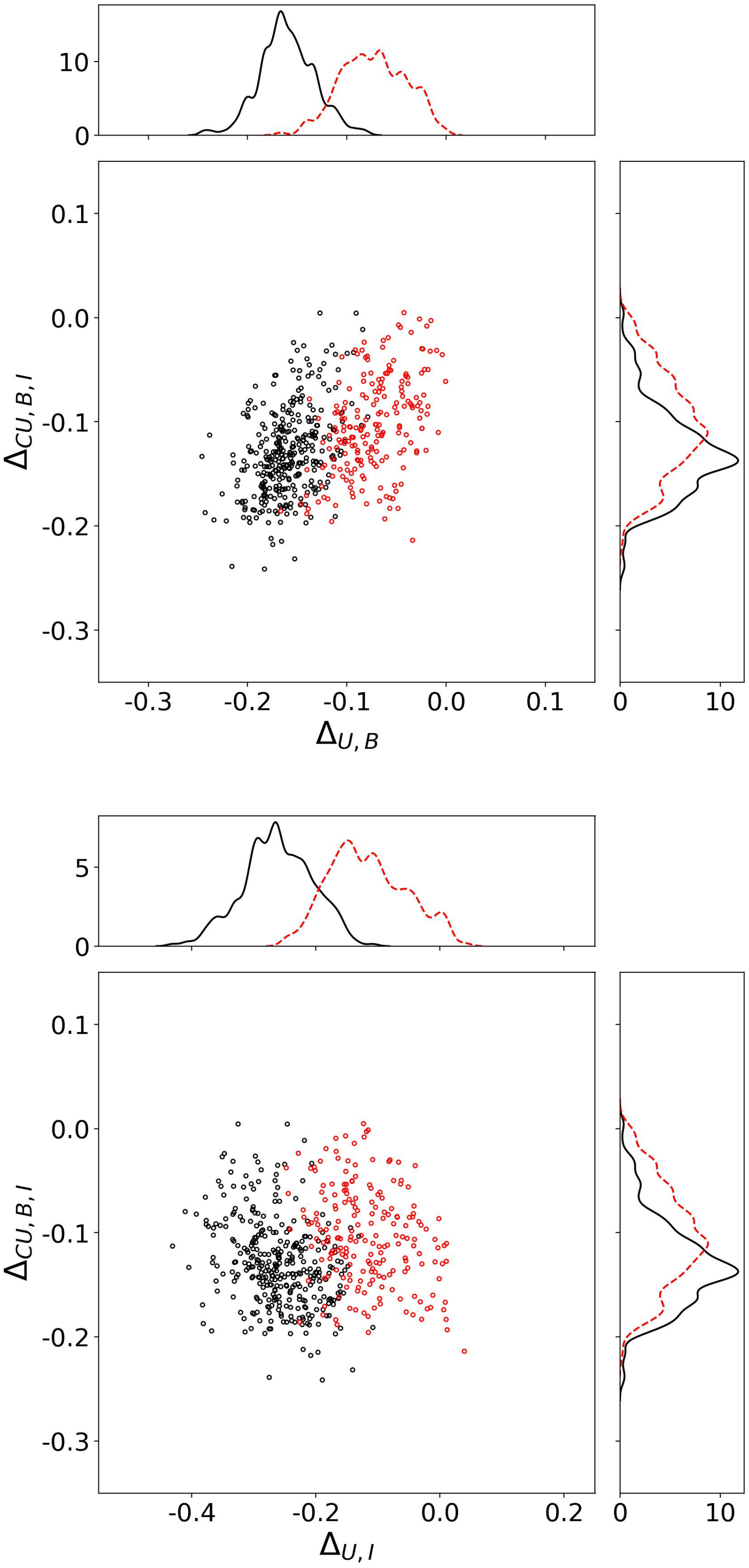

Figure 3.14: *Top panel*: $\Delta_{CU,B,I}$ vs $\Delta_{U,B}$ ChM. *Bottom panel*: $\Delta_{CU,B,I}$ vs $\Delta_{U,I}$ ChM.

3.2.3 Population identification

With the ChMs produced in **Sec. 3.2**, the different populations that can be disentangled in these photometric diagrams are now identified. The 1G and 2G stars in the ChM made with HST filters are grouped in two separated blobs (see **Sec. 1.1.1**) centered at the ChM coordinates ($\Delta_{F336W,F814W}$,$\Delta_{CF275W,F336W,F438W}$) ~(-0.2,-0.15) and ~(0.5,0.18), respectively, as seen in **Fig. 3.15**. To define a sample of 1G and 2G stars, two ellipses that encapsulate the respective blobs in the ChM are built. To do that, the procedure presented in Dondoglio et al., 2023 used for the anomalous GC NGC1851 is followed.

1. Select by hand the bona fide members of each population.
2. Measure the median ChM coordinates of each population, which define the center of the respective ellipses.
3. Find the line that crosses the center and minimizes the orthogonal dispersion of the population. This defines the major axis direction.
4. Fix the length of the semi-major and -minor axis as 2.5 times the dispersion of stars along the directions parallel and orthogonal to the major axis direction, respectively.

The green and magenta ellipses in **Fig. 3.15** define the location of 1G and 2G stars, respectively, in the ChM.

Since the anomalous stars do not form separated distribution in the ChM, the procedure outlined by Dondoglio et al., 2023 to define anomalous sub-populations cannot be applied. However, it is still remarkable how this population is clearly not formed by chemically homogeous stars, as proven by the similar y-axis range covered on the ChM compared to the canonical stars. In order to study anomalous sub-populations, the lot of them is tentatively divided into two populations -AI and AII- defined as the stars below and above the 50_{th} percentile of the y-axis anomalous stars distribution. This border is indicated as a horizontal red line in **Fig. 3.15**. This same procedure is repeated using the $\Delta_{CU,B,I}$ vs $\Delta_{U,B}$ ChM, as shown in **Fig. 3.16**. Sub-populations *1G, 2G, AI*, and *AII* are color coded in green, magenta, cyan, and yellow, respectively, while the total number of stars belonging to each are referred to as P_{1G}, P_{2G}, P_{AI}, P_{AII}.

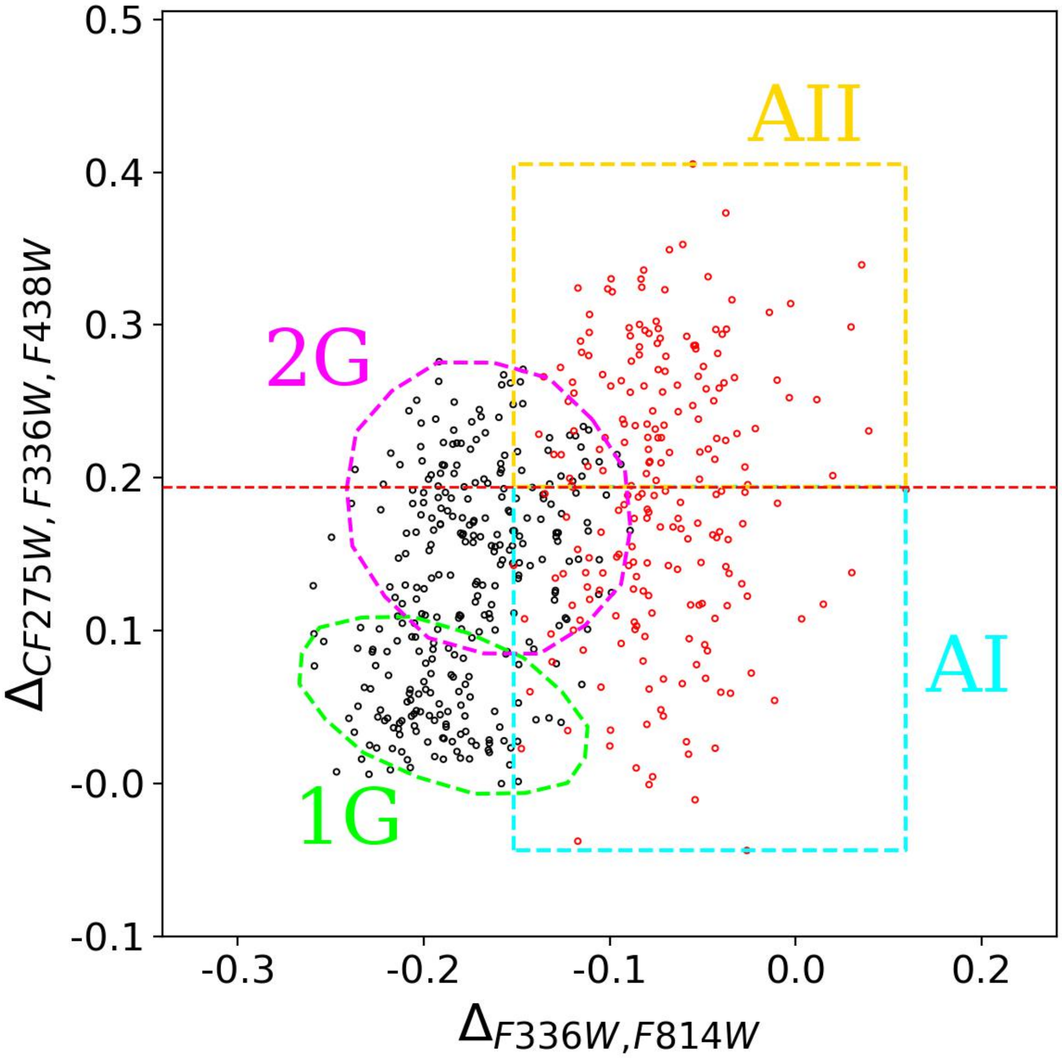

Figure 3.15: $\Delta_{CF275W,F336W,F438W}$ vs $\Delta_{F336W,F814W}$ population selection. Canonical sub-populations can be selected with the ellipse method, while the anomalous sub-populations are selected by dividing above and below the 50_{th} percentile along Y -axis, depicted as yellow- and cyan-bordered regions.

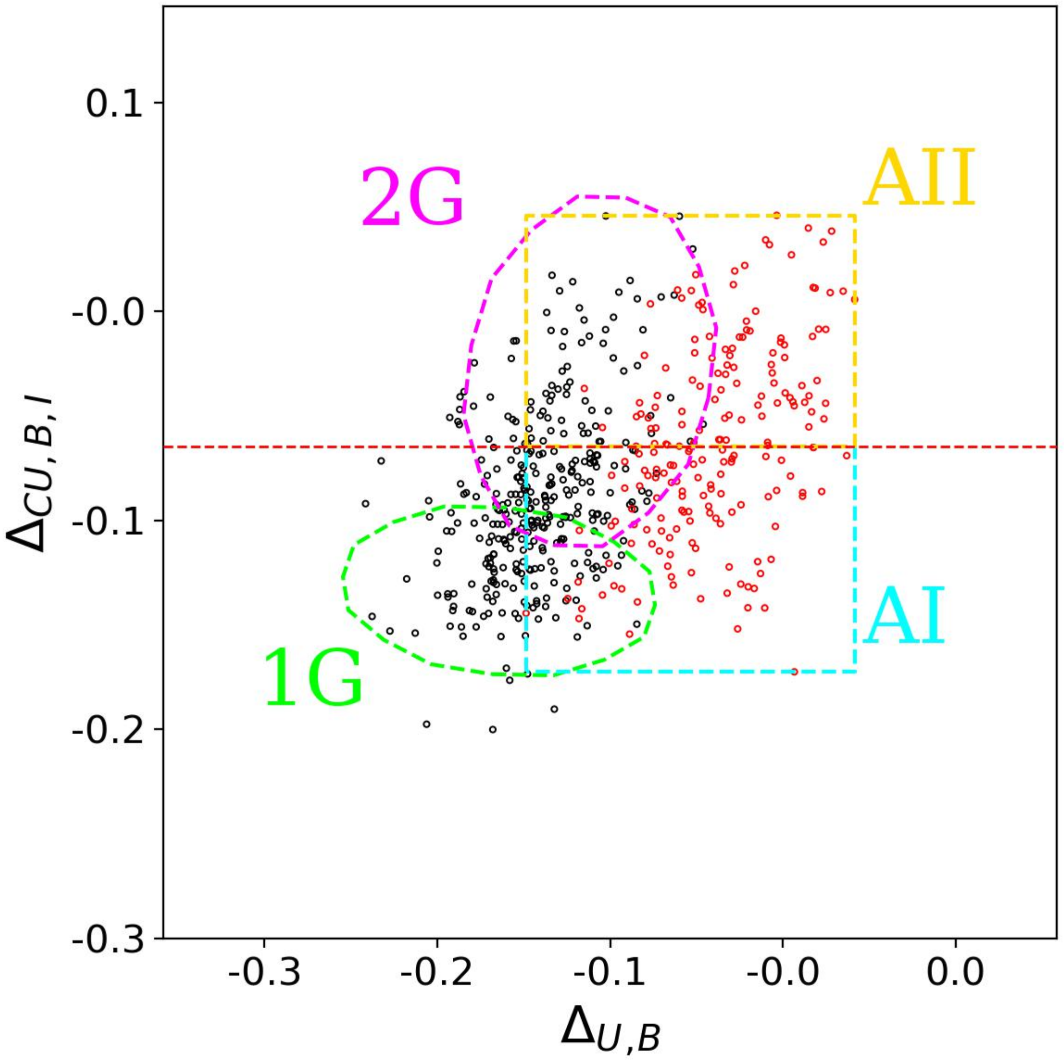

Figure 3.16: $\Delta_{CU,B,I}$ vs $\Delta_{U,B}$ population selection.

When the ellipse method is applied, it is possible to identify P_{1G} and P_{2G}, while the division on the 50^{th} percentile allows to separate P_{AI} from P_{AII}. Finally, on counting the stars in each of the polygons (ellipses or rectangles), the hierarchy adopted is P_A first, meaning if a star is already identified as *anomalous*, then it is not taken into account if it is inside any of the ellipses; then, if a star falls into the P_1 ellipse, then it is not taken into consideration for P_2 in the particular case that it falls into both ellipses.

3.2.4 Population fractions and radial distributions

With the separation provided in **Sec. 3.2.3**, it is now possible to calculate the fraction of the distinct populations harbored by M22[11].

Each population's absolute fraction can be estimated as:

$$f_x = \frac{P_x}{P_{1G} + P_{2G} + P_{AI} + P_{AII}} \tag{3.5}$$

therefore, the total canonical population is defined as $P_C = P_{1G} + P_{2G}$ and similarly, $P_A = P_{AI} + P_{AII}$ is the total anomalous population, found in the red-RGB sequence on the appropriate CMD. This implies that the total population in the cluster is $P_{TOTAL} = P_A + P_C$.

Relative population fractions of canonical 1G, 2G, and anomalous AI, AII populations are derived by dividing their total number of stars by P_C and P_A respectively. The derived fractions, along with their uncertainties, are reported in **Table 3.2**.

	Absolute fraction	$\pm\sigma$	**Relative fraction**	$\pm\sigma$
Metal-poor	0.601	0.015	1.000	0.000
Metal-rich	0.399	0.016	1.000	0.000
1G	0.252	0.015	0.427	0.025
2G	0.339	0.016	0.573	0.028
AI	0.211	0.014	0.516	0.033
AII	0.198	0.013	0.484	0.032

Table 3.2: Overall absolute and relative population fractions. 1G and 2G, and AI and AII relative fractions refer to those with respect to the metal-poor and metal-rich populations respectively.

In order to map the behaviour of the fractions of 1G, 2G, and anomalous population stars, both a Cumulative Distribution Function (CDF) plot and a radial distribution of the population fractions were computed. Two separate CDF plots were computed to have a more precise reference of the behaviour of stars, since HST and GB have different characteristics, the radial count of stars is not seamless across datasets. The plots are presented in **Fig. 3.17**. In the *upper panels*, the result for the HST dataset is shown, covering the innermost 110 arcsec, while the CDF from the GB dataset is represented in the *lower panels*, and

---

[11] While the population fraction here proposed certainly gives a hint of the real MSP composing the GC, another applicable method is that of a bi-gaussian decomposition (described in Dondoglio, 2020 and Dondoglio et al., 2023)

covers a much larger radial interval, about four times wider. The comparison between the bulk of canonical (metal-poor) and anomalous (metal-rich) stars in the *right panels* show a very small difference between the two distributions, so that no particular segregation is evident. On the other hand, the CDF of 1G and 2G stars show large differences in the 120-480 arcsec range, thus suggesting that 2G stars (that have larger values in this radial range) are more centrally concentrated than the 1G. Also AI and AII exhibit a similar behavior, consistent with the latter being more centrally concentrated than the former.

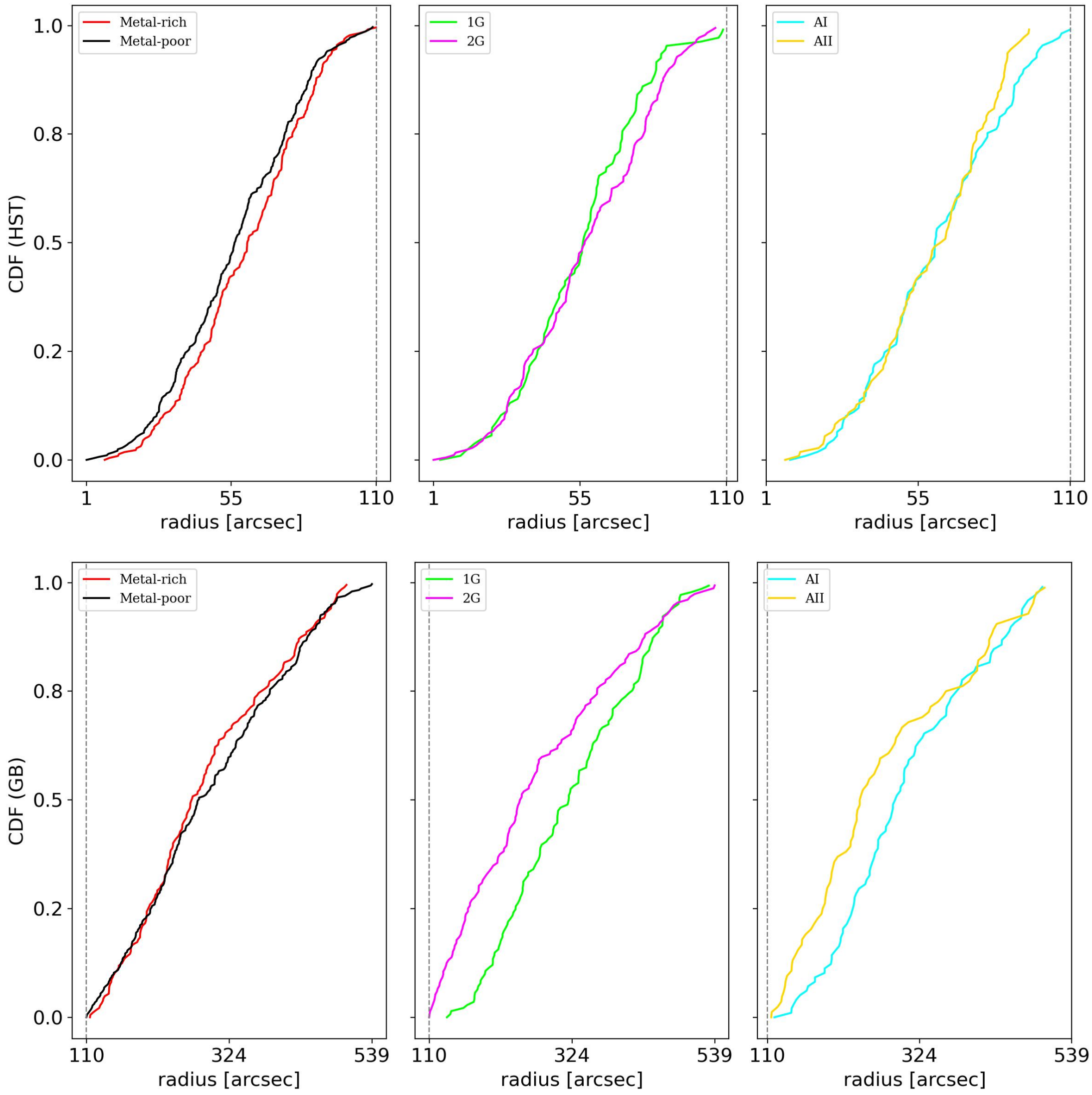

Figure 3.17: *Top panel*: Radial CDF for stars in HST FoV. *Bottom panel*: Radial CDF for stars in GB FoV. *Left column*: Metal-poor and metal rich CFD. *Central column*: Metal-poor 1G and 2G CFD. *Right column*: Metal-rich AI and AII CFD. A vertical grey dotted line is added as reference for the limit of HST FoV.

The radial distribution of the fraction of the different populations is then derived by repeating the procedure to compute their fractions at different radial bins. Given that GB photometry tends to be poor close to the GC center because of crowding, stars from GB observations that overlap with the HST FoV were discarded in this analysis. To avoid any possible bias due to different number of stars per bin, the full radial extension of the cluster is divided in bins of equal number of stars to obtain a step-wise mean value of the radius and population fraction, along with their associated errors.

The radial distribution of the bulk of canonical and anomalous stars is illustrated in **Fig. 3.18**, while the distributions of canonical and anomalous sub-populations are illustrated in **Fig 3.19** and **3.20**, respectively. On each plot, a vertical gray line indicates the FoV limit of HST observations, with data inside and outside this radial coordinate portrayed with circles and triangles respectively. The average trend of the fraction of anomalous stars exhibits a modest decrease moving outwards, thus suggesting that these stars are more centrally concentrated than the canonicals. On the other hand **Fig 3.19** and **3.20** clearly show that the fraction of 2G and AII stars decrease moving outwards. The radial distribution of the populations fractions are qualitatively in agreement with the CDF results, thus with a very small variation of the anomalous and canonical fractions (with a possible small decrease arising from the radial distribution), and with a difference in segregation within their sub-populations.

Moreover, a p-value test was performed to infer the probability that the observed radial behaviours are intrinsically flat, and that any deviation from a constant trend is the result of observational errors. To do that, for each distribution, 10,000 radial distributions were simulated by scattering the average fraction by the observational error and the corresponding χ^2 value was calculated. Then, the p-value was calculated by dividing the number of times that the simulated χ^2 was larger than the χ^2 of observed data. The derived p-values are 0.22, 0.08, and 0.18 for absolute metal-rich and -poor, relative metal-poor 1G and 2G, and relative metal-rich AI and AII populations respectively. The 1G and 2G distributions are the ones characterized by the smallest value, therefore with the highest probability of being intrinsically non-flat.

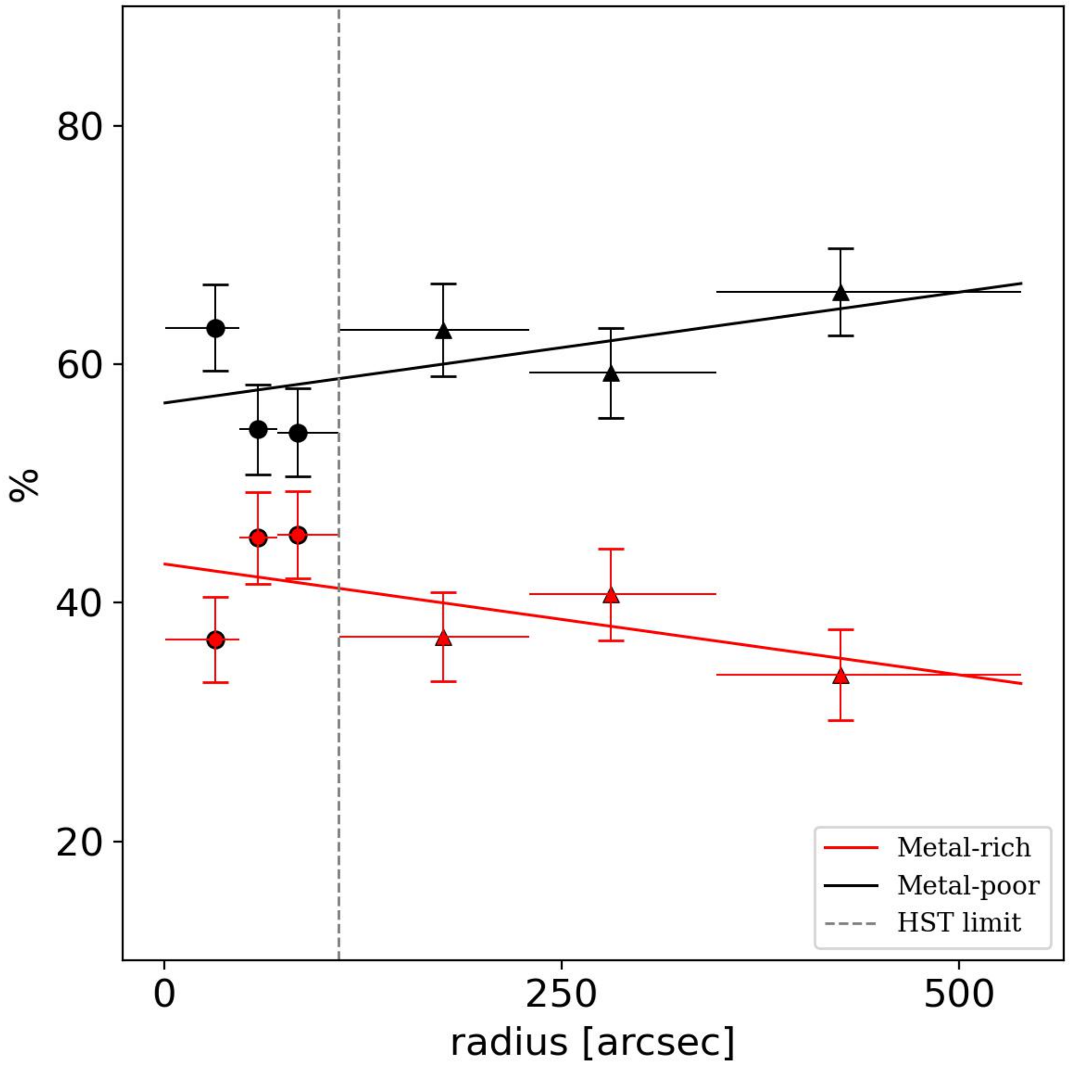

Figure 3.18: Radial distribution of population fractions for metal-poor and metal-rich populations. A vertical grey dotted line is added as reference for the limit of HST FoV. Circles represent datapoints from HST observations while triangles do so for GB observations.

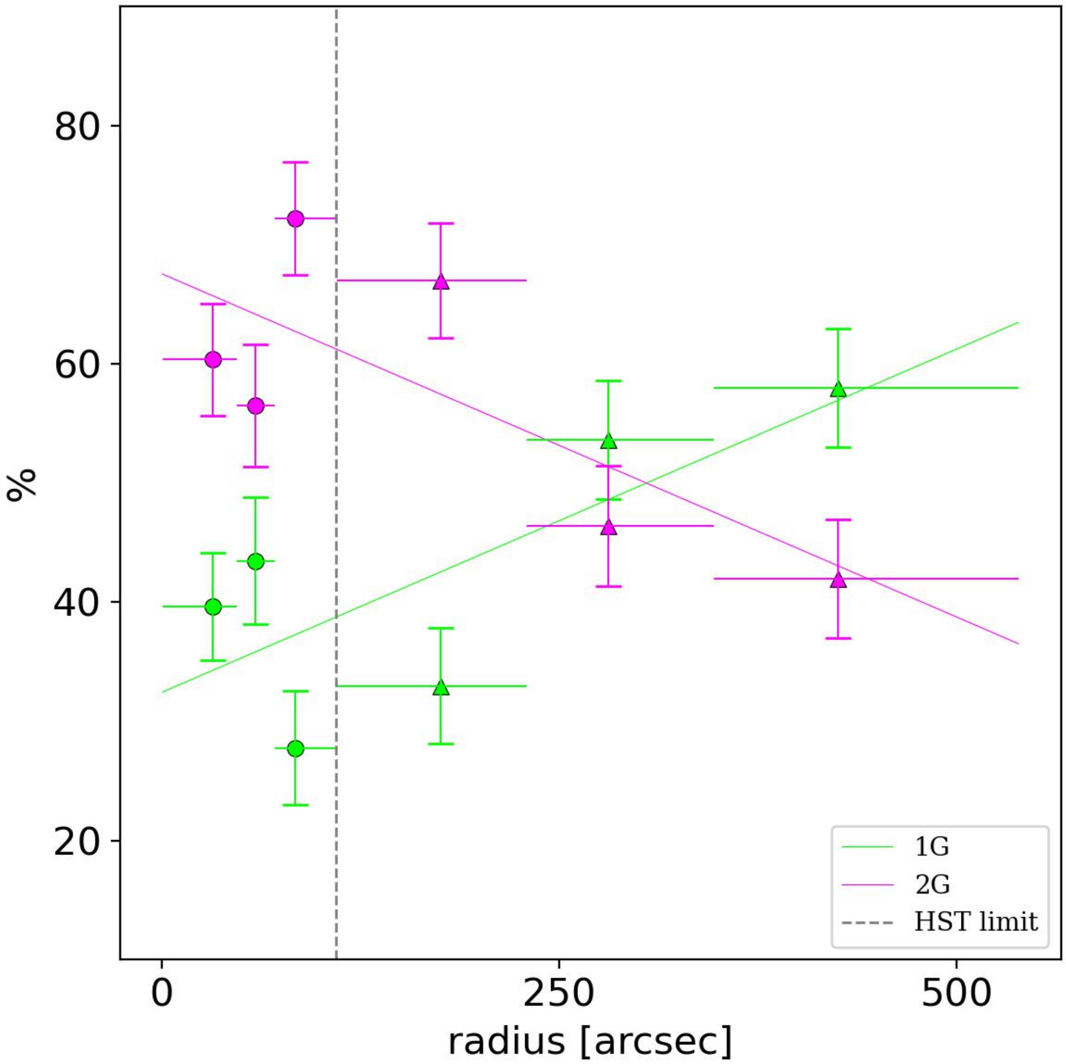

Figure 3.19: Radial distribution of metal-poor 1G and 2G fractions. A vertical grey dotted line is added as reference for the limit of HST FoV. Circles represent datapoints from HST observations while triangles do so for GB observations.

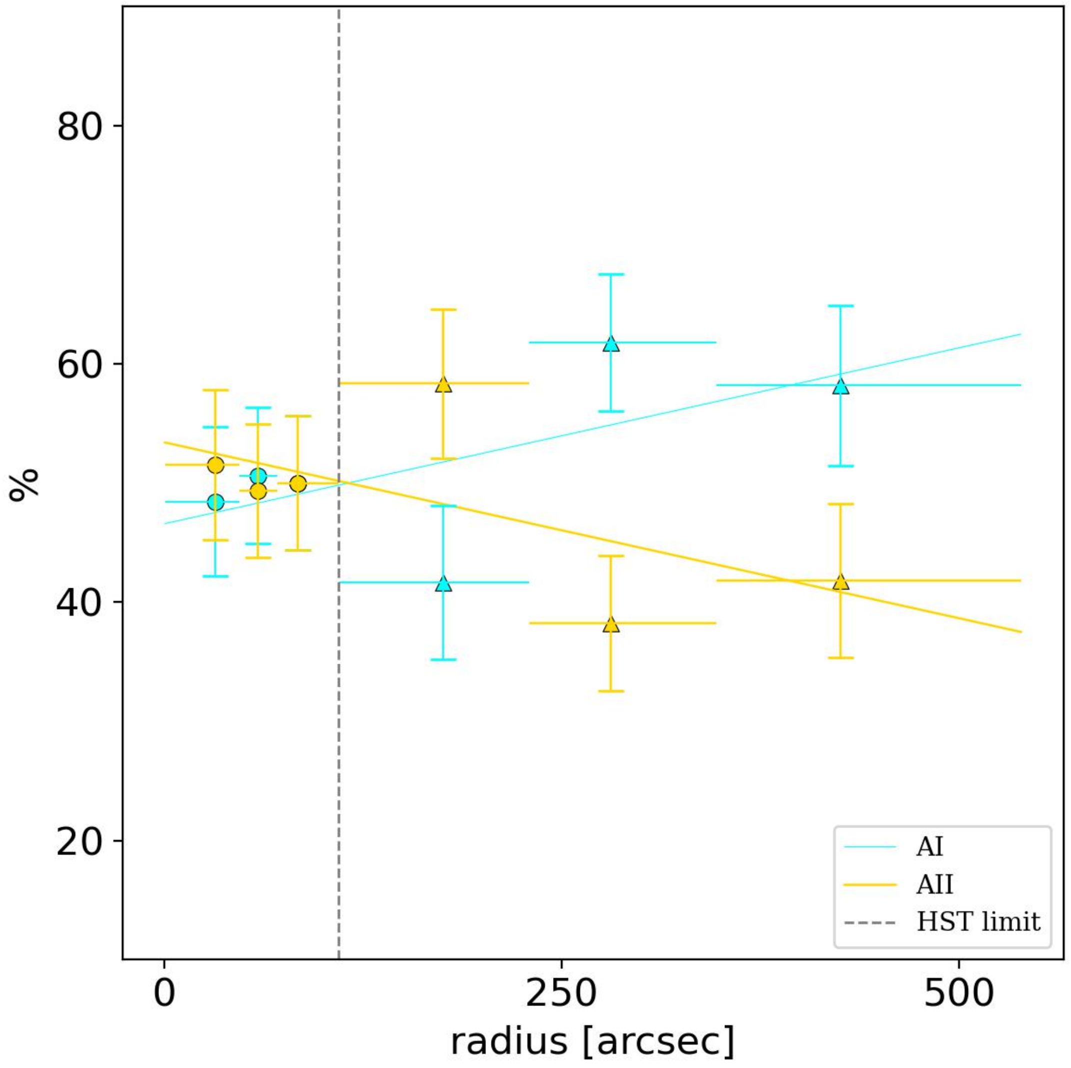

Figure 3.20: Radial distribution of metal-rich AI and AII fractions. A vertical grey dotted line is added as reference for the limit of HST FoV. Circles represent datapoints from HST observations while triangles do so for GB observations.

Notably, both metal-rich and metal-poor sub-populations behave in a similar way, with the populations distributed around larger y-axis values on the ChM, 2G and AII, are more centrally concentrated than 1G and AI, respectively.

3.2.5 Chemical composition of MSPs

To infer the average chemical composition of the different populations in M22, stars in our ChMs are cross-matched with literature spectroscopic abundances of [Na/Fe], [Al/Fe], and [Fe/H]. Sodium abundances are taken from Aguilera-Gómez et al., 2021, while aluminum and iron values were measured by the APOGEE survey (see **Section 2.2.5** for details).

Spectroscopic observations, as opposed to photometric observations, are not only time consuming but also require a very good angular resolution, both of which turn this observations highly costly, hence, spectroscopic data is available for a very small fraction of stars with a photometric identification.

In the present work, a subset of 95 stars is considered. Results are presented in **Figs. 3.21, 3.22**, and **3.23** for iron, aluminum, and sodium, respectively, where the *upper panels* present the HST (left) and GB (right) ChMs. Here, stars with available spectroscopic measurements are highlighted in green, magenta, cyan and yellow 'starred' symbols, following the color-coding introduced in this section. The central panels illustrate the median [Fe/H] values per population along with colored vertical bands that represent their interquartile range. The *bottom panels* are instead a representation of all the stars with chemical abundances used in our sample. These figures show that, as expected, anomalous stars are iron enriched with respect to the canonicals, while within their sub-populations no evident iron differences are present (it is worth noting that there is a small iron enrichment among the AII stars, though their interquartile range distributions overlap). Sodium and aluminum (two light elements that typically vary between multiple populations) are more abundant among the metal-rich population, and also present differences within the respective sub-populations: 2G are on average aluminum- and sodium-richer than 1G stars, which is a typical behavior of MSPs, but a similar trend is observed even in the anomalous stars, where AII are enriched in both elements with respect to the AI.

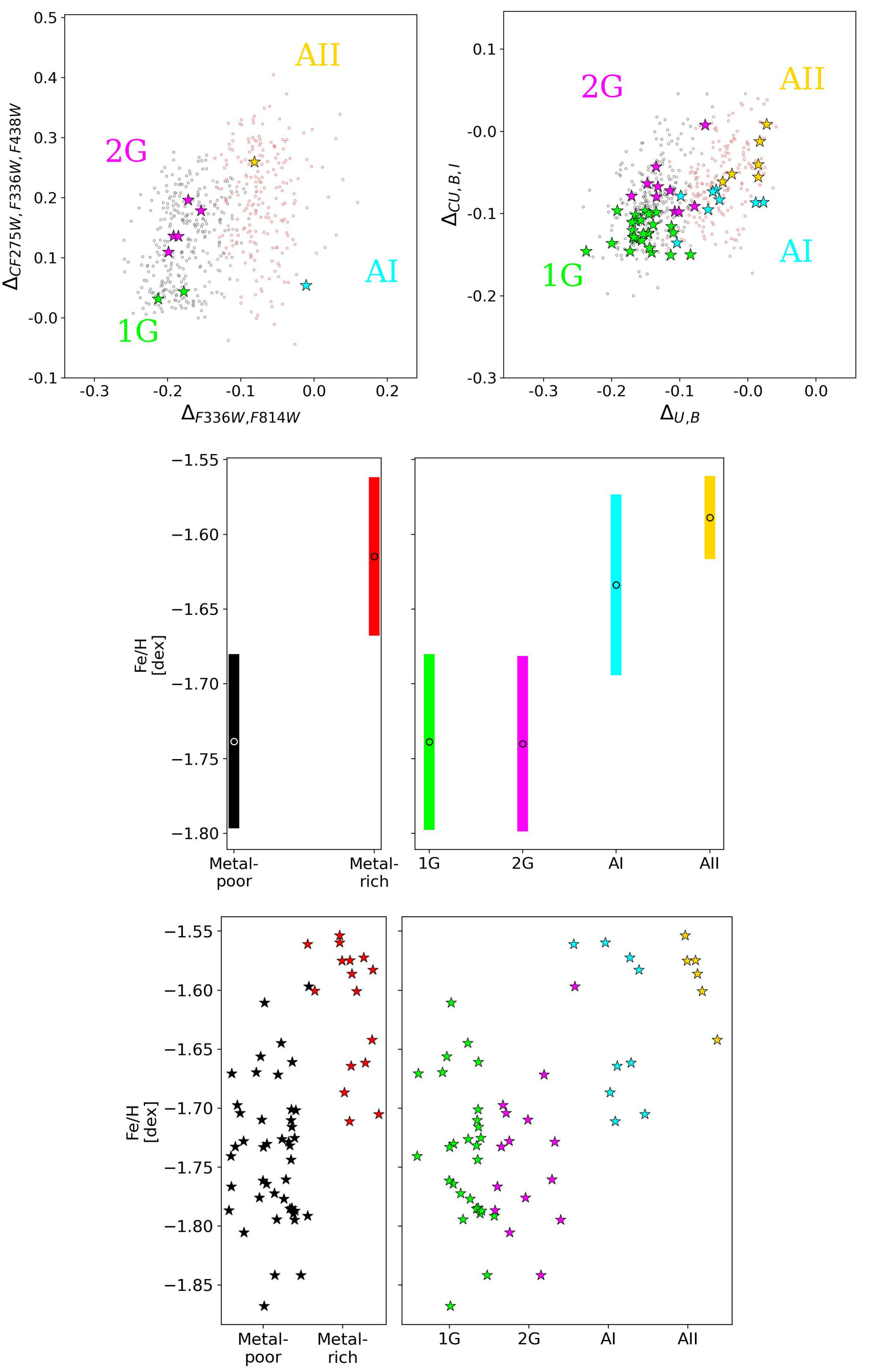

Figure 3.21: Fe/H abundance spectroscopy.

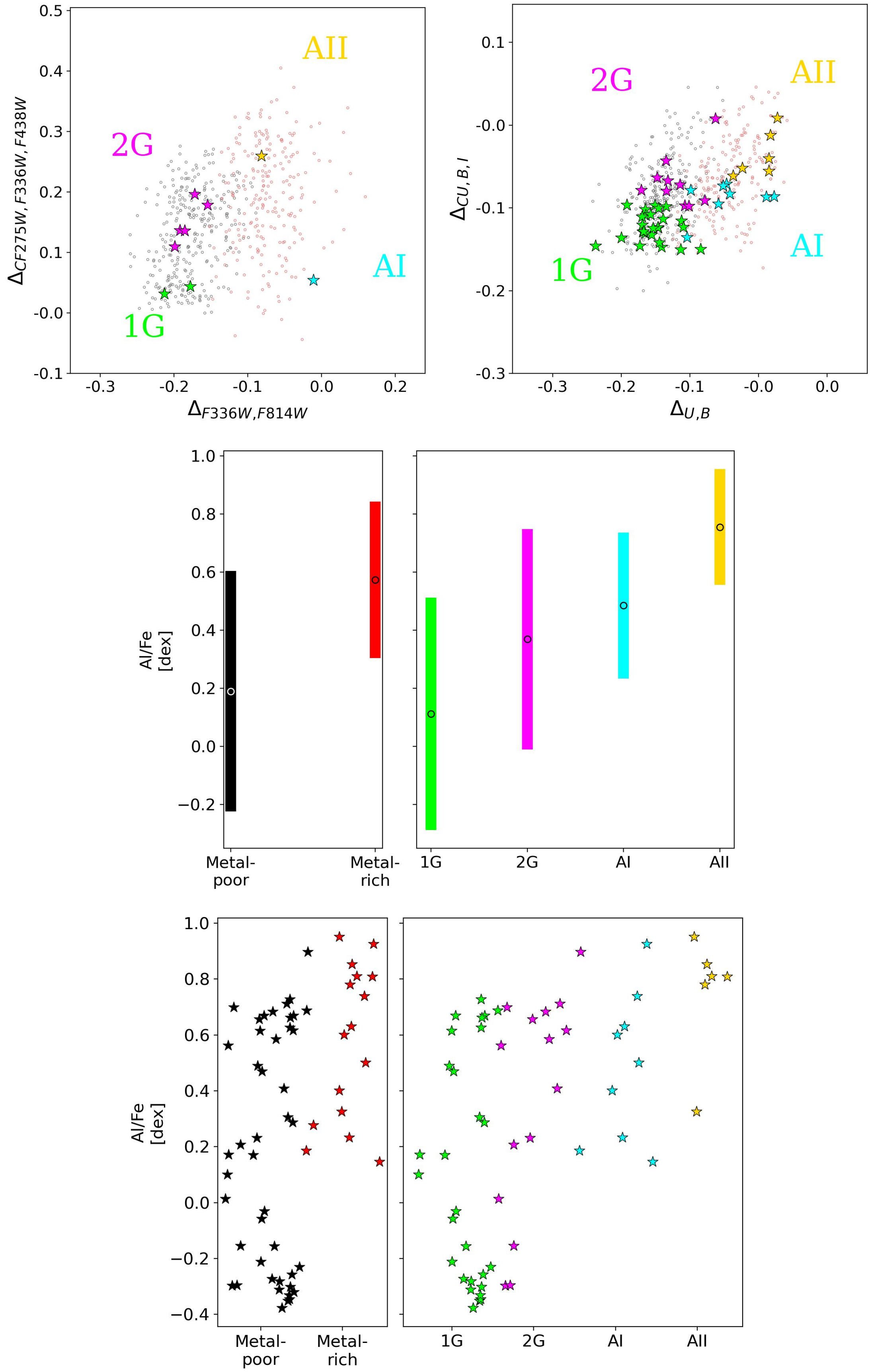

Figure 3.22: Al/Fe abundance spectroscopy.

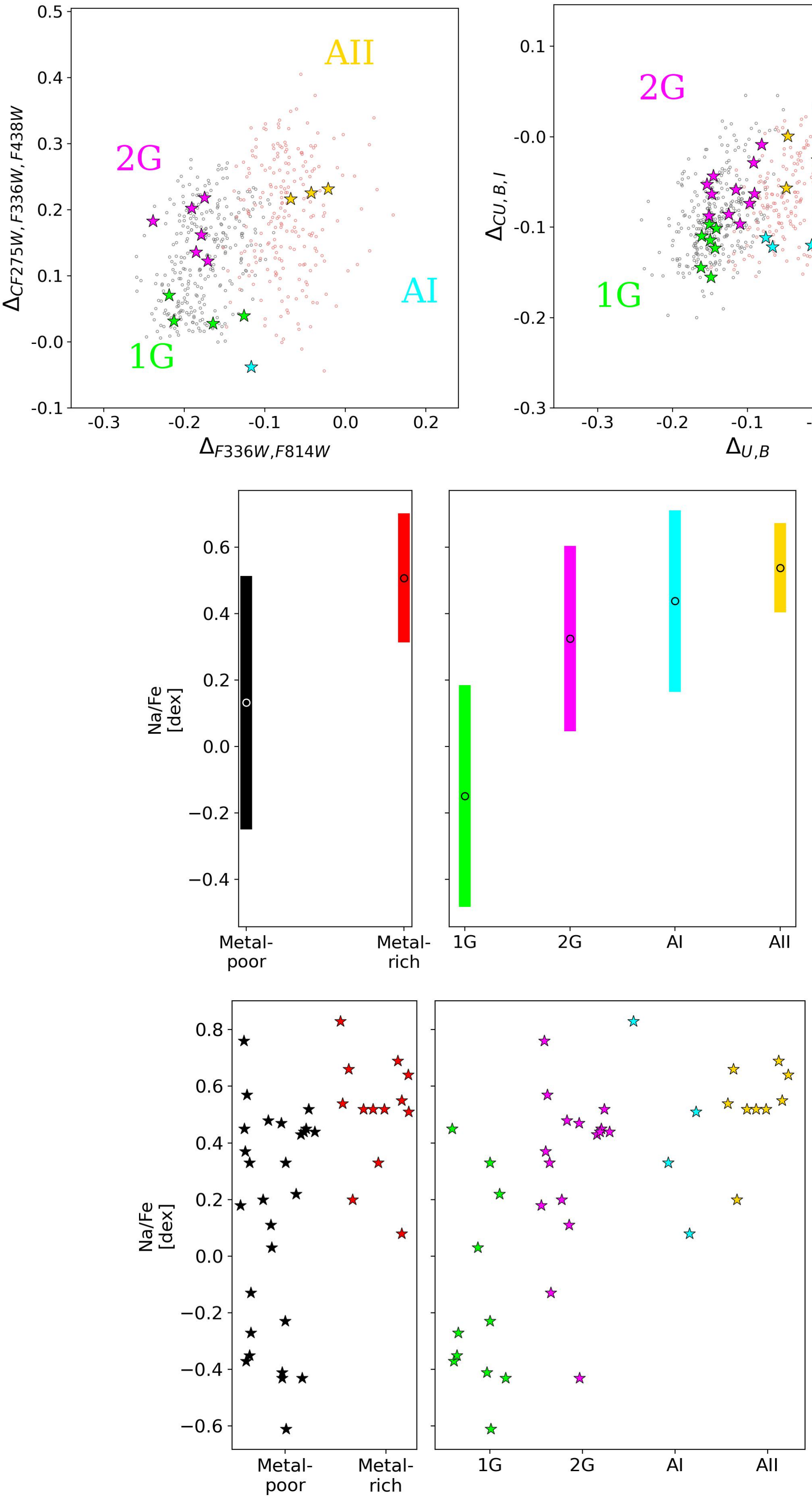

Figure 3.23: Na/Fe abundance spectroscopy.

In **Fig. 3.24**, mean abundance values for each population (and sub-population) are represented in chemical abundance coordinates on [Al/Fe] vs. [Fe/H] and [Al/Fe] vs. [Na/Fe] diagrams. Here, dots represent the metal-poor and metal-rich populations, while triangles indicate their sub-populations. This diagrams further show how these elements are correlated, with the aluminum abundance increasing with iron and sodium enrichment, thus suggesting that the phenomena that led to an increase in iron and in light elements are linked to each other. In this Figure, grey errorbars represent the average uncertainty on the abundances measured with spectroscopy, clearly proving that the observed distribution of points is much wider than predicted by errors only.

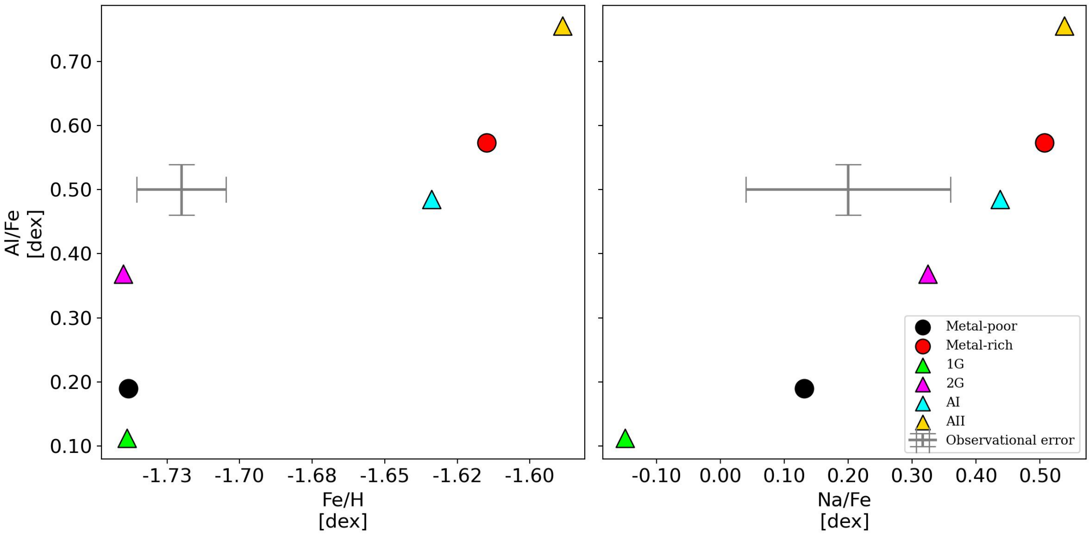

Figure 3.24: Representation of chemical distribution per population. Color coded circles in black and red are used for Metal-poor and Metal-rich populations, in the same manner, color coded triangles in green, magenta, cyan and yellow are used for 1G, 2G, AI, and AII populations respectively. Average observational errors are represented with a grey cross. This representation is not limited to same-star correlation, but relates the average abundance of the total population. *Left panel:* Al/Fe correlation. *Right panel:* Al/Na correlation.

As seen in **Table 3.3**, the cluster is confirmed to be a metal-poor one with ⟨*Fe/H*⟩ = -1.705 (σ=0.058), in agreement with Marino et al., 2011 that report ⟨*Fe/H*⟩ = -1.76 (σ=0.10). Also, as a whole, M22 is both sodium and aluminum enhanced (⟨*Na/Fe*⟩ = 0.254 (σ=0.381) and ⟨*Al/Fe*⟩ = 0.292 (σ=0.415)), though sub-population 1G is actually sodium depleted.

Abundance variation results are presented in **Tables 3.4** and **3.5**. The metal-poor population presents a spread in metallicity of 0.058 dex, with a clear separation in Al abundance of 0.415 dex at constant metallicity for sub-populations 1G and 2G. Population 2G, AI and AII are all progressively enhanced in both sodium and aluminum with respect to 1G.

The metal-rich population sodium and aluminum enhanced with respect to the metal-poor and has not only higher values for metallicity, but also a much grander variation between sub-populations of 0.045 dex for 0.001 dex for the metal-poor population. The chemical abundance distribution for the metal-rich populations AI and AII is poorly described with the present data but the very wide spread of both iron and sodium hints to be in accordance with the present hypothesis that this population is composed by at least 2 sub-populations (AI and AII in the present work), as supported by Lee, 2019, where 3 sub-populations are proposed.

	$\langle Fe/H \rangle$ [dex]	$\pm\sigma$	**$\langle Al/Fe \rangle$ [dex]**	$\pm\sigma$	**$\langle Na/Fe \rangle$ [dex]**	$\pm\sigma$
Total	-1.705	0.058	0.292	0.415	0.254	0.381
Metal-poor	-1.738	0.058	0.190	0.415	0.131	0.382
Metal-rich	-1.615	0.053	0.573	0.270	0.507	0.194
1G	-1.739	0.059	0.112	0.400	-0.149	0.334
2G	-1.740	0.059	0.369	0.380	0.324	0.279
AI	-1.634	0.060	0.485	0.251	0.438	0.273
AII	-1.589	0.028	0.755	0.200	0.538	0.135

Table 3.3: Mean chemical abundances for M22 overall and per population.

	$\delta Fe/H$ [dex]	$\pm\sigma$	**$\delta Al/Fe$ [dex]**	$\pm\sigma$	**$\delta Na/Fe$ [dex]**	$\pm\sigma$
Metal-poor	0.058	0.015	0.415	0.040	0.382	0.160
Metal-rich	0.053	0.015	0.270	0.039	0.194	0.160
1G	0.059	0.015	0.400	0.040	0.334	0.160
2G	0.059	0.016	0.380	0.040	0.279	0.160
AI	0.060	0.016	0.251	0.040	0.273	0.160
AII	0.028	0.015	0.200	0.039	0.135	0.160

Table 3.4: Intrinsic spread of chemical abundances per population.

	Δ*Fe/H* [dex]	**±σ**	**Δ*Al/Fe* [dex]**	**±σ**	**Δ*Na/Fe* [dex]**	**±σ**
Metal-poor* vs *Metal-rich	0.124	0.079	0.384	0.495	0.375	0.428
1G vs 2G	0.001	0.083	0.256	0.552	0.473	0.435
1G vs A	0.124	0.079	0.461	0.483	0.656	0.386
2G vs A	0.125	0.079	0.205	0.466	0.183	0.340
AI vs AII	0.045	0.066	0.270	0.321	0.100	0.305

Table 3.5: Variations in chemical abundances between populations.

4

Discussion & conclusions

In this chapter, a brief discussion of the data analysis is presented. The main results of the thesis are summarized and compared to literature. Finally, qualitative constraints are presented towards the identification of the origin and evolution of M22.

In this thesis, I reduced the most recent images of M22 taken with the F475W and F814W filters of the ACS/WFC camera onboard the HST by performing state-of-the-art PSF photometry, producing a high-precision catalog with astrometry and photometry of the stars in the external field of the cluster. Moreover, I combined several multiband, multi-facility catalogs (including both HST and ground-based observations) to provide the most complete photometric tagging of the different populations that inhabit M22 to date.

The main results of my thesis are summarized as follows:

- The data reduction procedure included the derivation of a reddening map accounting for differential reddening on the FoV of the most recent HST observations (Dataset 1, described in **Sec. 2.2.1**), obtaining $\Delta E(B-V)$=0.051 and $\sigma_{\Delta E(B-V)}$=0.010, in qualitative agreement with literature (Legnardi et al., 2023, Monaco et al., 2004) as presented in **Table 2.2**.
- As a result of the full data reduction procedure, the m_{F814W} vs. (m_{F475W}-m_{F814W}) CMD displayed in **Fig. 2.10** was derived. I performed isochrone fit on this diagram to estimate the age, luminosity distance and reddening of M22, finding that this cluster has an age range of 13.2-13.8 Gyr, at a distance of 3.31 kpc, and with *E(B-V)*=0.39, as presented in **Table 3.1**. These

numbers are qualitatively in agreement with previous literature results (Marino et al., 2011, Marino et al., 2012, Piotto et al., 1999, Baumgardt et al., 2018, and Legnardi et al., 2023). The range in the computed age could be explained directly as an intrinsic variation in age, however, as detailed by Marino et al., 2012, another explanation is that of a spread in metallicity of coeval stars, which is hereby confirmed by the results from spectroscopy seen in **Table 3.5**.

- I identified 1G, 2G, and anomalous sub-populations in the RGB stars along the whole cluster area, from its center to the outskirts, thanks to the derivation of different ChMs based on HST and ground-based observations. Moreover, I noticed how in all the ChMs anomalous stars exhibit a y-axis spread comparable to the bulk of 1G and 2G stars, thus suggesting the presence of light-elements differences even among this group of stars. For that, the AI and AII anomalous sub-populations are tentatively defined as the ones below and above the 50^{th} percentile of the anomalous stars y-axis distribution. The proportion of canonical and anomalous stars is 0.601:0.399 ± 0.016, in agreement with Lee, 2019 and Milone et al., 2017, with reported values of 0.63:0.37 ± 0.03 and 0.597:0.403 ± 0.021 respectively; while 1G, 2G (with relative fractions 0.46:0.54 ± 0.04), AI, and AII stars occupy a fraction of 0.283, 0.330, 0.194, and 0.194 ± 0.02 respectively (see **Table 3.2**).
- I inferred the radial behaviour of the fraction of the bulk of canonical and anomalous stars (see **Fig. 3.18**), finding that the latter decreases moving outwards and the former dominates all over the cluster at around 60%, the p-value test result is 0.22 for this trend, which hints at the possibility of the distribution being even flatter.
- I then derived, for the first time, the radial distribution of their sub-populations, as seen in **Fig. 3.19** and **3.20** discovering that in both cases, the second generation is more centrally concentrated, up to above 60% at the centermost region for the case of 2G population, result which is in agreement with Lee, 2019 where Cumulative Radial Distributions of individual sub-populations in M22 based on photometric CN and CH abundance were derived on a radius of over 800 arcsec, and resulting in the proposed CN-enriched sub-populations (related to the second generation populations 2G and AII in the present work) in both the canonical and anomalous groups being more centrally concentrated. The derived p-values for my linear fits are 0.08, and 0.18 for relative metal-poor 1G

and 2G, and relative metal-rich AI and AII populations respectively. The CDFs of these populations qualitatively agree with what is derived from the radial distribution of the fractions.

- I combined the photometric population tagging introduced in this work with spectroscopy measurements from the literature of iron, aluminum, and sodium abundances, with results presented in **Figs. 3.21, 3.22**, and **3.23**, and condensed in **Table 3.5**, from which I find M22 to be a metal-poor cluster, with $\langle Fe/H \rangle$ =-1.705 (σ=0.058), in agreement with both Marino et al., 2009b,2011 and Mészáros et al., 2019, with reported values of $\langle Fe/H \rangle$ =-1.76 ± 0.02 and $\langle Fe/H \rangle$ =-1.52 ± 0.09, respectively.
- Regarding the abundance of aluminum and sodium, I find M22 to be enhanced in both, with $\langle Al/Fe \rangle$ =0.292 (σ=0.415) and $\langle Na/Fe \rangle$ =0.254 (σ=0.381), which again are in agreement with literature as Marino et al., 2011 reports $\langle Al/Fe \rangle$ =0.34 ± 0.08 and $\langle Na/Fe \rangle$ =0.24 ± 0.08, while Mészáros et al., 2019 reports $\langle Al/Fe \rangle$ =0.46 ± 0.09. When contrasting the chemical abundances between metal-poor and metal-rich populations, the resulting $\Delta Fe/H$ =0.124 ± 0.079, $\Delta Al/Fe$ =0.384 ± 0.495, and $\Delta Na/Fe$ =0.382 ± 0.428 support the conclusion from Marino et al., 2011 which confirms two groups of stars with mean abundances of $\langle Fe/H \rangle$ =1.63 and $\langle Fe/H \rangle$ = 1.89.
- Aditionally, I find small intrinsic metallicity spreads in every population, being the metal-rich AI population the one with the largest variation with $\delta Fe/H$=0.060 ±0.016, well within the behaviour of populations 1G and 2G. The sub-populations AI and AII differ chemically in both sodium and aluminum abundances by 0.270 dex for Al and 0.100 dex for Na, albeit with large intrinsic spread in both (above 0.200 dex ± 0.039 for Al and above 0.135 dex ± 0.160 for Na) which supports the hypothesis of the anomalous population being composed by two or more sub-populations, as proposed by Lee, 2019.

  In general, my results further confirm M22 as a metal poor Type II GC as reported by Marino et al., 2009b, Marino et al., 2011, Marino et al., 2012, Milone et al., 2017, Lee, 2019 and McKenzie et al., 2022; Na and Al abundances are also in agreement with the cited works, further characterizing the chemical composition of M22 both in the inner and outer FoV.

The results of this thesis provide a new set of observational constraints that a model aimed at explaining the formation and evolution of M22 (and possibly other Type II GCs) should take into account. In particular, the fact that the AI and AII sub-populations of metal-rich anomalous stars qualitatively behave in a similar way as the 1G and 2G stars in terms of radial distribution and intrinsic light-element spread, which may be a sign that canonical and anomalous stars were born within two initially-separated GCs that merged into one. Bekki et al., 2016 developed a model, based on the observational constraints of M22 known at that time, in which each GC formed within a dwarf galaxy, thus accounting the chemical differences between the two groups of stars to the chemical evolution of the host galaxy. However, not all the observational constraints are naturally fulfilled by this model (see their Section 4.2), and the possibility that Type II GCs were not the product of a merging but rather that they experienced a prolonged star formation history compared to Type I GCs should not be excluded (D'Antona et al., 2016).

References

[1] C. Aguilera-Gómez et al. "Lithium on the lower red giant branch of five Galactic globular clusters". In: *Astronomy & Astrophysics* 657 (Dec. 2021), A33. ISSN: 1432-0746. DOI: `10.1051/0004-6361/202141750`. URL: `http://dx.doi.org/10.1051/0004-6361/202141750`.

[2] J Anderson et al. "Toward HighPrecision Astrometry with WFPC2. I. Deriving an Accurate PointSpread Function". In: *Publications of the Astronomical Society of the Pacific* 112.776 (Oct. 2000), pp. 1360–1382. ISSN: 1538-3873. DOI: `10.1086/316632`. URL: `http://dx.doi.org/10.1086/316632`.

[3] J. Anderson et al. *PSFs, Photometry, and Astronomy for the ACS/WFC*. Instrument Science Report ACS 2006-01, 34 pages. Feb. 2006.

[4] Barbara J. Anthony-Twarog et al. "CN and CA abundance variations among the giants in M22". In: *Publications of the Astronomical Society of the Pacific* 107 (Jan. 1995), p. 32. ISSN: 1538-3873. DOI: `10.1086/133513`. URL: `http://dx.doi.org/10.1086/133513`.

[5] N. Bastian et al. "Early disc accretion as the origin of abundance anomalies in globular clusters". In: *Monthly Notices of the Royal Astronomical Society* 436.3 (Oct. 2013), pp. 2398–2411. ISSN: 0035-8711. DOI: `10.1093/mnras/stt1745`. URL: `http://dx.doi.org/10.1093/mnras/stt1745`.

[6] H Baumgardt et al. "A catalogue of masses, structural parameters, and velocity dispersion profiles of 112 Milky Way globular clusters". In: *Monthly Notices of the Royal Astronomical Society* 478.2 (May 2018), pp. 1520–1557. ISSN: 1365-2966. DOI: `10.1093/mnras/sty1057`. URL: `http://dx.doi.org/10.1093/mnras/sty1057`.

[7] Kenji Bekki et al. "FORMATION OF ANOMALOUS GLOBULAR CLUSTERS WITH METALLICITY SPREADS: A UNIFIED PICTURE". In: *The Astrophysical Journal* 831.1 (Oct. 2016), p. 70. ISSN: 1538-4357. DOI: `10.3847/`

0004-637x/831/1/70. URL: http://dx.doi.org/10.3847/0004-637X/831/1/70.

[8] M. Bellazzini et al. "THE NUCLEUS OF THE SAGITTARIUS DSPH GALAXY AND M54: A WINDOW ON THE PROCESS OF GALAXY NUCLEATION". In: *The Astronomical Journal* 136.3 (Aug. 2008), pp. 1147–1170. ISSN: 1538-3881. DOI: 10.1088/0004-6256/136/3/1147. URL: http://dx.doi.org/10.1088/0004-6256/136/3/1147.

[9] A. Bellini et al. "Radial distribution of the multiple stellar populations in ω Centauri". In: *Astronomy & Astrophysics* 507.3 (Oct. 2009), pp. 1393–1408. ISSN: 1432-0746. DOI: 10.1051/0004-6361/200912757. URL: http://dx.doi.org/10.1051/0004-6361/200912757.

[10] A. Bellini et al. "The State-of-the-art HST Astro-photometric Analysis of the Core of Centauri. I. The Catalog". In: *The Astrophysical Journal* 842.1 (June 2017), p. 6. ISSN: 1538-4357. DOI: 10.3847/1538-4357/aa7059. URL: http://dx.doi.org/10.3847/1538-4357/aa7059.

[11] Andrea Bellini et al. "The HST large programme on ω Centauri. II. Internal kinematics". In: *The Astrophysical Journal* 853.1 (2018), p. 86.

[12] Ralph C. Bohlin. "PERFECTING THE PHOTOMETRIC CALIBRATION OF THE ACS CCD CAMERAS". In: *The Astronomical Journal* 152.3 (Aug. 2016), p. 60. DOI: 10.3847/0004-6256/152/3/60. URL: https://dx.doi.org/10.3847/0004-6256/152/3/60.

[13] Emanuele Bortolan. *Multiple populations among very low-mass stars in NGC 288*. 2022.

[14] E Margaret Burbidge et al. "Synthesis of the elements in stars". In: *Rev. Mod. Phys.* 29.4 (Oct. 1957), pp. 547–650.

[15] E. Carretta et al. "Na-O anticorrelation and HB: VII. The chemical composition of first and second-generation stars in 15 globular clusters from GIRAFFE spectra". In: *Astronomy & Astrophysics* 505.1 (July 2009), pp. 117–138. ISSN: 1432-0746. DOI: 10.1051/0004-6361/200912096. URL: http://dx.doi.org/10.1051/0004-6361/200912096.

[16] E. Carretta et al. "ABUNDANCES FOR A LARGE SAMPLE OF RED GIANTS IN NGC 1851: HINTS FOR A MERGER OF TWO CLUSTERS?" In: *The Astrophysical Journal* 722.1 (Sept. 2010), pp. L1–L6. ISSN: 2041-8213. DOI: 10.1088/2041-8205/722/1/l1. URL: http://dx.doi.org/10.1088/2041-8205/722/1/L1.

[17] M J Cordero et al. "Detailed abundances for a large sample of giant stars in the globular cluster 47 tucanae (ngc 104)". In: *Astrophys. J.* 780.1 (Dec. 2013), p. 94.

[18] Giacomo Cordoni et al. "Multiple stellar populations found outside the tidal radius of NGC 1851 via Gaia DR3 XP spectra". In: *Astronomy & Astrophysics* 678 (Oct. 2023), A155. ISSN: 1432-0746. DOI: `10.1051/0004-6361/202347189`. URL: `http://dx.doi.org/10.1051/0004-6361/202347189`.

[19] F. D'Antona et al. "A single model for the variety of multiple-population formation(s) in globular clusters: a temporal sequence". In: *Monthly Notices of the Royal Astronomical Society* 458.2 (Feb. 2016), pp. 2122–2139. ISSN: 0035-8711. DOI: `10.1093/mnras/stw387`. eprint: `https://academic.oup.com/mnras/article-pdf/458/2/2122/18240620/stw387.pdf`. URL: `https://doi.org/10.1093/mnras/stw387`.

[20] Annibale D'Ercole et al. "Abundance patterns of multiple populations in globular clusters: a chemical evolution model based on yields from AGB ejecta". en. In: *Mon. Not. R. Astron. Soc.* 407.2 (Sept. 2010), pp. 854–869.

[21] E Dalessandro et al. "The unexpected kinematics of multiple populations in NGC 6362: Do binaries play a role?" In: *Astrophys. J.* 864.1 (Aug. 2018), p. 33.

[22] J. F. Dean et al. "Reddenings of Cepheids using BVI photometry". In: *Monthly Notices of the Royal Astronomical Society* 183.4 (Aug. 1978), pp. 569–583. ISSN: 0035-8711. DOI: `10.1093/mnras/183.4.569`. eprint: `https://academic.oup.com/mnras/article-pdf/183/4/569/2796047/mnras183-0569.pdf`. URL: `https://doi.org/10.1093/mnras/183.4.569`.

[23] Hans Dekker et al. "Design, construction, and performance of UVES, the echelle spectrograph for the UT2 Kueyen Telescope at the ESO Paranal Observatory". In: *Optical and IR Telescope Instrumentation and Detectors*. Ed. by Masanori Iye et al. Vol. 4008. Society of Photo-Optical Instrumentation Engineers (SPIE) Conference Series. Aug. 2000, pp. 534–545. DOI: `10.1117/12.395512`.

[24] P. A. Denissenkov et al. "Supermassive stars as a source of abundance anomalies of proton-capture elements in globular clusters". In: *Monthly Notices of the Royal Astronomical Society: Letters* 437.1 (Oct. 2013), pp. L21–L25. ISSN: 1745-3933. DOI: `10.1093/mnrasl/slt133`. URL: `http://dx.doi.org/10.1093/mnrasl/slt133`.

[25] M Di Criscienzo et al. “NGC 2419: a large and extreme second generation in a currently undisturbed cluster”. en. In: *Mon. Not. R. Astron. Soc.* 414.4 (July 2011), pp. 3381–3393.

[26] E. Dondoglio et al. *A deep dive into the Type II Globular Cluster NGC 1851*. 2023. arXiv: `2309.16423 [astro-ph.GA]`.

[27] Emanuele Dondoglio. *Investigating the effect of redshift and host galaxy on the multiple-population phenomenon*. 2020.

[28] Aaron Dotter et al. “The ACS survey of galactic globular clusters. II. Stellar evolution tracks, isochrones, luminosity functions, and synthetic horizontal-branch models”. en. In: *Astron. J.* 134.1 (July 2007), pp. 376–390.

[29] Richard Edgar. “A review of BondiHoyleLyttleton accretion”. In: *New Astronomy Reviews* 48.10 (Sept. 2004), pp. 843–859. ISSN: 1387-6473. DOI: `10.1016/j.newar.2004.06.001`. URL: `http://dx.doi.org/10.1016/j.newar.2004.06.001`.

[30] ESA. *GAIA overview*. 2013. URL: `https://www.esa.int/Science_Exploration/Space_Science/Gaia/Gaia_overview` (visited on 06/25/2024).

[31] Raffaele Gratton et al. “Abundance Variations within Globular Clusters”. In: *Annual Review of Astronomy and Astrophysics* 42.1 (Sept. 2004), pp. 385–440. ISSN: 1545-4282. DOI: `10.1146/annurev.astro.42.053102.133945`. URL: `http://dx.doi.org/10.1146/annurev.astro.42.053102.133945`.

[32] J. N. Heasley. “Point-Spread Function Fitting Photometry”. In: *Precision CCD Photometry*. Ed. by Eric R. Craine et al. Vol. 189. Astronomical Society of the Pacific Conference Series. Jan. 1999, p. 56.

[33] Robert P Kraft. “Abundance differences among globular-cluster giants: Primordial versus evolutionary scenarios”. In: *Publ. Astron. Soc. Pac.* 106 (June 1994), p. 553.

[34] M. Krause et al. “Superbubble dynamics in globular cluster infancy: II. Consequences for secondary star formation in the context of self-enrichment via fast-rotating massive stars”. In: *Astronomy & Astrophysics* 552 (Apr. 2013), A121. ISSN: 1432-0746. DOI: `10.1051/0004-6361/201220694`. URL: `http://dx.doi.org/10.1051/0004-6361/201220694`.

[35] Jae-Woo Lee. “Five Stellar Populations in M22 (NGC 6656)”. In: *The Astrophysical Journal Letters* 888.1 (Dec. 2019), p. L6. ISSN: 2041-8213. DOI: `10.3847/2041-8213/ab60b2`. URL: `http://dx.doi.org/10.3847/2041-8213/ab60b2`.

[36] M V Legnardi et al. "Differential reddening in the direction of 56 Galactic globular clusters". In: *Monthly Notices of the Royal Astronomical Society* 522.1 (Apr. 2023), pp. 367–380. ISSN: 1365-2966. DOI: 10.1093/mnras/stad1056. URL: http://dx.doi.org/10.1093/mnras/stad1056.

[37] Maria Vittoria Legnardi. *Constraining the composition of pristine material through first-generation stars in globular clusters*. 2021.

[38] R. Lupton et al. *SM 2.4.0 user manual*. 1996.

[39] A F Marino et al. "The double sub-giant branch of NGC 6656 (M 22): a chemical characterization". In: *Astron. Astrophys.* 541 (May 2012), A15.

[40] A. F. Marino et al. "Spectroscopic and photometric evidence of two stellar populations in the Galactic globular cluster NGC 6121 (M4)". In: *Astronomy & Astrophysics* 490.2 (Aug. 2008), pp. 625–640. ISSN: 1432-0746. DOI: 10.1051/0004-6361:200810389. URL: http://dx.doi.org/10.1051/0004-6361:200810389.

[41] A. F. Marino et al. "Chemical composition of stellar populations in Centauri". In: *Proceedings of the International Astronomical Union* 5.S268 (Nov. 2009), pp. 183–184. ISSN: 1743-9221. DOI: 10.1017/s1743921310004096. URL: http://dx.doi.org/10.1017/S1743921310004096.

[42] A. F. Marino et al. "The two metallicity groups of the globular cluster M 22: a chemical perspective". In: *Astron. Astrophys.* 532 (Aug. 2011), A8.

[43] A. F. Marino et al. "The halo+cluster system of the Galactic globular cluster NGC 1851". In: *Monthly Notices of the Royal Astronomical Society* 442.4 (June 2014), pp. 3044–3064. ISSN: 0035-8711. DOI: 10.1093/mnras/stu1099. eprint: https://academic.oup.com/mnras/article-pdf/442/4/3044/13765505/stu1099.pdf. URL: https://doi.org/10.1093/mnras/stu1099.

[44] A. F. Marino et al. "Iron and s-elements abundance variations in NGCă5286: comparison with anomalous' globular clusters and Milky Way satellites". In: *Monthly Notices of the Royal Astronomical Society* 450.1 (Apr. 2015), pp. 815–845. ISSN: 0035-8711. DOI: 10.1093/mnras/stv420. eprint: https://academic.oup.com/mnras/article-pdf/450/1/815/18754351/stv420.pdf. URL: https://doi.org/10.1093/mnras/stv420.

[45] F. Marino et al. "A double stellar generation in the globular cluster NGC 6656 (M 22)". In: *Astron. Astrophys.* 505.3 (Oct. 2009), pp. 1099–1113.

[46] A. J. van Marle et al. "ContinuumDriven Winds from SuperEddington Stars: A Tale of Two Limits". In: (2008). ISSN: 0094-243X. DOI: `10.1063/1.2905555`. URL: `http://dx.doi.org/10.1063/1.2905555`.

[47] M McKenzie et al. "The complex stellar system M 22: confirming abundance variations with high precision differential measurements". In: *Monthly Notices of the Royal Astronomical Society* 516.3 (Aug. 2022), pp. 3515–3531. ISSN: 0035-8711. DOI: `10.1093/mnras/stac2254`. eprint: `https://academic.oup.com/mnras/article-pdf/516/3/3515/45932096/stac2254.pdf`. URL: `https://doi.org/10.1093/mnras/stac2254`.

[48] *Messier 22 - NASA Science — science.nasa.gov*. `https://science.nasa.gov/mission/hubble/science/explore-the-night-sky/hubble-messier-catalog/messier-22/`. [Accessed 12-06-2024].

[49] Szabolcs Mészáros et al. "Homogeneous analysis of globular clusters from the APOGEE survey with the BACCHUS code II. The Southern clusters and overview". In: *Monthly Notices of the Royal Astronomical Society* 492.2 (Dec. 2019), pp. 1641–1670. ISSN: 0035-8711. DOI: `10.1093/mnras/stz3496`. eprint: `https://academic.oup.com/mnras/article-pdf/492/2/1641/33127961/stz3496.pdf`. URL: `https://doi.org/10.1093/mnras/stz3496`.

[50] A P Milone et al. "The infrared eye of the wide-field camera 3 on the Hubble space telescope reveals multiple main sequences of very low mass stars in ngc 2808". In: *Astrophys. J. Lett.* 754.2 (Aug. 2012), p. L34.

[51] A P Milone et al. "A wfc3/hstview of the three stellar populations in the globular cluster ngc 6752". In: *Astrophys. J.* 767.2 (Apr. 2013), p. 120.

[52] A P Milone et al. "The*Hubble* Space TelescopeUV Legacy Survey of Galactic globular clusters – IX. The Atlas of multiple stellar populations". en. In: *Mon. Not. R. Astron. Soc.* 464.3 (Jan. 2017), pp. 3636–3656.

[53] A P Milone et al. "The Hubble Space Telescope UV legacy survey of galactic globular clusters – XVI. The helium abundance of multiple populations". en. In: *Mon. Not. R. Astron. Soc.* 481.4 (Dec. 2018), pp. 5098–5122.

[54] A P Milone et al. "Multiple populations in globular clusters and their parent galaxies". In: *Monthly Notices of the Royal Astronomical Society* 491.1 (Oct. 2019), pp. 515–531. ISSN: 0035-8711. DOI: `10.1093/mnras/stz2999`. eprint: `https://academic.oup.com/mnras/article-pdf/491/1/515/31076050/stz2999.pdf`. URL: `https://doi.org/10.1093/mnras/stz2999`.

[55] A P Milone et al. "The HST Large Programme on NGC 6752 – II. Multiple populations at the bottom of the main sequence probed in NIR". en. In: *Mon. Not. R. Astron. Soc.* 484.3 (Apr. 2019), pp. 4046–4053.

[56] A. P. Milone et al. "Multiple stellar populations in Magellanic Cloud clusters: I. An ordinary feature for intermediate age globulars in the LMC?" In: *Astronomy & Astrophysics* 497.3 (Feb. 2009), pp. 755–771. ISSN: 1432-0746. DOI: `10.1051/0004-6361/200810870`. URL: `http://dx.doi.org/10.1051/0004-6361/200810870`.

[57] A. P. Milone et al. "The ACS survey of Galactic globular clusters: XII. Photometric binaries along the main sequence". In: *Astronomy & Astrophysics* 540 (Mar. 2012), A16. ISSN: 1432-0746. DOI: `10.1051/0004-6361/201016384`. URL: `http://dx.doi.org/10.1051/0004-6361/201016384`.

[58] A. P. Milone et al. "The Hubble Space Telescope UV Legacy Survey of galactic globular clusters II. The seven stellar populations of NGC 7089 (M2)". In: *Monthly Notices of the Royal Astronomical Society* 447.1 (Dec. 2014), pp. 927–938. ISSN: 0035-8711. DOI: `10.1093/mnras/stu2446`. URL: `http://dx.doi.org/10.1093/mnras/stu2446`.

[59] A. P. Milone et al. "Multiple stellar populations in Magellanic Cloud clusters III. The first evidence of an extended main sequence turn-off in a young cluster: NGC 1856". In: *Monthly Notices of the Royal Astronomical Society* 450.4 (May 2015), pp. 3750–3764. ISSN: 0035-8711. DOI: `10.1093/mnras/stv829`. URL: `http://dx.doi.org/10.1093/mnras/stv829`.

[60] A. P. Milone et al. "The binary populations of eight globular clusters in the outer halo of the Milky Way". In: *Monthly Notices of the Royal Astronomical Society* 455.3 (Nov. 2015), pp. 3009–3019. ISSN: 1365-2966. DOI: `10.1093/mnras/stv2415`. URL: `http://dx.doi.org/10.1093/mnras/stv2415`.

[61] Antonino P. Milone et al. *Multiple Populations in Star Clusters*. 2022. arXiv: `2206.10564 [astro-ph.GA]`.

[62] S E de Mink et al. "Massive binaries as the source of abundance anomalies in globular clusters". In: *Astron. Astrophys.* 507.1 (Nov. 2009), pp. L1–L4.

[63] L. Monaco et al. "Wide-field photometry of the Galactic globular cluster M22". In: *Monthly Notices of the Royal Astronomical Society* 349.4 (Apr. 2004), pp. 1278–1290. ISSN: 0035-8711. DOI: `10.1111/j.1365-2966.2004.07599.x`. eprint: `https://academic.oup.com/mnras/article-pdf/349/4/1278/3041630/349-4-1278.pdf`. URL: `https://doi.org/10.1111/j.1365-2966.2004.07599.x`.

[64] M Monelli et al. "The SUMO project I. A survey of multiple populations in globular clusters". In: *Mon. Not. R. Astron. Soc.* 431.3 (May 2013), pp. 2126–2149.

[65] A. Mucciarelli et al. "Lithium abundance in lower red giant branch stars of Omega Centauri". In: *Astronomy & Astrophysics* 618 (Oct. 2018), A134. ISSN: 1432-0746. DOI: `10.1051/0004-6361/201833457`. URL: `http://dx.doi.org/10.1051/0004-6361/201833457`.

[66] D. Nardiello et al. "Observing multiple stellar populations with VLT/FORS2: Main sequence photometry in outer regions of NGC 6752, NGC 6397, and NGC 6121 (M 4)". In: *Astronomy & Astrophysics* 573 (Dec. 2014), A70. ISSN: 1432-0746. DOI: `10.1051/0004-6361/201424117`. URL: `http://dx.doi.org/10.1051/0004-6361/201424117`.

[67] Edward W. Olszewski et al. "A 500 PARSEC HALO SURROUNDING THE GALACTIC GLOBULAR NGC 1851". In: *The Astronomical Journal* 138.6 (Oct. 2009), pp. 1570–1576. ISSN: 1538-3881. DOI: `10.1088/0004-6256/138/6/1570`. URL: `http://dx.doi.org/10.1088/0004-6256/138/6/1570`.

[68] L. Pasquini et al. "Installation and commissioning of FLAMES, the VLT Multifibre Facility". In: *The Messenger* 110 (Dec. 2002), pp. 1–9.

[69] G. Piotto et al. "HST Luminosity Functions of the Globular Clusters M10, M22, and M55. A comparison with other clusters". In: (1999). arXiv: `astro-ph/9902176 [astro-ph]`.

[70] G. Piotto et al. "HUBBLE SPACE TELESCOPEREVEALS MULTIPLE SUBGIANT BRANCH IN EIGHT GLOBULAR CLUSTERS". In: *The Astrophysical Journal* 760.1 (Nov. 2012), p. 39. ISSN: 1538-4357. DOI: `10.1088/0004-637x/760/1/39`. URL: `http://dx.doi.org/10.1088/0004-637X/760/1/39`.

[71] C. Allende Prieto et al. "APOGEE: The Apache Point Observatory Galactic Evolution Experiment". In: *Astronomische Nachrichten* 329.9-10 (2008), pp. 1018–1021. DOI: `https://doi.org/10.1002/asna.200811080`. eprint: `https://onlinelibrary.wiley.com/doi/pdf/10.1002/asna.200811080`. URL: `https://onlinelibrary.wiley.com/doi/abs/10.1002/asna.200811080`.

[72] Harvey B Richer et al. "A dynamical signature of multiple stellar populations in 47 Tucanae". In: *The Astrophysical Journal Letters* 771.1 (2013), p. L15.

[73] P. Richter et al. *Stroemgren photometry of globular clusters: M55 & M22*. 1999. DOI: `10.48550/ARXIV.ASTRO-PH/9907200`. URL: `https://arxiv.org/abs/astro-ph/9907200`.

[74] I. U. Roederer et al. "CHARACTERIZING THE HEAVY ELEMENTS IN GLOBULAR CLUSTER M22 AND AN EMPIRICALs-PROCESS ABUNDANCE DISTRIBUTION DERIVED FROM THE TWO STELLAR GROUPS". In: *The Astrophysical Journal* 742.1 (Nov. 2011), p. 37. ISSN: 1538-4357. DOI: `10.1088/0004-637x/742/1/37`. URL: `http://dx.doi.org/10.1088/0004-637X/742/1/37`.

[75] Verne V. Smith. *Chemical Evolution in Omega Centauri*. 2003. arXiv: `astro-ph/0310654 [astro-ph]`. URL: `https://arxiv.org/abs/astro-ph/0310654`.

[76] A Sollima et al. "Deep FORS1 observations of the double main sequence of ω centauri". en. In: *Astrophys. J.* 654.2 (Jan. 2007), pp. 915–922.

[77] A. Sollima et al. "Spectroscopic hint of a cold stream in the direction of the globular cluster NGC 1851". In: *Monthly Notices of the Royal Astronomical Society* 426.2 (Oct. 2012), pp. 1137–1143. ISSN: 0035-8711. DOI: `10.1111/j.1365-2966.2012.21803.x`. eprint: `https://academic.oup.com/mnras/article-pdf/426/2/1137/2962588/426-2-1137.pdf`. URL: `https://doi.org/10.1111/j.1365-2966.2012.21803.x`.

[78] Space Telescope Science Institute. *HST Instrumentation*. Feb. 2024.

[79] Peter B Stetson. "Homogeneous photometry for star clusters and resolved galaxies. II. Photometric standard stars". en. In: *Publ. Astron. Soc. Pac.* 112.773 (July 2000), pp. 925–931.

[80] Mark Stevens. "Photometric Zero Point". In: *HST Data Handbook*. 1997. URL: `https://www.stsci.edu/documents/dhb/web/0_cover.fm.html`.

[81] G. Tautvaiien et al. "Gaia-ESO Survey: Detailed elemental abundances in red giants of the peculiar globular cluster NGC 1851". In: *Astronomy & Astrophysics* 658 (Feb. 2022), A80. ISSN: 1432-0746. DOI: `10.1051/0004-6361/202142234`. URL: `http://dx.doi.org/10.1051/0004-6361/202142234`.

[82] Takuji Tsujimoto et al. "Star Formation History of ω Centauri Imprinted in Elemental Abundance Patterns". In: *The Astrophysical Journal* 590 (2003), pp. 803–808. URL: `https://api.semanticscholar.org/CorpusID:15458491`.

[83] P Ventura et al. “Yields of AGB and SAGB models with chemistry of low- and high-metallicity globular clusters”. In: *Mon. Not. R. Astron. Soc.* 431.4 (June 2013), pp. 3642–3653.

[84] Enrico Vesperini et al. “The fraction of globular cluster second-generation stars in the galactic halo”. In: *Astrophys. J. Lett.* 718.2 (Aug. 2010), pp. L112–L116.

[85] Shu-i Wang et al. “ARCES: an echelle spectrograph for the Astrophysical Research Consortium (ARC) 3.5-m telescope”. In: *Instrument Design and Performance for Optical/Infrared Ground-based Telescopes*. Vol. 4841. SPIE. 2003, pp. 1145–1156.

[86] David Yong et al. “Heavy Element Abundances in Giant Stars of the Globular Clusters M4 and M5”. In: *The Astrophysical Journal* 689.2 (Dec. 2008), pp. 1031–1043. ISSN: 1538-4357. DOI: `10.1086/592600`. URL: `http://dx.doi.org/10.1086/592600`.

[87] David Yong et al. “CNO abundances in the globular clusters NGC 1851 and NGC 6752”. In: *Monthly Notices of the Royal Astronomical Society* 446.4 (Dec. 2014), pp. 3319–3329. ISSN: 0035-8711. DOI: `10.1093/mnras/stu2334`. URL: `http://dx.doi.org/10.1093/mnras/stu2334`.

[88] M Zennaro et al. “Four stellar populations and extreme helium variation in the massive outer-halo globular cluster NGC 2419”. en. In: *Mon. Not. R. Astron. Soc.* 487.3 (Aug. 2019), pp. 3239–3251.

Acknowledgments

The present thesis could not have been accomplished without the incredible guidance of Prof. A. Milone, the dedication and great insights from Dr. E. Dondoglio, the most relevant recommendations from Dr. S. Zaggia, and in general the support from the GALFOR group at the Department of Physics and Astronomy "Galileo Galilei" at the University of Padova (check out https://progetti.dfa.unipd.it/GALFOR/).